Spring 2023

Prediction & Active Control of Multi-Rotor Noise

Samuel O. Afari
Embry-Riddle Aeronautical University, afaris@my.erau.edu

Dedicated to my family, friends, and colleagues who helped throughout this journey.

ACKNOWLEDGEMENTS

I would like to express my deepest gratitude to my advisor Dr. Reda Mankbadi for his unrelenting support, patience and guidance throughout my study and research. I would also like to thank my committee members Dr. Tasos Lyrintzis for his deep insights in computational aeroacoustics, and his suggestions, Dr. Vladimir Golubev for his support and ideas for my research, and Dr. William MacKunis for his support. I would like to extend my gratitude for the support of the Florida Center for Advanced Aero-propulsion (FCAAP), as well as Embry-Riddle Aeronautical University for granting me access to the high-performance super cluster, VEGA without which this research would not have been possible.

Lastly, I would like to express my gratitude to my family and friends for enduring my arduous talks, scarce communication and long study nights, and especially Beathia, for the unending support through it all.

ABSTRACT

Significant developments have been made in designing and implementation of Advanced Air Mobility Vehicles (AAMV). However, wider applications in urban areas require addressing several challenges, such as safety and quietness. These vehicles differ from conventional helicopter in that they operate at a relatively lower Reynolds number. More chiefly, they operate with multiples of rotors, which may pose some issues aerodynamically, as well as acoustically.

The aim of this research is to first investigate the various noise sources in multi-rotor systems. High-fidelity simulations of two in-line counter-rotating propellers in hover, and in forward flight conditions are performed. Near field flow and acoustic properties were resolved using Hybrid LES-Unsteady RANS approach. Far-field sound predictions were performed using Ffowcs-Williams-Hawkings formulation. The two-propeller results in hovering are compared with that of the single propeller. This enabled us to identify the aerodynamic changes resulting from the proximity of the two propellers to each other and to understand the mechanisms causing the changes in the radiated sound. It was discovered that there is a dip in the thrust due to the relative proximity of the rotors. Owing to this, there is also some acoustic banding above the rotors mainly because they operate at the same rotational rate. We then considered the forward flight case and compared it with the corresponding hovering case. This enabled us to identify the aerodynamic changes resulting from the incoming stream. By examining the near acoustic field, the far-field spectra, the Spectral Proper Orthogonal Decomposition, and by conducting periodic averaging, we were able to identify the sources of the changes to the observed tonal and broadband noise. The convection of the oncoming flow

was seen to partially explain the observed enhancement in the tonal and BBN, compared to the hovering case.

It is well known that High fidelity methods are critical in predicting the full spectrum of rotor acoustics. However, these methods can be prohibitively expensive. We present here an investigation of the feasibility of reduction methods such as Proper Orthogonal Decomposition as well as Dynamic Mode decomposition for reduction of data obtained via Hybrid Large-Eddy – Unsteady Reynolds Averaged Navier Stokes approach (HLES) to be used further to obtain additional parameters. Specifically, we investigate how accurate reduced models of the high-fidelity computations can be used to predict the far-field noise. It was found that POD was capable of reconstructing accurately the parameters of interest with 15-40% of the total mode energies, whereas the DMD could only reconstruct primitive parameters such as velocity and pressure loosely. A rank truncation convergence criterion > 99.8% was needed for better performance of the DMD algorithm. In the far-field spectra, DMD could only predict the tonal contents in the lower- mid frequencies whiles the POD could reproduce all frequencies of interest.

Lastly, we develop an active rotor noise control technology to reduce the in-plane thickness noise associated with multi-rotor Advanced Air Mobility Vehicles (AAMV). An actuation signal is determined via the Ffowcs-Williams-Hawking (FWH) formula. Two in-line rotors are considered and we showed that the FWH-determined actuation signal can produce perfect cancellation at a point target. However, the practical need is to achieve noise reduction over an azimuthal zone, not just a single point. To achieve this zonal noise reduction, an optimization technique is developed to determine the required actuation signal produced by the on-blade distribution of embedded actuators on the two rotors. For the specific geometry considered

here, this produced about 9 dB reduction in the in-plane thickness noise during forward flight of the two rotors. We further developed a technology that replaces using a point actuator on each bladed by distributed micro actuators system to achieve the same noise reduction goal with significantly reduced loading amplitudes per actuator.

Overall, this research deepens the knowledge base of multi-rotor interaction. We utilize several techniques for extracting various flow and acoustic features that help understand the dynamics of such systems. Additionally, we provide a more practical approach to active rotor noise control without a performace penalty to the rotor system.

TABLE OF CONTENTS

LIST OF FIGURES

LIST OF TABLES

NOMENCLATURE

a_∞ , c_o	Ambient speed of sound
C_T	Coefficient of thrust
C_{tip}	Rotor tip chord
e_t	Total energy
L_i	Loading components of vector defined in eq. (3.22)
L_M	$L_i M_i$
L_r	$L_i \hat{r}_i$
$\dot{L}_r$	Time derivative of L_r, $\dot{L}_i \hat{r}_i$
M	Local Mach number vector of source, with components M_i
M_r	Mach number of source in radiation direction, $M_i \hat{r}_i$
$\hat{n}_i$	Component of unit outward normal vector to surface
p'	Acoustic pressure, $p - p_{time\ average}$
P_{ij}	Compressive stress tensor
q_j	Heat flux
R	Rotor radius
r	Distance between observer and source, $\|x\text{-}y\|$
$\hat{r}_i$	Component of unit vector in radiation direction

Re	Reynolds number
S_{ij}	Strain rate tensor
T_{ij}	Lighthill stress tensor, $\rho' u_i u_j + (p' - c_0^2 \rho')\delta_{ij} - \sigma_{ij}$
T	Ambient temperature
t	Observer time
U_i	components of vector defined in eq. (3.22)
U_n	$U_i \hat{n}_i$
$U_{\dot{n}}$	$U_i \dot{\hat{n}}_i$
$\dot{U}_n$	time derivative of U_n, $\dot{U}_i \hat{n}_i$
u_i	components of local fluid velocity
u_n	normal component of local fluid velocity
v_n	local normal velocity of source surface
w_p	wave speed
δ_{ij}	Kronecker delta, 1 for i=j, otherwise 0
κ	Karman constant
μ	laminar viscosity
ν_t	turbulent eddy viscosity
$\tilde{\nu}$	modified eddy viscosity

ρ	density
σ_{ij}, τ_{ij}	viscous stress tensor
τ	source time
ϕ	mass flux
Ψ	low Reynolds number correction term
Ω	vorticity magnitude

1 Introduction

The projected increase in Advanced-Air-Mobility Vehicles (AAMV), such as Electrical Vertical-Take-Off and Landing (eVTOLs), has necessitated the need to focus on reduction of the noise associated with such systems to address the adverse effect on community as highlighted by several NASA workshops [1]. Progress in its implementation is hindered by the concerns about its safety and the associated noise annoyance near vertiports [2–6]. From an aerodynamic point of view, the most safety-critical situations for civilian aircraft are during takeoff and landing. The Federal Aviation Administration (FAA), as well as other international aviation regulators have imposed stringent regulations on aircraft noise [7]. For these regulations to be met, AAMV vehicles would have to be significantly quieter. It can easily be seen that with the assumption of the onset of the age of personal flying cars, there would be detrimental effects of noise on human health. Noise has been related to permanent hearing loss [3], sleep disorders [4], mental [5] and cognitive issues [6], to say the least. Realizing that aircraft noise is also a health-safety hazard to populations around airports, the FAA has modified the aircrafts takeoff and landing operations around airports to minimize the noise impact on the populations around airports, thus aero-safety and aero-noise are coupled. More so, in several military applications, stealth of UAM vehicles is a must.

Propellers are usually used for propulsion and are mostly powered by an electric or hybrid-electric source. Small AAMV usually carry no people and fly at low- to mid- altitude, while the eVTOL carries people (less than 6) and flies on-demand in low altitudes between vertiports at urban areas. Some literatures classify these vehicles in terms of passenger capacity or maximum takeoff weight [8], or by size (see Figure 1-1). Most of these aerial vehicles have multiples of rotors with some vehicles such as the Volocopter air taxi having as many as 18 rotors. Several

complications arise from the aerodynamic and aero-acoustic point of view for these multi-rotor systems. One of the goals of this research is to investigate the dominant noise sources for such systems through high-fidelity modeling. After this knowledge has been established, we would then attempt to mitigate some of the noise sources via active noise control.

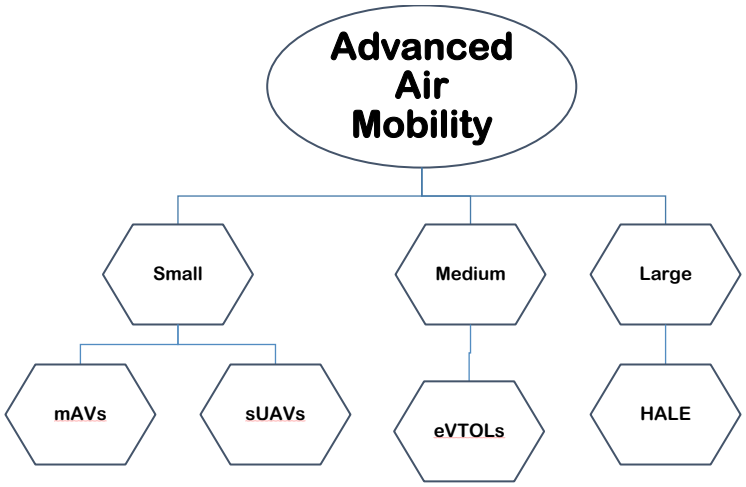

Figure 1-1 Classification of Urban Air Mobility based on size.

1.1 Review of Relevant Literature for Multi-Rotor Noise Prediction

To begin, we briefly discuss the general noise sources for rotor systems. Noise radiated by rotors is composed of tonal noise and Broad-Band Noise (BBN). Tonal noise occurs at discrete frequencies, while BBN extends over a wide range of frequencies. The propeller tonal noise is usually split into loading noise and thickness noise and is characterized by sharp tonal noise at the Blade-Passing-Frequency (BPF) and its harmonics. The BBN is created by turbulence effects and non-linearities in the flow [9] and originates from various sources, including, the turbulent leading or trailing edge of the boundary layer, and separation effects, among other sources (see Figure 1-2). Tonal noise is well studied, but the broadband noise is not easily computed. In the case of AAMV, due to multi-rotor interactions, and unsteady operations, BBN may be of the same order

as tonal noise. As such, the NASA AAMV-Working Noise Group [10] has indicated that there is need to develop schemes to predict broadband noise that rely less on empirical data.

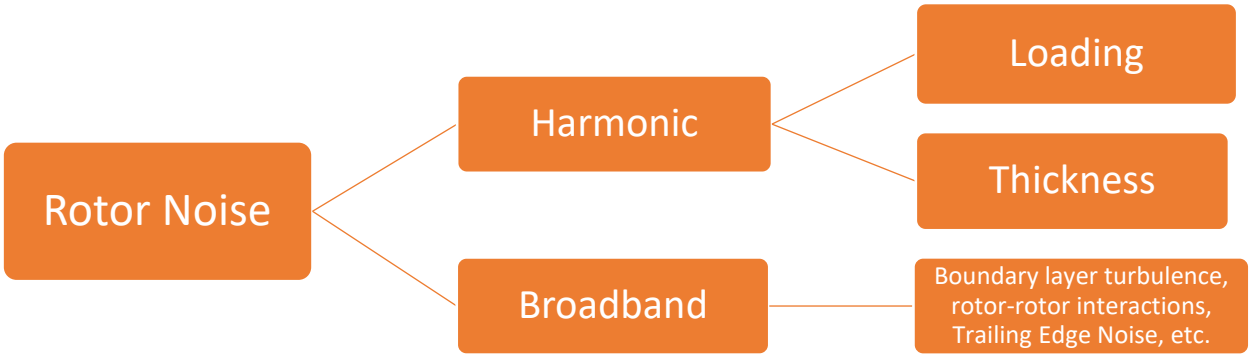

Figure 1-2 Schematic of Propeller Noise Sources

Noise generated by an isolated rotor at hovering conditions has been studied both experimentally as well as numerically by Zawodny et. al [11], and Mankbadi et al. [12]. It was found that the broadband levels in the low-mid frequency range were significant. Also, an investigation into the broadband noise sources revealed that the wake was a significant contributor, as well as the unsteady pressure on the blade surface and trailing edge noise. In forward flight conditions, several researchers have performed both experimental and preliminary numerical studies. Yang et al. [13] considered an isolated rotor in flight. Their data showed that both the tonal and broadband noise increases with either increasing the flight speed or the rotor's tilt angle relative to the free stream.

AAMV are characterized by multiple rotors near each other as well as to the wing and fuselage. Rotor Interactions (see Figure 1-3) can be classified as rotor-rotor interactions or rotor interaction with other structures than the rotor, such as the wing or the fuselage. Rotor-wing or rotor-fuselage interaction would require resolving complex geometries and including scattering effects. In conventional rotorcraft, this is usually less of a noise source and more of an influence on the trim

state of the vehicle because the rotors are not close to wings. In many AAMV vehicles, rotors and propellers are close to wings. This proximity allows blade passage effects on the flow field of the wing, causing unsteady loading on the wing, which function as a noise source [14]. Also, If the rotors are behind the wing or fuselage, then the rotor ingests the wake from the wing or fuselage, increasing the unsteady loading noise from the rotor, resulting in fuselage wake noise. Due to the number of rotors and placement on many proposed AAMV vehicles, this is anticipated to be more important sources than in conventional rotorcraft. Since the wake can be composed of a periodic or turbulent structure, this interaction can lead to both tonal and broadband noise [15].

Noise generation for such multi-rotor vehicle is highly dependent on the tip Mach number and Reynolds number of the flow. At high tip Mach numbers, $M_{tip} > 0.65$, the thickness noise dominates the total noise levels. However, as the tip Mach number reduces, the relative importance of broadband noise becomes prevalent especially at $M_{tip} \leq 0.5$ [16]. The broadband noise is primarily generated by the unsteady pressure fluctuations of the blade surface, as well as the increase in turbulent boundary layer interactions with an increase in the sectional blade angle of attack. The steady loading noise is discussed to be primarily generated by the convective amplification of the flow in forward flight, as well as the steady pressure differentials responsible for the rotor thrust.

Several experimental investigations have been conducted to examine the Multi-Rotor-Interaction (MRI) noise at hover conditions. Experimental observations have shown several interesting features: Both the tonal and broadband noise were found to increase due to the interaction and that the effect decreases as the separation distance increases [17,18]. The directivity pattern is seen to be omni directional in the plane of rotation [19]. Again, in forward flight, detailed studies were conducted by Zawodny & Pettingill [20], Intaratep et. al [21], Wang et al. [22] and

Alexander & Crofton [23], among others. These works have investigated the acoustic characteristics of a representative multicopter system in simulated forward flight conditions. The experiments revealed several interesting features, such as the effect of wake generated by one propeller on the broadband noise of the other rear rotor, tonal noise interactions, and how the directivity pattern changes with rotor-rotor interactions. On the numerical side, Lee & Lee [24] studied MRI in forward flight by simplifying the governing equations using the vortex lattice approach.

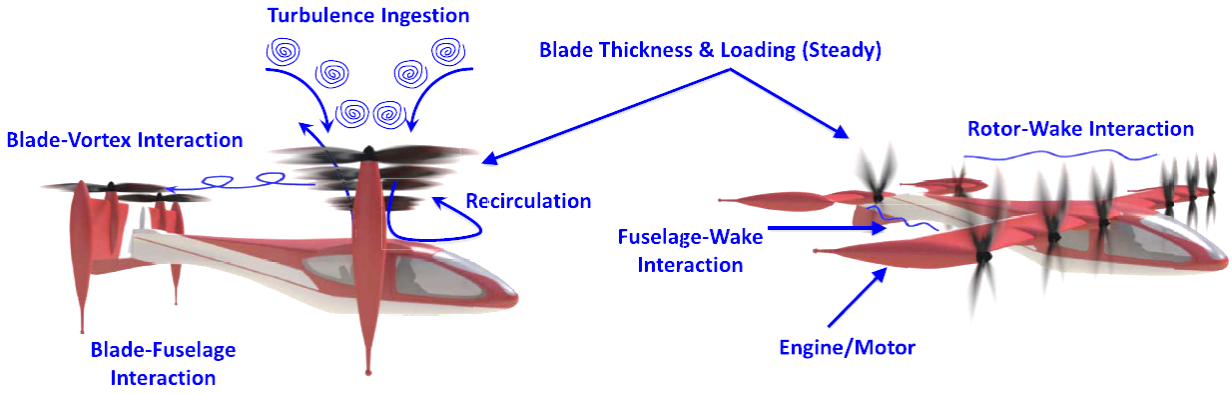

Figure 1-3 Schematic of various multi-rotor noise sources [10]

There are several levels of fidelity in noise predictions. High-Fidelity studies such as the computations performed by Diaz et al. [25] are quite expensive. Full configuration of a small-scale UAS with a fuselage was simulated by Cadieux et. al[26].They also mention that the computation was CPU intensive. Faster methods exist such as the nonlinear vortex lattice method [24,27], as well as the semi-empirical approach of ANOPP [28]. However, these methods can be limited in accuracy (e.g., Rizzi et al. [29]).

As aforementioned, LES computations are quite resource intensive. In several use cases, especially in acoustic processing, the simulations may need to be run again to collect data or information for different target observer locations. To avoid multiple runs of the same case, we

look at the feasibility of reduction methods and models for reproducing such high-fidelity data for reuse.

Recently, advances in data science and machine learning have provided opportunities to apply these relatively new technologies to CFD. Using modal decomposition, we can approximate the resulting flow field using Proper Orthogonal Decomposition (POD)[30,31], Spectral POD [32], and Dynamic Mode Decomposition (DMD) [33,34]. Traditionally, such methods have been used to reconstruct flow fields with inputs either from experiments or CFD. Several researchers have utilized POD methods to understand the physics of various flows such as cavity flows [35], pitching airfoils [36] to name a few. Towne & Schmitz utilized Spectral POD methods to investigate the coherent structures of a jet. Countless researchers have utilized DMD for various studies. Rowley & Dawson [37] provide an extensive review of these models and their utilization in great detail. Generally, reduced order models are generally used for either an interpolation type case, usually PODs [38,39], or an extrapolation type case, usually DMDs, with very few extensions of POD for extrapolation over the years [40,41].

Originally, the POD originates from the field of turbulence and was first introduced by Lumley [30,31]. This technique attempts to decompose a random vector field into a set of deterministic functions that capture some fractions of the original data. It essentially reduces the order of the fidelity whiles attempting to retain the “important” features of the flow. POD attempts to find spatial correlations in the flow and to find low rank number of modes to reconstruct the original data. One of the advantages of POD is the ability to provide a straightforward ranking of the weight of each mode of the data set but presents some limitations in resolving heavily time dependent systems or structures in the flow. To remedy this, the DMD algorithm[34] was introduced.

DMD computes the set of dynamic modes which are each associated with a frequency and a decay/growth rate. It is useful for finding correlations with coherent structures in the domain and has the capability to consider the temporal dimension as well in the form of a Fast Fourier Transform (FFT), however, there is no simple way to rank the generated modes, which would be discussed further in Section 3. Another prong of this research is to investigate how feasible these modeling techniques are in modeling the high-fidelity aerodynamics and aeroacoustics of a rotor in hover as a starting point.

1.2 Review of Relevant Literature for Active Rotor Noise Control

Rotor noise can generally be categorized into mechanical (engine, motor, and transmission) and aerodynamic noise, but our concern here is the aerodynamically- generated noise. This in turn can be divided into deterministic (tonal) noise, and non-deterministic (broadband) noise[42]. The tonal noise is usually split into thickness and loading noise. Broadband Noise (BBN) comprises turbulence noise, rotor self-noise, blade-wake interaction noise, and other sources.

Several ideas have been spurned to passively reduce the noise signatures of propellers over the past decade. For tonal noise reduction, Lu, et al. [43] researched on the use of ducts with acoustic absorption materials to reduce the noise. They tested two ducts – one with perforated internal walls and one without perforations. Both ducts showed deleterious effects in thrust, with a 10-20% reduction in thrust, and overall noise level increase of ~5 -10 dBA. Stacking two propellers on top of each other was found to increase the overall propulsive efficiency[44,45]. Loss of thrust and propulsive efficiency was observed in the front (or top) propeller [45], while an increase in thrust and propulsive efficiency was observed for the bottom propeller. Diaz et al.[46] investigated the effects of ducts on coaxial rotors in hover using high-fidelity CFD [46]. They performed some

qualitative acoustic analysis on the various configurations evaluated and saw that placing the duct around the lower propeller of the coaxial system resulted in reduced acoustic signature. For the same thrust, increasing the number of blades reduces the tonal noise. Increasing the number of blades from two blades to four blades resulted in 10 dB reduction, but also increases the frequency of the noise [47]. This may increase the broadband noise floor, and hence increase the perceived noise level. Unequal blade spacings were found to diminish tones at the BPF harmonics [47]. Reducing the diameter of the propeller reduces the tip Mach number for a given rotational rate and the noise as well. A tip Mach number reduction from $M_T = 0.6$ to $M_T = 0.53$ was seen to have an acoustic energy difference of 6 dB [47].

Leslie, et al. [16] investigated the main sources of broadband noise for small scale propellers at low Reynolds numbers and found it to be a result of the trailing edge boundary layer thickness caused by a laminar separation bubble on the suction side of the propeller. They used a leading-edge trip and serrations placed prior to the laminar separation to reduce trailing edge thickness which resulted in a decrease in turbulent boundary-layer trailing edge noise. They reported an overall broadband reduction of up to 4 dB in static tests. An important takeaway mentioned is that this method would only be effective for cases where there was a presence of a laminar separation bubble, which was mentioned to be the case only for cruise conditions, and thus would perform poorly for take-off conditions where blade loading is highest. Other passive control methods such as reducing tip speed by using small-diameter rotors, increasing the blade count, using serrated trailing edges [48], to name a few, have been suggested and tested with some limited results. Phase synchronization has been explored as a possible noise reduction technique that leverages destructive interference of coherent (tonal) acoustic source field between a system of propellers rotating at equivalent rates. The overall directivity of the blade passage frequency noise can be

modified, with a reduction as high as 28.6 dB recorded [49]. Generally, noise reduction from passive methods has limited successes whiles limiting in some cases the aerodynamic performance of the rotors. As such a more active control method is desired.

Active Noise Control (ANC) is an alternative approach that differs from the passive techniques, in that it is engaged only when needed. Since AAMV noise may be particularly critical as it approaches the target observer, or during take-off and landing, ANC may be an appropriate technology.

The notional principle that the sound pressure can be mitigated by superimposing a secondary noise source that is in phase with but opposite in amplitude to the primary source was first introduced by Lueg [50]. Lueg's idea developed eventually into the field of active noise control. Three main classification of active noise control mechanisms were devised – Zone Control, On-blade or source modification, and sound absorption [51]. For simplicity, the sound absorption mechanism would be omitted as it pertains mainly to the fuselage/cabin noise control.

1.2.1 Zone Control

The first type of ANC is sound field cancellation or zone control. To execute a zone control, a zone of silence is needed around the sound source. One method for achieving this is the use of anti-noise. The basic principle is that if the noise at the target point is a simple wave, one can impose an identical wave to it with a 180 degrees phase shift to cancel it. A perfect application of this mechanism is the noise cancelling headphones, first developed by Meeker of RCA [52]. Practical applications of this kind of mechanism are limited to relatively enclosed regions. Usually, a feedback loop is needed. A sensor measures the radiated sound, which is fed into a microprocessor to determine the anti-noise signal needed for sound suppression. Complete cancellation at a given point, in principle, can be achieved via an iterative process through the

feedback mechanism. Ikelheimer & Nagel [53] considered a propeller surrounded by four speakers to create a zone of silence. The method worked best at the specific target location, but other locations saw increases in the sound pressure level. Increasing the number of speakers was found to be more effective. Deviating slightly from rotors, some successes have been seen in experiments by Koopmann et al. [54] with 10-20 dB noise reductions in centrifugal fans. This technique becomes unfeasible for open rotors as it would require a high acoustic impedance to counter the noise source for every observer location [53].

1.2.2 On-Blade Actuation

The second type of ANC is the modification or suppression of the sound generation, is the case where a modification is done on the blade to alter the radiation impedance of the original noise source for acoustic mitigation. Most active rotor noise control ideas fall under this mechanism or classification. Several decades of research and studies were directed towards BVI noise reduction, vibration reduction, and performance enhancement [55–57]. On-blade active rotor control methods such as higher harmonic control (HHC), individual blade control (IBC), trailing edge flap (TEF), blowing on or near the rotor blade have been tested as potential ways of altering the wake structure, and subsequently the reduction of the BVI effects [56].

Higher harmonic control system is an active vibration control mechanism where the rotor blades are oscillated at higher harmonics of the rotational speed. Although originally devised as a method for vibrational reduction, it was suggested as a potential method for reducing BVI in the late 1980s [57]. However, it was determined that when implemented, fuselage vibration levels were drastically increased when driven at low BVI noise frequencies[58,59]. This can be reduced by applying the excitation at a higher harmonic frequency, which ultimately led to the development of the individual blade control methods. eVTOLs are generally scaled down variants of rotorcrafts

with multiple rotor systems. Applying this method of active rotor control might prove quite deleterious as the vibrations or excitation of the oscillations from all the rotors might introduce some structural issues and may reduce the level of comfort in the fuselage/cabin. Several active control research have been done particularly for helicopter rotors with little to none done for small-scale rotors for UAVs. However, we review a few techniques and their feasibility and successes.

Anobile et al.[60] developed a low-frequency controller geared towards reducing helicopter rotor BVI noise. They utilized an active twist rotor concept via torque load distributions at 2/rev frequency. They applied this methodology numerically to a scaled Bo-105 4-bladed helicopter main rotor, with a radius of 2 meters, a constant chord of 0.212 meters, linear twist of -8 degrees, and a rotational speed of 109 rad/s. The general Kussner-Schwarz theory was employed to determine the unsteady aerodynamic loads associated with the profile downwash. Aeroelastic computations were performed to account for the blade deformation and its effects on the wake. The wake inflow was then predicted using a free-wake boundary element solver. They performed an open-loop control using the active twist, which showed that a 2/rev actuation was effective in reducing the BVI sound pressure level by about 2 dB. However, this also resulted in an increase in vibratory loads and low frequency noise of about 3 dB. Using the microphones below helicopter and at the skid ends, a closed loop controller was developed which resulted in a maximum BVI sound pressure level reduction of 6 dB at the retreating side.

Generally, for rotorcrafts in forward flight, it is quite known that the in-plane thickness noise is especially important and has been shown to be partly due to the blade vortex interaction (BVI) [55]. Helicopters usually operate at relatively low altitudes, with the rotor disk slightly tilted downward. This is similar to the flight attitude of UAVs. For this reason, in-plane rotor noise levels are high and radiates mainly at the lower frequencies that propagate at much larger distances.

Alluding to the more recent eVTOLs that would be in this flight envelope, it is imperative that this in-plane rotor noise be alleviated. We explore here some of the methods devised over the years in reducing the thickness noise.

One of the earliest proven tests of the concept of on-blade actuation for harmonic noise control was the full-scale "Boeing SMART" rotor [61]. They utilized an active trailing edge flap for the blade noise control. The results showed that placing the controls near the tips is an effective thickness noise control, with the total thickness noise reduced to about 50% in amplitude.

Sargent & Schmitz [55,62,63] performed experiments with a 1/7th scale rotor, where they used tip mass ejection to attempt to reduce specifically the in-plane thickness noise. They implement this by extracting out the mass flow rate equation and comparing with the Ffowcs-Williams Hawking (FWH) equation [64]. For an idealized point source ejecting mass into a quiescent medium, the jet mass flow rate is given as [63]:

$$\dot{m}_{jet} = \rho_{jet} A_{jet} V_{jet} \tag{1.1}$$

With velocity of source moving with respect to the medium $\vec{V}_{source} = \vec{\Omega}\ x\ \vec{r}_{jet} + \vec{V}_{\infty}$.

Assuming $\rho_{jet} = \rho_0$ then:

$$\vec{F}_{jet} = \dot{m}_{jet}\left(\vec{V}_{jet} + \vec{V}_{source}\right) = \dot{m}_{jet}\left(\vec{V}_{jet} + \vec{\Omega}\ x\ \vec{r}_{jet} + \vec{V}_{\infty}\right) \tag{1.2}$$

The anti-noise acoustic pressure was derived to be the combination of the pressure due to the mass injection term, and that due to the momentum injection. They utilized a cumbersome jet powered by a compressor which was ducted through the blades. For actuation, they explored two main valve control techniques. The first was generating a sinusoidal jet by applying a sine voltage to the pneumatic motors. They noticed a lag and difference in the actual amplitude of the jet which affected the amplitude of the anti-noise. This also affected the harmonic of the wave as it generated a 2 per rev excitation. Next, they explored a single pulse valve control. This generated a 3-per rev

harmonic, which meant a higher rate of change of the jet, and thus increased the peak amplitude and decreased the pulse width. Overall, this method resulted in a reduction of the peak negative amplitude of the test rotor's radiated noise by 5 Pa at the target microphone but was impractical as the required mass flow rate needed required a high exit jet velocity profile.

Another approach was performed by Shi et al [65]. They explored the use of trailing edge winglets for unsteady force excitation. This method specifically looks to target the rotor thickness noise. This involved the application of unsteady aerodynamic forces to excite a secondary or anti-sound wave. This excitation was done with the use of a trailing edge winglet near the tip of the rotor. A harmonic formulation for prescribing the motion of the trailing edge winglet actuator was devised:

$$F = F_n \sin(n\psi + \psi_o) \tag{1.3}$$

where F_n is amplitude, n is the harmonic, ψ & ψ_o are azimuthal angle and initial excitation angle. The limitations of this approach were that the formulation of the anti-noise actuation depends on the correct amplitude of the forcing function, F_n, the harmonic number, and the phase angle. There was no direct correlation to obtain the exact wave form without experimentation.

Yang et al [66] tackled the problem by relating the in-plane thickness noise to a point source loading noise formulation. From the Differential form of the FWH[64], the loading noise is given as:

$$p_L'(x,t) = \frac{1}{4\pi c_0}\left[\frac{1}{r(1-M_r)^2}\frac{\partial L_r}{\partial \tau} + \frac{c_0 L_r}{r^2(1-M_r)} + \frac{L_r\left(r\dot{M}_r + c_0 M_r - c_O M^2\right)}{r^2(1-M_r)^3}\right]_{ret} \tag{1.4}$$

By equating the thickness noise at an observer to the loading noise:

$$p_L'(x,t) = -p_T'(x,t) \tag{1.5}$$

This was then reformulated as a first order ordinary differential equation (ODE), the solution of which is the loading anti-noise signal needed to cancel the in-plane thickness noise for a target

observer. This technique was implemented both numerically and experimentally using a flap for a single observer and a single rotor blade. They tested two actuators – an active flap and a winglet on the blades and found that the active flap resulted in about 3dB noise reduction over an azimuth range of 150 to 210 degrees, and the winglet showed more than 6dB reduction over an azimuthal range of 120 to 240 degrees in the rotor plane.

All the discussed methods have proven to be successful in cancelling thickness noise, but the practicality of the applications is still questionable. The use of the active flaps showed great promise, but its effects on the blade loading and performance, as well as the structural integrity of the blades is yet to be understood. Also, the methods discussed have all been tested on single rotor blades, and thus their applicability in multi-bladed and multi-rotor systems must be explored.

1.3 Research Objectives

The main objectives of the current dissertation are presented here:

- Simulations of multi-rotor interaction noise at hovering & forward flight conditions. With the onset of the age of advanced air mobility vehicles, there are several limitations to the design of these AAMVs. One such limitation is the noise it would generate. The noise generated by these multi-rotor systems becomes increasingly complicated. We set out to explore, using high-fidelity computational methods, the various noise sources for multi-rotor systems. The complex dynamics of the wake and rotor systems require careful grid generation, selection of numerically accurate schemes, and turbulent models as well as non-reflective boundary treatments. We take a look at the aerodynamics of such systems as well as the near and far-field aeroacoustics for both hovering rotors and rotors in forward flight.

- Application of Data Reduction methodologies to rotor noise prediction. As discussed earlier, accurate predictions of multi-rotor systems require very high fidelity in the form of either HLES or pure LES computations, which are both computationally and storage intensive. Especially for acoustics, it requires a predetermined knowledge of the target observers. However, after this computation has been run, there is no way of revisiting the case, for further processing at a different observer location, as for most solvers, the intermediary surface integration is not stored. Another prong of this dissertation is to investigate the feasibility of data reduction methods – POD and DMD, and how they can model the highly unsteady flow field of a rotor in hover as a model problem, as well as their ability to regenerate data on the fly for far-field acoustic predictions.
- Development of Active noise control of multi-rotor advance air mobility vehicles. After the dynamics and relative importance of the noise sources are understood, we take a look at an active technique for reducing, as a model case, the in-plane thickness noise using embedded actuators. Extension formulations are developed using FWH equations that can cancel the noise of multirotor systems and for a target zone of observers. One of the main challenges of this approach is that obtaining a simple anti-noise signal for a target zone is no easy feat. This is because each target location relative to the source is phase-shifted from each other. As such to find a feasible solution, a complex fitness function has to be developed using a genetic algorithm to find a global minima for the total noise for the specified target zone. With the proof of concept developed, the feasibility and practicality of this method will then be explored, and some modifications or corrections would be introduced.

1.4 Dissertation Organization

In this subsection, we discuss briefly the organization and overview of this dissertation. The dissertation would be split mainly into three parts. Chapter 2 tackles the high-fidelity computations of multi-rotor aerodynamics and noise in hover and forward flight conditions. The specific research goals are discussed in this chapter. Next, the numerical approach is described. The governing equations, the numerical scheme, and turbulence modeling techniques are explained. The boundary treatment and the computational grid are then discussed to highlight the acoustic requirements of the grid and to avoid numerical reflections at the boundaries. A grid sensitivity study is then provided to identify the grid density threshold. The acoustic theory and formulations are then discussed in detail.

The subsequent sections in Chapter 2 discuss the results of a comparison between a single rotor and two rotors of the same geometry in hover. The aerodynamic and acoustics properties and features are then highlighted and explained. Next, the results of two rotor systems in hover and in forwarding flight are presented. The results are compared with experimental data, and some acoustic and aerodynamic observations are made and discussed. An interim conclusion of this part of the research is presented in the last subsection of chapter 2.

In Chapter 3, the second part of the dissertation is presented. A reduced order modeling approach for a model single rotor in hover is discussed. The various formulations for POD and DMD are presented. Additionally, the mode truncation problem is introduced, and solutions to the problem are also discussed. Next, the modeling approach and workflow is discussed. The approach for extracting the relevant data from the HLES computations in OpenFOAM is detailed here. The subsequent subsections discuss the results of the computed reduced order model in reproducing the aerodynamic parameters of the HLES, and their limitations. The far-field acoustic performance

of the models is presented, and their inherent limitations are also discussed. Again, an interim conclusion is presented for this study.

In Chapter 4, the third and final part of the dissertation is presented. An active rotor noise control methodology is devised and discussed here. First, the problem statement is described in detail. Then the thickness noise prediction formulations are discussed with a benchmark case used for validation. Next, the multi-rotor formulations of the anti-noise signal for a single target observer is presented. The results of this are also shown to prove that the formulations perform as expected. The formulation is then extended to a zone of target observers, where again this is tested for a model case of two 2-bladed rotors in forward flight. The results of the zone actuation formulation are presented after which the practicality of the formulation is discussed. An embedded distributed array of actuators approach is presented, and the formulations for the multi-rotor system are modified. Again, this practical application is verified using the same model case. An interim conclusion is follows, discussing the prospects of this methodology.

In Chapter 5, the overall conclusions and general outlook of the research are discussed. The key findings for each of the prongs of the dissertation are summarized here, with some suggestions for the future continual studies of the research provided here. A list of all the publications for the research is provided after Chapter 5.

2 Simulations of Multi-rotor Interaction Noise

The focus of this research is to unravel the physics of multi-rotor interactions and their noise sources in a typical small-scale UAV configuration. Unsteady RANS (URANS) methods can predict tonal noise levels but cannot predict broadband noise. The other spectrum of fidelity is the Large Eddy Simulations (LES), which can predict all of the noise sources, but is computationally prohibitive. As such, a Hybrid Unsteady RANS – LES (HLES) approach is devised here and utilized for this study for the near field flow and acoustic resolution. Using the Ffowcs-Williams-Hawkings equations, specifically the Farassat's 1A formulation, the near field is extended to the far-field acoustics.

2.1 Numerical Approach

For this study, the hybrid unsteady RANS-LES (HLES) method is utilized for the flow field resolution. This approach is selected as an intermediary between accuracy and computational cost because we solve unsteady Reynolds averaged equations near the wall, and a Smagorinsky-like set of equations away from the wall.

2.1.1 Governing Equations

The governing equations for the entire computational domain are the compressible, unsteady Favre-Averaged Navier-Stokes equations [67]:

$$\frac{\partial \bar{\rho}}{\partial t} + \frac{\partial}{\partial x_i}[\bar{\rho}\widetilde{u_\iota}] = 0 \tag{2.1}$$

$$\frac{\partial}{\partial t}(\bar{\rho}\widetilde{u_\iota}) + \frac{\partial}{\partial x_j}\left[\bar{\rho}\widetilde{u_j}\widetilde{u_\iota} + \bar{p}\delta_{ij} - \widetilde{\tau_{j\iota}^{tot}}\right] = 0 \tag{2.2}$$

$$\frac{\partial}{\partial t}(\bar{\rho}\widetilde{e_t}) + \frac{\partial}{\partial x_j}\left[\bar{\rho}\widetilde{u_j}\widetilde{e_t} + \bar{p}\widetilde{u_j} + \widetilde{q_j^{tot}} - \widetilde{u_\iota}\widetilde{\tau_{j\iota}^{tot}}\right] = 0 \tag{2.3}$$

where:

$$\widetilde{\tau_{ji}^{tot}} = \widetilde{\tau_{ji}^{lam}} + \widetilde{\tau_{ji}^{turb}} \tag{2.4}$$

$$\widetilde{\tau_{ji}^{turb}} \equiv -\overline{\rho u_i' u_j'} \approx 2\nu_t \left(S_{ij} - \frac{1}{3}\frac{\partial u_k}{\partial x_k}\delta_{ij} \right) - {}^2/_3\, \bar{\rho} k \delta_{ij} \tag{2.5}$$

$\widetilde{e_t}$ is the total energy, $\widetilde{q_j^{tot}}$ is the total heat flux, and $\widetilde{\tau_{ji}^{tot}}$ is the total viscous stress term, and S_{ij} is the strain rate tensor, with:

$$S_{ij} = \frac{1}{2}\left(\frac{\partial u_i}{\partial x_j} + \frac{\partial u_j}{\partial x_i} \right) \tag{2.6}$$

The term ν_t is the turbulent eddy viscosity = $\rho\mu_t$, and k is the modeled turbulent kinetic energy (TKE) which is a measure of the energy contained in a turbulent flow, and is defined as:

$$k = \frac{1}{2}\left(\overline{u_1' u_1'} + \overline{u_2' u_2'} + \overline{u_3' u_3'} \right) \tag{2.7}$$

2.1.2 HLES Turbulence Modeling

The goal of the turbulence model is to get an approximation to the stress term, τ_{ij} in the above governing equations. As aforementioned, two sets of equations are solved based on the location and distance from the wall.

In the near-wall region, URANS is utilized. The turbulent viscous stresses τ_{ij} are modeled using the one equation Spalart-Allmaras turbulence model[68]. This model has been shown to accurately predict the flow of small-scale rotors [12,25,69], and thus is used in this study. The model uses the Boussinesq approximation, which relates the Reynolds stresses to the turbulent eddy viscosity. The eddy viscosity ν_t is obtained by first calculating a modified eddy viscosity ($\tilde{\nu}$) through the transport equation:

$$\frac{\partial \tilde{\nu}}{\partial t} + u_i \frac{\partial \tilde{\nu}}{\partial x_j} = \underbrace{c_{b1}(1 - f_{t2})\tilde{S}\tilde{\nu}}_{\text{Production}} - \underbrace{\left[c_{w1} f_w - \frac{c_{b1}}{\kappa^2} f_{t2} \right]\left(\frac{\tilde{\nu}}{d} \right)^2}_{\text{Destruction}} + \underbrace{\frac{1}{\sigma}\left[\frac{\partial}{\partial x_j}\left((\nu + \tilde{\nu})\frac{\partial \tilde{\nu}}{\partial x_j} \right) + c_{b2}\frac{\partial \tilde{\nu}}{\partial x_i}\frac{\partial \tilde{\nu}}{\partial x_j} \right]}_{\text{Dissipation}} \tag{2.8}$$

Where ν is the kinematic viscosity, and the closure functions are defined as:

$$\tilde{S} = \Omega + \frac{\tilde{\nu}}{\kappa^2 d^2} f_{v2} \tag{2.9}$$

$\tilde{S}$ is the mean strain rate and Ω is the vorticity.

$$f_{v1} = \frac{\chi^3}{\chi^3 + {c_{v1}}^3}; \quad \chi = \frac{\tilde{\nu}}{\nu} \tag{2.10}$$

$$f_{v2} = \frac{\chi}{1 + \chi f_{v1}}; \quad f_{t2} = c_{t3} \exp(-c_{t4}\chi^2); \quad f_w = g\left[\frac{1 + {c_{w3}}^6}{g^6 + {c_{w3}}^6}\right]^{1/6} \tag{2.11}$$

$$c_{w1} = \frac{c_{b1}}{\kappa^2} + \frac{1 + c_{b2}}{\sigma};\ g = r + c_{w2}(r^6 - r);\ r = min\left[\frac{\tilde{\nu}}{\tilde{S}\kappa^2 d^2}, 10\right] \tag{2.12}$$

Here κ is the Karman constant. The eddy viscosity is computed as $\nu_t = \tilde{\nu} f_{v1}$. The turbulence length scale $\boldsymbol{d}$ seen in Eq. (2.9) and Eq. (2.12) is defined as the distance to the nearest wall. The model coefficients are given as:

$$\boldsymbol{c_{b1}} = 0.1355;\ \boldsymbol{c_{b2}} = 0.622;\ \boldsymbol{\kappa} = 0.41, \boldsymbol{\sigma} = {}^2/_3;\ \boldsymbol{c_{t3}} = 1.2;\ \boldsymbol{c_{t4}} = 0.5;\ \boldsymbol{c_{w2}} = 0.3, and\ \boldsymbol{c_{w3}} = 2. \tag{2.13}$$

To account for rotation and curvature of the wake physics, a rotation/curvature correction term f_{r1} is multiplied by the production term of the transport equation as suggested by Shur et. al [70]:

$$f_{r1}(r^*, \hat{r}) = (1 + c_{r1})\frac{2r^*}{1 + r^*}[1 - c_{r3} tan^{-1}(c_{r2}\hat{r})] - c_{r1} \tag{2.14}$$

Where:

$$\mathrm{r}^* = {}^S/_\omega; S = \sqrt{2S_{ij}S_{ij}};\ and\ \omega = \sqrt{2\omega_{ij}\omega_{ij}} \tag{2.15}$$

$$S_{ij} = 0.5 * \left(\frac{\partial u_i}{\partial x_j} + \frac{\partial u_j}{\partial x_i}\right); and\ \omega_{ij} = 0.5 * \left(\left(\frac{\partial u_i}{\partial x_j} - \frac{\partial u_j}{\partial x_i}\right) + 2\varepsilon_{mji}\Omega_m\right) \tag{2.16}$$

$$\hat{r} = \frac{2\omega_{ik}S_{jk}}{D^4}\left(\frac{DS_{ij}}{Dt} + \left(\varepsilon_{imn}S_{jn} + \varepsilon_{jmn}S_{in}\right)\Omega_m\right); \text{with } D^2 = 0.5(S^2 + \omega^2) \tag{2.17}$$

DS_{ij}/Dt are the components of the Lagrangian derivative of the strain tensor, and ε is the Einstein summation convention. The constants used here are c_{r1}=1.0, c_{r2}=12, and c_{r3}=1.0.

To switch from URANS to LES, we adopt Spalart et al[71] approach in modifying the length scale $\boldsymbol{d}$ used in the Eqs. (2.8), (2.9), & (2.12) to be replaced by the switching function $\tilde{\boldsymbol{d}}$, defined as:

$$\tilde{d} = \min(d, C_{DES}\Delta) \tag{2.18}$$

$\boldsymbol{d}$ is defined as the wall distance, $\boldsymbol{\Delta}$ is defined as the local grid size $= max\left(\Delta_x, \Delta_y, \Delta_z\right)$, and $C_{DES} = 0.65$. The switching mechanism works such that URANS is solved in the near wall region where d < $C_{DES}\Delta$, and solves LES in the outer regions where $d \geq C_{DES}\Delta$, that is:

- In the inner layer, $(d < C_{DES}\Delta) \longrightarrow \tilde{d} = d$
- In the outer layer, $(d \geq C_{DES}\Delta) \longrightarrow \tilde{d} = C_{DES}\Delta$

When the model is switched, the eddy viscosity becomes proportional to the local deformation rate and the turbulence length scale $\tilde{d}$, that is, $\nu_t \propto S\tilde{d}$. The modified transport Eq. (2.8) is then solved using the new length scale. It should be noted that the velocity term u_i changes to the filtered $\bar{u}_i$. This modification transforms the transport equation into a grid-dependent sub-grid scale-like model. The turbulence length scale $\tilde{d}$ acts as an implicit filter, where the larger eddies are resolved, and the smaller eddies are modeled. Thus, the transport equation for the eddy viscosity Eq. (2.8) behaves as a Smagorinsky-like sub-grid scale model in the outer layer and becomes grid dependent.

"Wall proximity" is calculated by the ratio of the eddy viscosity and the molecular viscosities. In the LES region, the sub-grid eddy viscosity decreases with grid refinement, and thus decreases

the flow Reynolds number. To avoid this misinterpretation, a low Reynolds number correction term ψ is introduced into the switching function:

$$\tilde{d} = \min(d, \psi C_{DES}\Delta) \tag{2.19}$$

$$\psi^2 = min\left[10^2, \frac{1 - \frac{1 - C_{b1}}{C_{w1}\kappa^2 f_w^*}[f_{t2} + (1 - f_{t2})f_{v2}]}{f_{v1}\max(10^{-10}, 1 - f_{t2})}\right] \tag{2.20}$$

2.1.3 Solver

The open-source finite volume code, OpenFOAM v1906 is utilized in this study. Owing to the fact that it is a finite volume solver, it integrates between the cell centers. It utilizes the Gauss theorem to convert the volume integrals into surface integrals. Assuming ϕ represents the conservative form of all fluid flow equations, the general transport equation solved is:

$$\int_{Vp} \frac{\partial \rho \phi}{\partial t} dV + \int_{Vp} \nabla \cdot (\rho u \phi) dV - \int_{Vp} \nabla \cdot \left(\rho \Gamma_\phi \nabla \phi\right) dV = \int_{Vp} S_\phi(\phi) dV \tag{2.21}$$

The first term in the equation above represents the temporal derivative, the second term represents the convective term, the third represents diffusion terms, and the last term on the right-hand side is the source terms. Using the Gauss theorem, the volume integrals are converted to surface integrals, which can be represented as summations. The equations are then discretized spatially.

The pressure-based rhoPimpleFOAM, which is a transient compressible PIMPLE solver, is utilized to solve the Navier-Stokes and energy equations. This solver combines the PISO (Pressure Implicit with Splitting of Operator) and SIMPLE (Semi-Implicit Method for Pressure-linked Equations) algorithms. It uses the PISO-like time marching scheme with the pressure-velocity coupling performed in the SIMPLE algorithm. Utilizing this solver allows for flexibility in solution convergence by specifying several pressure correctors per loop. This allows for larger time

stepping without divergence. The PIMPLE solver is utilized with 5 corrector loops per time step and 3 pressure corrections per loop, allowing for convergence of flow parameters per time step. The energy equation is computed using a calorically perfect, sensible enthalpy, and the ideal gas law is used for the equation of state. The laminar viscosity is calculated using Sutherland's law.

The mesh rotation is achieved using the Arbitrary Mesh Interface (AMI) approach where a baffle is specified between rotor and stator regions of the flow. This acts as an interface for transfer of fluid variables between the regions.

OpenFOAM has an advantage of flexibility of the order of numerical discretization scheme to select. For this research, the second order accurate Gauss linear (central differencing) scheme is used for all the spatial derivatives. To advance in time, the implicit, second-order accurate Crank-Nicolson method [72] is utilized. The Crank-Nicolson scheme includes an off-centering coefficient which can be modified to increase stability at the cost of the overall scheme order. For numerical stability, an off-centering coefficient of 0.4 is employed.

2.1.4 Boundary Treatment

The propeller surface is treated as a wall with zero gradient pressure and temperature boundary conditions. A No-Slip boundary condition with a moving wall velocity type is specified for the velocity.

The turbulent eddy viscosity is defined with a "*nutUSpalding*" wall function on the blade surface. This wall function is based on the special relation between y^+ and u^+. The relation is given as follows:

$$y^+ = u^+ + \frac{1}{E}\left[e^{\kappa u^+} - 1 - \kappa u^+ - \frac{1}{2}(\kappa u^+)^2 - \frac{1}{6}(\kappa u^+)^3\right] \tag{2.22}$$

κ is the von Karman constant, and E is 9.8 for smooth walls.

One of the goals of the study is to resolve the near-field acoustics. As such careful boundary treatment is given to the outer walls to avoid reflections. The outer boundaries are modeled as outlets with the Navier-Stokes Characteristic Boundary Condition (NSCBC) implemented in OpenFOAM as a "Wave Transmissive" boundary condition [73]. This is implemented by solving the mass flux (φ) equation at the boundaries:

$$\frac{D\varphi}{Dt} \approx \frac{\partial \varphi}{\partial t} + w_p \frac{\partial \varphi}{\partial n} = 0 \tag{2.23}$$

$$w_p = \frac{\varphi_p}{|S_f|} + \sqrt{\frac{\gamma}{\psi_p}} \tag{2.24}$$

φ_p is the patch face flux, S_f is the patch face area vector, γ is the ratio of specific heats, and ψ_p is the compressibility which is the ratio of pressure and density. The wave speed w_p is computed as the sum of the velocity normal to the boundary and the speed of sound which is calculated from the second term on the right-hand side of Eq. (2.24). Additionally, a 2:1 grid stretching is implemented for further dampening. However, this is still not perfect for most complex flow fields. As such, an additional boundary conditioning is utilized in OpenFOAM using a source called "*acousticDamping*"[74,75]. This introduces an artificial damping source term in the governing equations, and it diminishes the strength of the waves within an absorbing region before they reach the boundaries to eliminate any residual reflections.

2.1.5 Far-field Noise Formulation

As mentioned earlier, one of the goals of this study is to extend the near-field noise to the far-field. There are two major ways of predicting the noise. The most direct method is to extend the nonlinear computational domain to the far-field location. This requires that the flow field be accurately resolved up to the location of interest. Direct methods such as direct numerical simulations (DNS) or large-eddy simulations (LES) are often utilized. This results in a very large

computational domain and requires an exorbitant amount of computational power. A simpler set of equations such as a Euler/Navier-Stokes model, or a full potential model can be used. One of the more common approaches is the integral formulations such as Kirchhoff's method[76,77], and the Ffowcs-Williams-Hawkings Formulations[64]. We utilize the latter in this study. A more general equation was derived for a porous surface as mentioned by Ffowcs Williams and Hawking [64]. Similarly, the quantities on the porous control surface are used to predict the far-field pressure. A complete comparison of the different formulations is discussed by Lyrintzis [77].

In the FWH method, the time histories of all the flow variables are needed for the prediction. The far-field solution is computed using a surface and volume integral which stems from the quadrupole source terms. In many applications of this formulations, especially in the area of rotorcraft aeroacoustics[78], the method has been implemented by taking the control surface to coincide with the surface of the blade or the solid body. However, the method is still valid when the control surface is off the body and is permeable [79].

The FWH equations are derived by manipulating the governing equations to obtain the "generalized equations". They are then combined to obtain a modified wave equation that leads to the integral expression of the porous FWH formulation. The general form of the FWH equations is given as:

$$
\begin{aligned}
4\pi c^2(\rho-\rho_0) = \; & \frac{\partial}{\partial t}\int_S \left[\frac{\rho_0 u_n + (\rho-\rho_0)(u_n - v_n)}{r|1-M_r|}\right]_{ret} dS \\
& + \frac{1}{c}\frac{\partial}{\partial t}\int_S \left[\frac{P'_{ij} + \rho u_r(u_n - v_n)}{r|1-M_r|}\right]_{ret} dS + \int_S \left[\frac{P'_{ij} + \rho u_r(u_n - v_n)}{r^2|1-M_r|}\right]_{ret} dS \\
& + \frac{1}{c^2}\frac{\partial^2}{\partial t^2}\int_V \left[\frac{T_{rr}}{r|1-M_r|}\right]_{ret} dV + \frac{1}{c}\frac{\partial}{\partial t}\int_V \left[\frac{3T_{rr}-T_{ii}}{r^2|1-M_r|}\right]_{ret} dV \\
& + \int_V \left[\frac{3T_{rr}-T_{ii}}{r^3|1-M_r|}\right]_{ret} dV
\end{aligned}
\tag{2.25}
$$

Where $M_r = v_i r_i / c$ is the Mach number in the observer direction, $T_{rr} = T_{ij} r_i r_j$, and $T_{ii} = T_{11} + T_{22} + T_{33}$. Also, V is the volume external to the surface S (f > 0), and the subscript, "ref" denotes the evaluation at the retarded time $\tau^* = t - r/c$. T_{ij} is the Lighthill stress tensor. The above general relation involves volume integrations, which are computationally expensive. As such, to circumvent this, Farassat's Formulation 1A developed by Brentner and Farassat[80] simplifies the equations by neglecting the quadrupole term. The 1A formulation then becomes:

$$4\pi p'(x,t) = \int_{f=0} \left[\frac{\rho_o\left(\dot{U}_n + U_{\dot{n}}\right)}{r(1-M_r)^2}\right]_{ret} dS + \int_{f=0} \left[\frac{\rho_o U_n((r\dot{M}_r + c(M_r - M^2))}{r^2(1-M_r)^3}\right]_{ret} dS$$

$$+ \frac{1}{c}\int_{f=0} \left[\frac{\dot{L}_r}{r(1-M_r)^2}\right]_{ret} dS + \int_{f=0} \left[\frac{L_r - L_M}{r^2(1-M_r)^2}\right]_{ret} dS \tag{2.26}$$

$$+ \frac{1}{c}\int_{f=0} \left[\frac{L_r((r\dot{M}_r + c(M_r - M^2))}{r^2(1-M_r)^3}\right]_{ret} dS$$

$$L_{ij} = P_{ij} + \rho u_i (u_n - v_n) \tag{2.27}$$

$$U_n = \left(1 - {}^{\rho}/_{\rho_o}\right) v_n + \left({}^{\rho}/_{\rho_o}\right) u_n \tag{2.28}$$

U and *M* are the surface motion velocity and Mach number, *r* is the distance between source and observer, *L* is given by Eq. (2.27). $\dot{L}_r, \dot{U}_n,$ and $\dot{M}_r$ represent the source time derivatives. The subscripts *r* or *n* denote a dot product of the vector with the unit vector in the radiation direction $\hat{r}$, or the unit vector in the surface normal direction $\hat{n}$ respectively. The term $L_M = L_i M_i$. The formulation above assumes a control surface where *f*=0.

In Eq. (2.26), the first two terms on the first line represent the thickness noise, which deals with the displacement of the fluid due to the blade geometry. The next set of equations represents the loading noise, which is primarily due to the unsteady pressure difference between the suction and pressure side of the blades. We note that the turbulence sources, as given by Lighthill's stress

tensor, do not appear explicitly in the solution. However, to account for this, we utilize the porous control surface approach, where we encase the sources in a cylindrical control surface. With this approach, we account for the blade, wake, as well as all the turbulent sources in the integration. This formulation is implemented in OpenFOAM using the third-party library, "*libAcoustics"*[81]. To validate this library and approach, a benchmark study was performed and documented in APPENDIX A. We utilize the permeable surface approach [12]. The shape of the control surface is selected to reduce convection of vorticity through the surface. As such, a slanted cylindrical control surface is utilized for the forward case, and a top-capped cylinder utilized for hover cases. The degree of slant was determined by the structure of the inflow velocity. With this numerical approach, the computations should be able to capture periodic noise sources, as well as quadrupole noise sources since we are utilizing a permeable surface approach. Noise sources such as boundary layer noise might not be fully captured due to the hybrid nature of the turbulence and wall modeling and may only capture low frequency modes.

2.2 Geometry & Computational Grid

Two blade geometries are utilized here. The first part of the study deals with comparisons between a single rotor and two rotors in hovering condition. As such we utilize the same geometry as used in earlier studies [12]. For completeness, this is the two bladed 9450 propellers of the commercial UAV DJI Phantom III [82] (see Figure 2-2). It has a diameter of 0.239m, and a C_{tip} of $0.01m$. A computer-aided design (CAD) model was created based on the chord and twist distributions provided by Diaz and Yoon [25] shown in Figure 2-1.

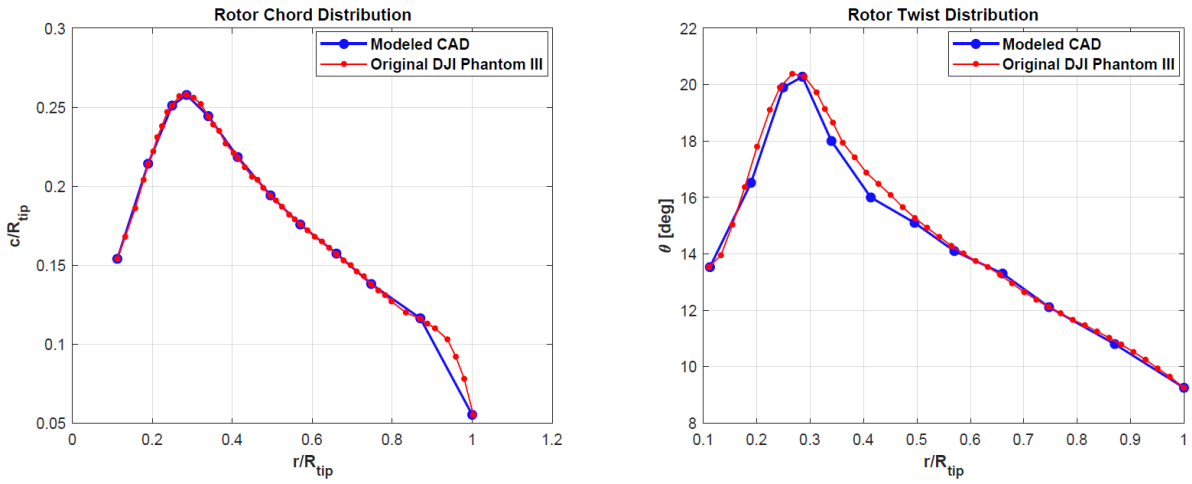

(a) (b)

Figure 2-1 (a) Rotor chord distribution, (b) Rotor twist distribution of DJI Phantom III [25] blade and the Modeled CAD blade.

For all subsequent multirotor computations, we employ a counter-rotating configuration. This is to emulate the general operating conditions of typical quadrotor type vehicles, which have two clockwise and two counterclockwise rotors for stability. A tip clearance of ~0.0478m (0.2D) is used.

Figure 2-2 Geometry of Counter-Rotating Propellers

A second set of propeller geometries are utilized for our comparison between inflight conditions. Two rotors in hover and forward flight will be computed with the T-Motor P15x5 rotors of the SUI Endurance Vehicle. This is mainly to necessitate close comparison with experimental data by Zawodny et al [20]. It has a diameter of 0.38m, and a C_{tip} of approximately 0.014m, with an extra taper at the tips and a tip clearance of ~0.129m (0.34D). A CAD model of this blade was obtained online at the GrabCAD library [83]. An assumption of symmetry is made,

taking one fore (R1) and one aft (R3) rotor of the UAV (see Figure 2-4) into consideration due to computational limitations.

Figure 2-3 Geometry of the T-Motor P15x5 propeller [83]

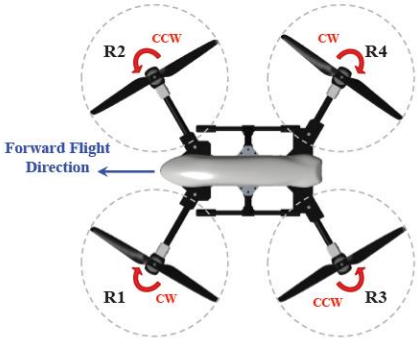

Figure 2-4 SUI Endurance UAV used by Zawodny et. al [20]

2.2.1 Grid Generation

Grid generation is performed using OpenFOAM's native grid generation tool, SnappyHexMesh. Three grids are generated – one for two in-line DJI Phantom III blades, one for two in-line T-motor rotors in hover, and another for T-motor P15x5 rotors in forward flight. For all subsequent grids, as explained by Mankbadi et. al [84,85] , it is suggested that for a good performance of the HLES approach, a wall y^+ range of $30 < y^+ < 300$ should be maintained. As such we enforce the lower limit of this range, that is $y^+ = 30$ near the walls, as they are modeled using URANS. The general choice of mesh resolution is obtained based on the resolvable near-field acoustic frequency. A resolution of 25 to 30 points per wavelength is utilized in the grid generation in the regions of interest, that is the near field. Typically, the consensus in the research community is to use at least 6-8 points per wavelength for acoustic wave capturing for higher order

schemes. It is however suggested to double that for lower order finite volume schemes such as those implemented in OpenFOAM.

The following are the general grid parameters:

- Domain assumes spherical shape to aid dissipation of acoustic waves at the boundary for the hover cases, and a spherical with flat fore and aft sides for inflow and outflow boundaries for the forward case. Domains for T-motor rotors span 8.4m in diameter = ~22 rotor diameters (Figure 2-6), and that for the DJI blades span 8m = ~33 rotor diameters (Figure 2-5).
- Hexahedral dominant unstructured cell type utilized with y^+ of 30 enforced in the boundary layer, sufficient for Detached Eddy Simulations.
- Near-field resolution is ~0.002m (14 % $C_{tip,Tmotor}$) and spans 1.6m diameter = 4.2 rotor diameters for the T-motor rotors, and ~1m in diameter = ~8.8 diameters for the DJI blade case.
- The region very near the blades as well as in the region between the rotors (for the counter-rotating case, is resolved to ~0.001m (7% $C_{tip,Tmotor}$)
- The refinement region of the forward flight case is slightly lobed to the right to capture the wake generated in the translation motion (.
- Total cell count: 35 million cells each.

Identical near-field and propeller surface grids are generated for both cases.

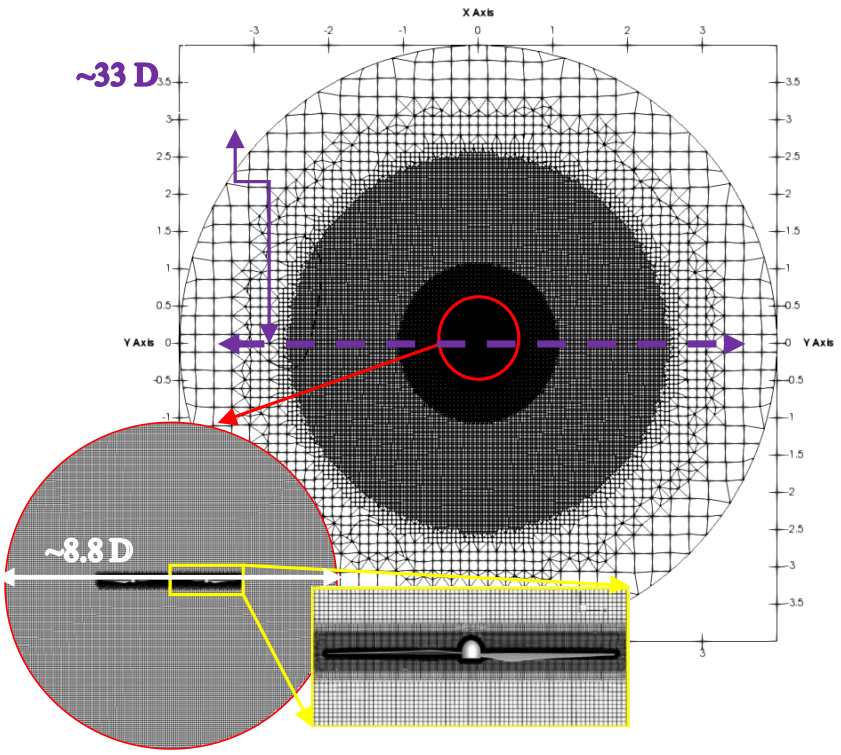

Figure 2-5 Vertical Slice Through Grid Showing Refinement Regions (DJI Blade)

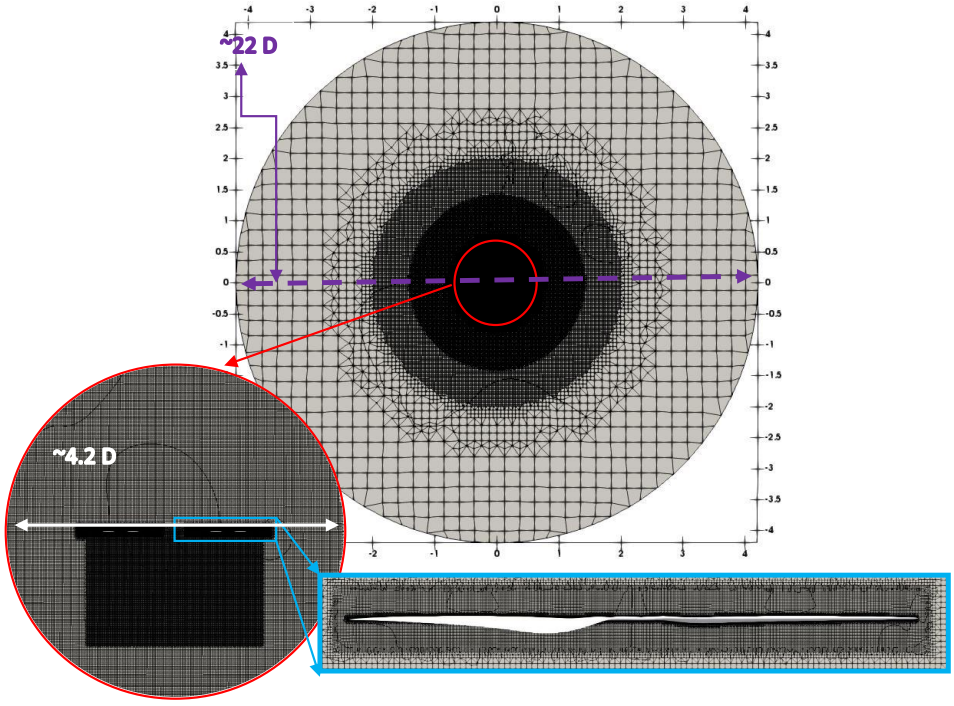

Figure 2-6 Vertical Slice Through Hover Case Grid Showing Refinement Regions (T-motor Blade)

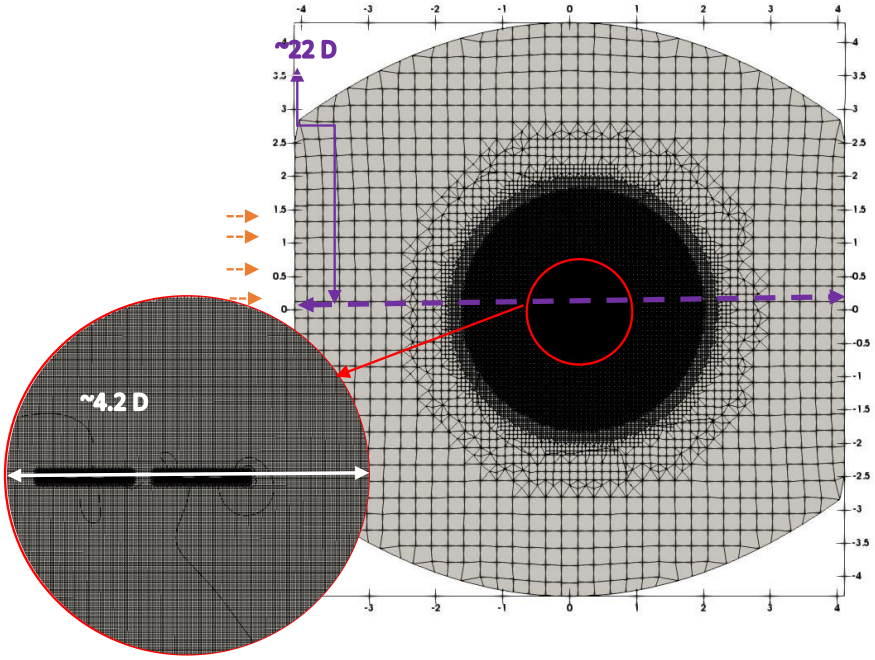

Figure 2-7 Vertical Slice Through Forward Flight Case Grid Showing Refinement Regions (T-motor Blade)

2.2.2 Grid Independence Study

To validate the mesh resolution needed for the computation, a grid independence study was performed on the blades. The T-motor P15x5 blade geometry was selected for this study. The thrust at a rotational rate of 4500 RPM was used. Results were compared with experimental data by Russel & Sekula [86], for which the thrust at the specified rotational rate was 10.6 Newtons. To validate the dependence of the flow features on the grid, we extract the pressure time derivative across the wake at 0.4D below the rotor plane. All computations are run for exactly 12 rotor rotations. Table 1 shows the results of the grid independence study (thrust), and Figure 2-8 shows the results of the variation of pressure across the wake.

Table 2-1 Grid independence study for the T-Motor P15x5 blade

	COARSE	MEDIUM	FINE	FINEST
nPoints (Blade)	5,566	71,821	311,858	621,256
nCells (Domain)	7,397,989	15,130,747	35,219,877	60,521,071
Cell size (Wake & acoustic near field) (m)	0.03	0.015	0.01	0.0075
Peak $\partial p/\partial t$ (Pa/s)	1705.45	2894.34	3272.6	3419.39
Thrust (N)	9.6034	10.1736	10.5201	10.5428
% Thrust Deviation	5.937%	3.406%	0.2158%	0.00542%
%Thrust Deviation from Exp [86]	9.402%	4.0226%	0.753%	0.5396%

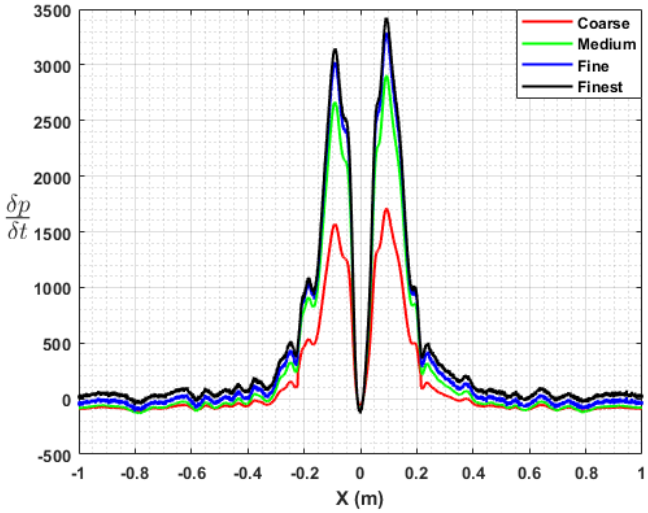

Figure 2-8 Grid sensitivity study showing variation of pressure time derivative at 0.4D below rotor.

The difference between the Finest and the Fine case is quite negligible given the difference in the total cell count for the thrust. For the pressure derivative, we see a 4.485% change between the finest case and the fine case. This difference is deemed small enough given the cell count. As such, we utilized the "Fine" surface grid for our subsequent computations. The cell size for the wake (0.01m) is utilized for all regions in the acoustic near field.

2.3 Results – Hovering

High-fidelity computations of two in-line rotors of two- bladed– DJI in hovering are presented here. These results will be compared with that of an isolated propeller with the same blade geometry used in our earlier studies [12], and with experimental data by Intaratep et al. [21]. The simulations were typically run on 360 CPU cores in parallel on ERAU's Vega cluster. A rotor speed of 5400 rpm is utilized for the DJI blade. The results presented here are divided into three sub-sections: the flow-field, the directly resolved near-field acoustics, and the far-field noise predictions.

2.3.1 Flow Field

Instantaneous quantities of velocity and vorticity are taken after 20 rotor rotations at which a statistically steady solution has been attained. We look at the instantaneous snapshot of the velocity magnitude in Figure 2-9. We compare the wake structure with that of the single propeller case. We notice more turbulent mixing with the two-propeller case as opposed to the relatively undisturbed wake structure of the single propeller case [12]. A look at the instantaneous snapshot of the scaled Turbulent Kinetic Energy (TKE), which is computed as $[0.5 * (\bar{u}^2 + \bar{v}^2 + \bar{w}^2)]/u_{tip}^2$ in Figure 2-10 shows the induced flow behind the rotors bending slightly toward the opposite rotor. This can be attributed to the Coanda effects of the radial flow. Looking at the horizontal slice through the near wake region, we see regions of elevated TKE due to the periodic tip vortex shedding. We see a slight bulge or onset of separation towards the region between the rotors. This is postulated to be a result of a steady upwash interacting with the radial flow of the rotors, which results in separated region towards the inward blade tips. This separation region effects are also seen by Zhou et. al [87] and increases drastically with decreasing separation distance and may be responsible for the

thrust variation observed by Zhou et. al. [87]. It should be noted that the asymmetry seen in the horizontal slice is a result of the rotor rotation directions (counter-rotating) with the left rotor moving counter-clockwise and the right rotor moving clockwise. These entrails more flow forward of the rotors, which is seen as the significant TKE content fore of the rotors in the central region.

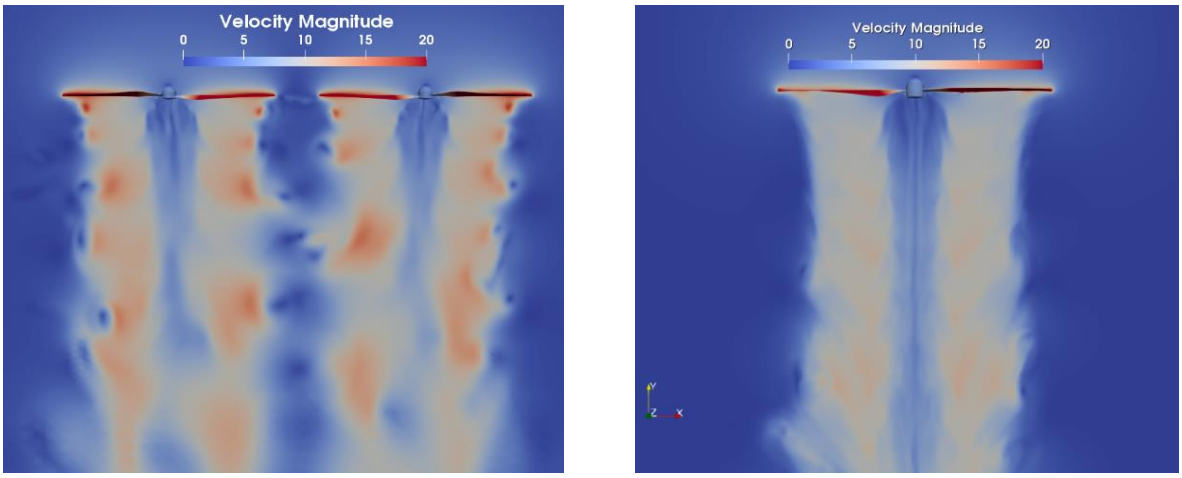

(a) (b)

Figure 2-9 Snapshot of Instantaneous Velocity Magnitude contours (a): HLES, two Propellers, and (b): HLES, Single Propeller [12]

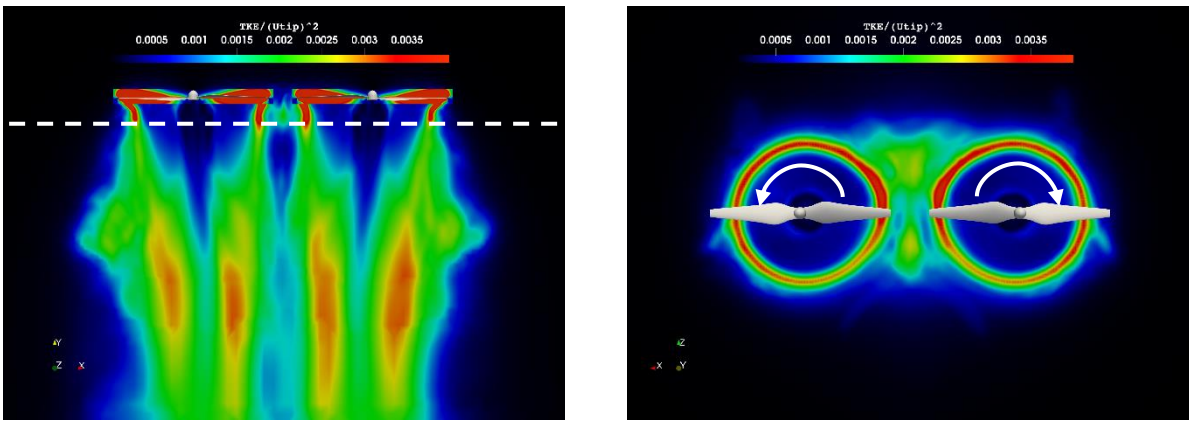

(a) (b)

Figure 2-10 Snapshot of Turbulent Kinetic Energy Scaled by tip velocity (a): Vertical Slice, and (b): Horizontal Cut through wake at 0.6 R below rotor plane.

To further explore the effects of the tip-blade interactions, we plot out the time history of the thrust coefficient for the two rotors (Figure 2-11).

$$C_T = \frac{T}{\rho_\infty \pi R^2 (\Omega R)^2} \tag{2.29}$$

Comparing the normalized thrust time variation of the two-propellers system with the isolated one (Figure 2-11), we clearly see a periodic increase/decrease of the thrust as the blade of one propeller approaches a blade of another propeller. This was corroborated by Lee & Lee [24] and may explain the observed increase in tonal noise that will be discussed in the subsequent sections.

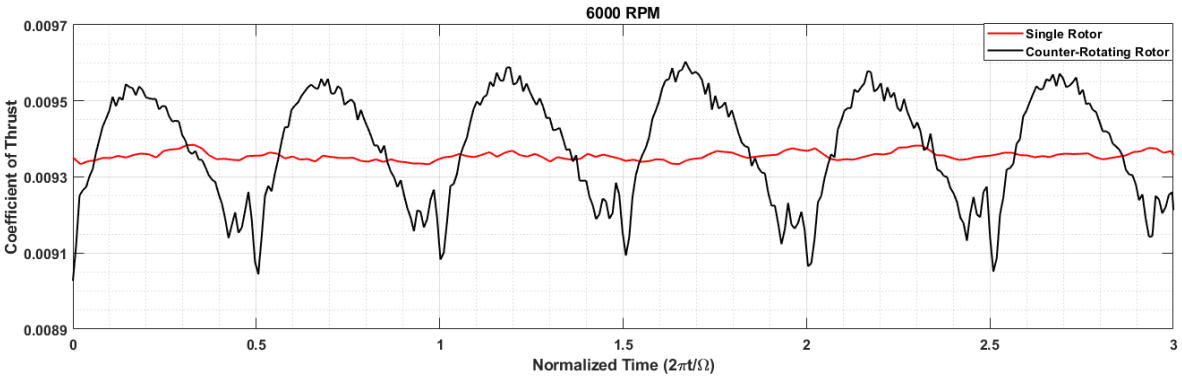

Figure 2-11 Thrust Per Rotor time history.

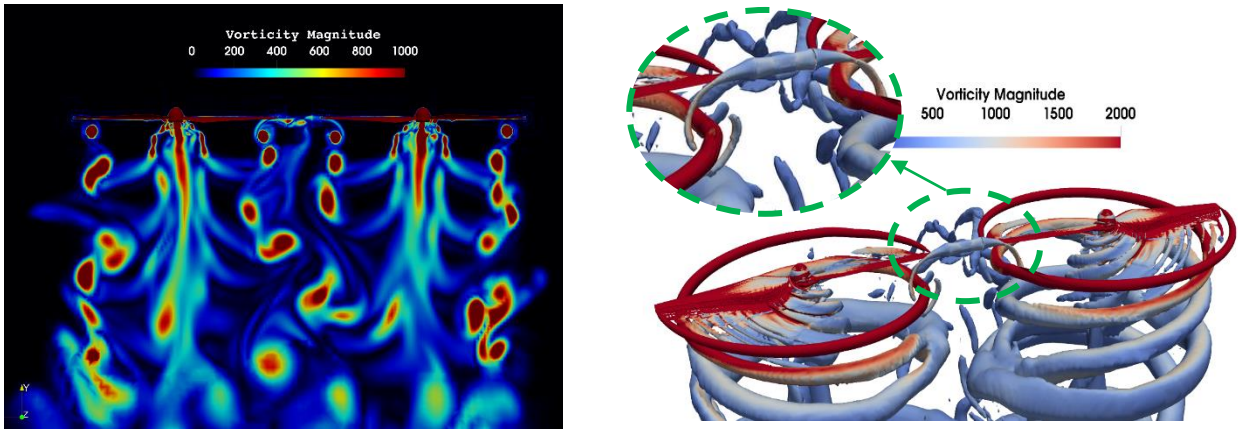

(a) (b)

Figure 2-12 Snapshots of (a): Vorticity Magnitude contours, and (b): Q-Criterion Iso contours colored by Vorticity Magnitude.

Instantaneous slices of vorticity magnitude and Q-criterion iso contours in Figure 2-12. From these figures, we can draw some preliminary conclusions on the dynamics of the wake interactions

between the rotors. From Figure 2-12a, we notice some rotor wake mixing in the separation region between the rotors. It was conjectured that some significant contributions of the broadband spectra of propellers in the low-mid frequency range were due to the wake dynamics [12]. A close up of the region between the rotors shows a tip – tip vortex interaction and a transfer of vorticity, which is visible in the vorticity magnitude snapshot (Figure 2-12a), and is further explored in the Q-criterion plot shown in Figure 2-12b. Similar results were shown by Yoon et al [88]. This could explain some of the unsteady loads responsible for the thrust variation. This contributes to the constructive tones that increase the overall noise signatures, which would reduce with increasing separation distance as concluded by Zhou et al [87]. This is further discussed in the subsequent section.

2.3.2 Near-Field Acoustics

We now examine the directly computed acoustic field to quantify the noise generation mechanism of multirotor systems. We note that with our conservative assumption that 25 grid points are needed to capture the acoustic waves, we can accurately capture frequencies up to about 1500 Hz, or for a rotational rate of 5400 RPM, is equivalent to up to 8.3 blade passage frequencies. This covers the low-to-mid frequency range of the tonal and broadband noise content in the spectrum. In all acoustic contours, we plot out dilatation rate which is computed as:

$$\frac{1}{p}\frac{Dp}{Dt} = \frac{1}{p}\left(\frac{\partial p}{\partial t} + \nabla \cdot \vec{\mathrm{V}}\right) \tag{2.30}$$

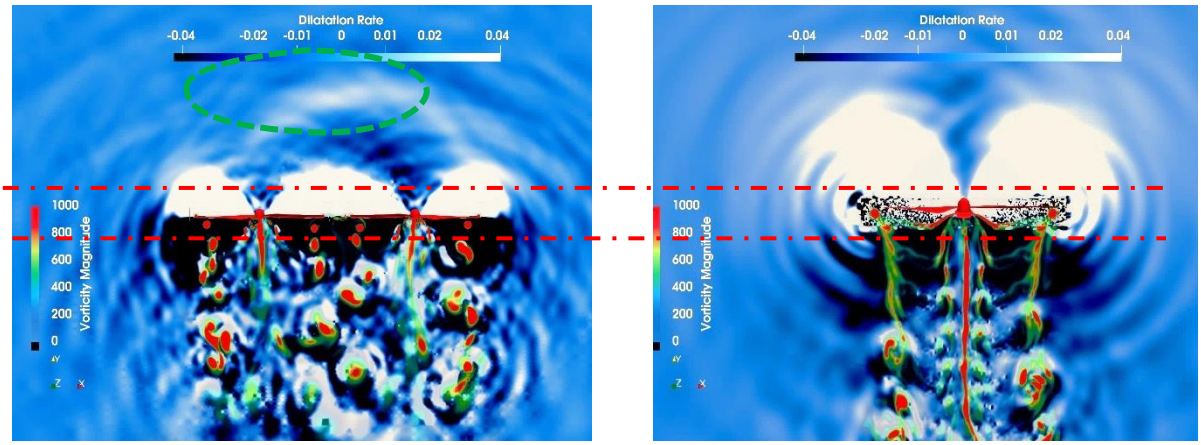

(a) (b)

Figure 2-13 Vertical slice showing snapshot of Vorticity Magnitude overlaid on Dilatation Rate.

(a): Two Counter-rotating Propellers, and (b): Single Propeller [12]

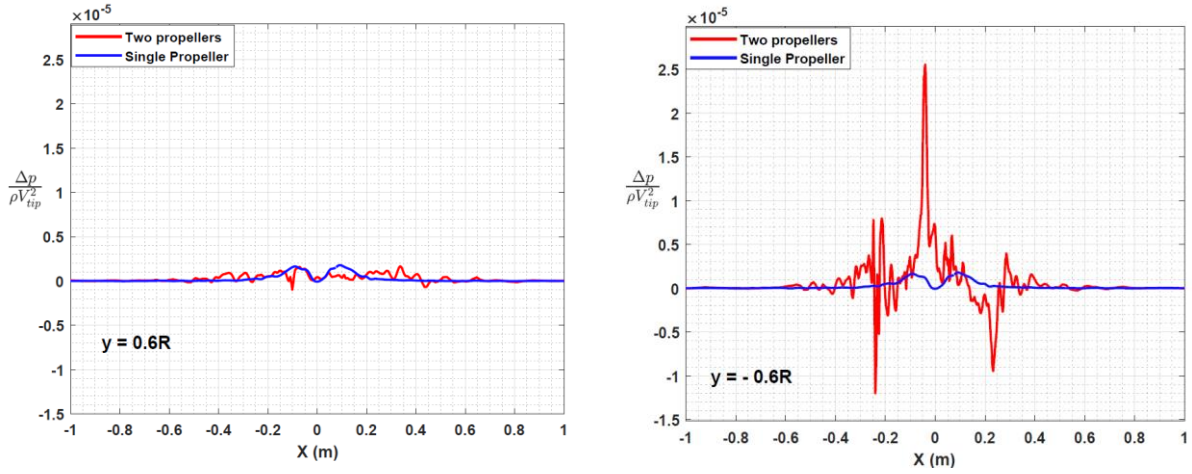

(a) (b)

Figure 2-14 Plot of Non-dimensional pressure fluctuations at (a): 0.6 R above rotor plane, and (b): 0.6 R below rotor plane

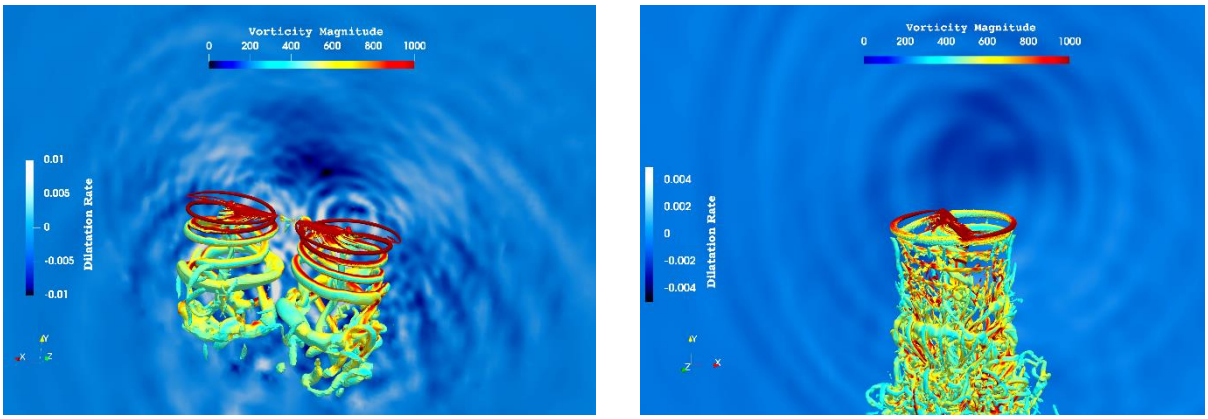

(a) (b)

Figure 2-15 Snapshot of Q-Criterion Iso Contours with Dilatation Rate background.

Snapshots of the dilatation rates are shown in Figure 2-13, and compared with that of the single propeller case [12]. Consistently with the case of the single propeller shown by Mankbadi et. al [12], we see the strongest waves radiating from the propeller surface due to blade loading. To distinguish between hydrodynamic noise and acoustic noise, the vorticity magnitude is overlaid on the dilatation rate. This shows the effect of convection of the wake below the propellers. One clear phenomenon seen in the figure is the interference banding of acoustic pressure in the region above the space between the rotors highlighted in green in Figure 2-13a. This can be explained by the constructive interference between the two rotors. Zhou & Fattah [17] found that there was significant increase in overall noise for the counter-rotating propellers as opposed to corotating propellers. This would explain their assertion and finding. A further probe into the interaction noise is performed by extracting the non-dimensional acoustic pressure at 0.6R (indicated with red lines in Figure 2-13) above and below the rotors. We clearly see that there significantly more fluctuations in the counter-rotating case compared to that of the single propeller shown in Figure 2-14 & Figure 2-15. Lee & Lee [24] found that while the thrust coefficients were independent of the separation distance, the fluctuations in thrust were found to increase dramatically as the

separation distance decreased. We can relate the non-dimensional pressure perturbations above the rotors to their effects on the thrust loading on the blade surface, and we see significantly more fluctuations for the counter-rotating propeller case. This may be due to the proximity of the blades and the acoustic pressures they radiate interacting and affecting the pressure distribution in the near-blade region. The effects of the vortex-vortex mixing of the wake are seen in the sharp spike in the non-dimensional pressure perturbations in Figure 2-14b. Further investigating the near field acoustic interactions, we take horizontal slices 1.5R below the rotor (Figure 2-16). Again, we see the wake interaction effect being translated into acoustic interference downstream of the propellers. These fluctuations are possibly the source of the increase in the broadband content of the noise signatures as they are inherently like shearing effects of jets [89,90].

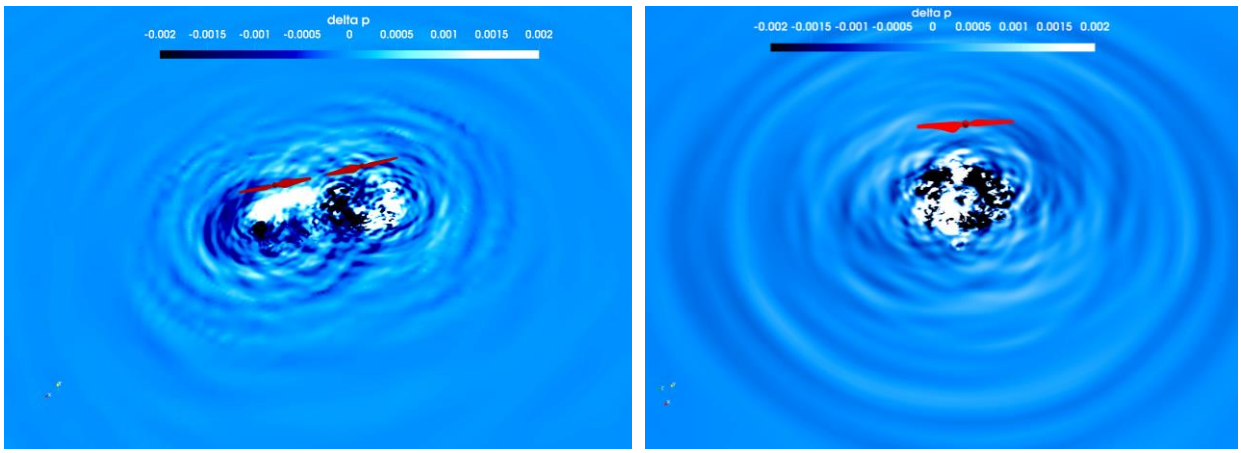

(a) **(b)**

Figure 2-16 Horizontal Slice Through ($\Delta p'$) at 1.5R Below the Propeller Plane. (a): Counter-rotating Case, and (b): Single Propeller [13]

Tonal Noise Sources

Looking at the near-field contours in Figure 2-13a, we notice some of the tones interact and increase at some regions and decreases at other regions. Due to the interaction of the tones from each blade, some secondary tones may arise. Our configuration has no phase difference between

the rotors. However, implementing phase shifts between the rotors has been studied to reduce some tonal levels [49]. Additionally, analyzing the thrust coefficient time history plot in Figure 2-11, a simple calculation of the period, T gives 0.0056s, which corresponds to a frequency of 180 Hz equal to the blade passage frequency. This means the periodicity observed would increase the fundamental tone, due to the proximity of a rotor at the same rotational rate and phase, and the aperiodic fluctuations may also increase the subsequent harmonics. A look at the surface pressure fluctuations (Figure 2-17) reveals an increase in pressure near the blade tips on the pressure side when the rotors pass each other. This could explain the dip in the performance of the blades as seen in the thrust plots, as well as an increase in the fundamental tone.

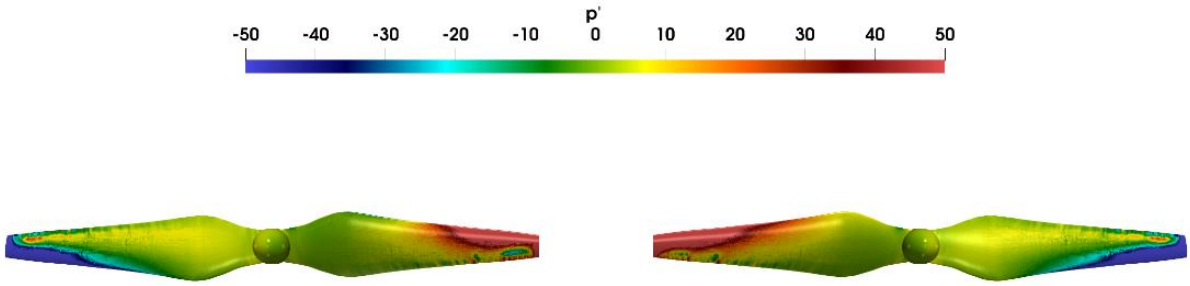

Figure 2-17 Surface Pressure fluctuation (*p'*) for counter-rotating rotors

To further explore the noise sources, we employ the technique of Spectral Proper Orthogonal decomposition (SPOD) [32]. A brief description of the implementation of the SPOD is provided here. The workflow for the algorithm is as follows:

1. The snapshots of the parameter of interest are restructured as a time series in a matrix form, that is [time, x, y, parameter (e.g., Pressure)].
2. Next, the time average of the parameter is computed, and then subtracted from the instantaneous values of the parameter such that the final array used in the processing, for example, pressure, is $\hat{Q} = p - p_{mean}$.

3. $\hat{Q}$ is then split into FFT blocks and a discrete fourier transform is performed on each block. We can call this new spectral data $\hat{Q}_{fft}$

4. For each frequency of interest, a matrix, M is formed such that:

$$\mathrm{M} = \hat{Q}_{fft}^{T} * \hat{Q}_{fft} * W \tag{2.31}$$

W is the weighting function for the FFT, for example, the hanning windowing weights.

5. Next, the eigen values and vectors of the new matrix, M are found such that $[\Theta, \lambda]$ = eig(M)

6. From this, the reconstructed spectral data are computed as:

$$\psi = \hat{Q}_{fft} * \Theta * \left({}^{1}/_{\sqrt{\lambda}}\right) \tag{2.32}$$

We take snapshots of pressure contours and analyze the modes that constitute the frequencies of interest. Looking at the relative contributions of each of the modes (Figure 2-18), it can be seen that the first mode accounts for over 97% of the mode energies. This also depicts that the dominant tones are generated by the leading modes of the system, whereas some contributions of the broadband may stem from the subsequent modes.

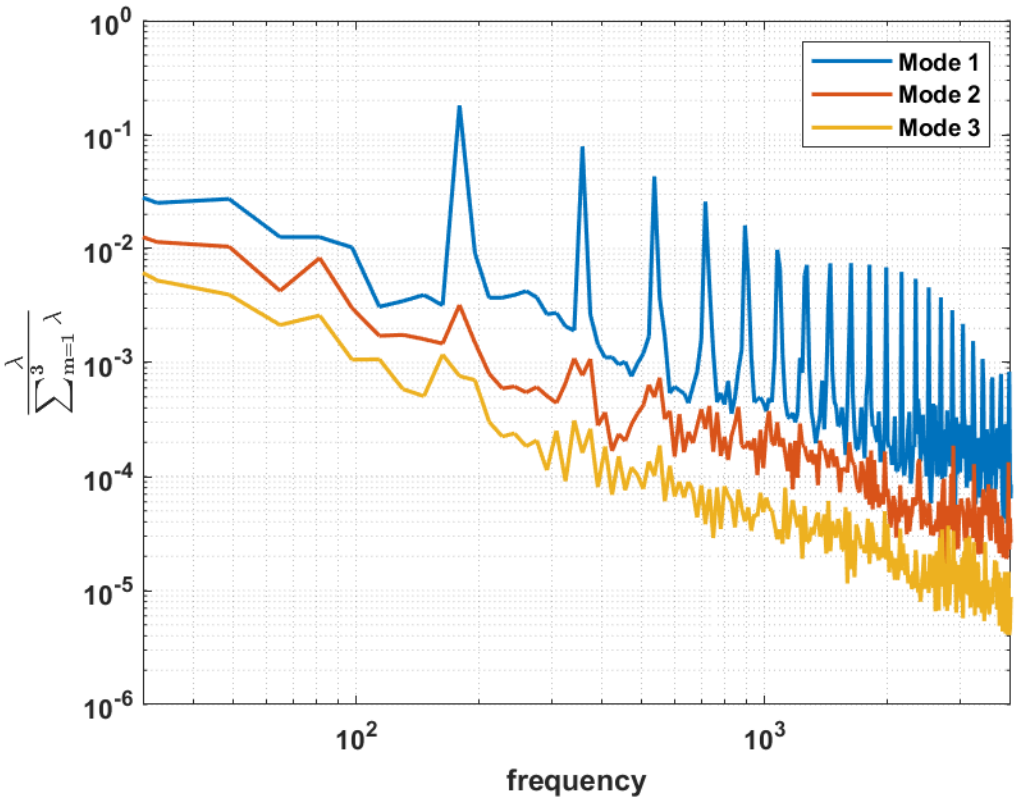

Figure 2-18 Spectra showing ratio of mode energies for the first 3 modes.

We focus here on the low-mid frequency range of the spectra shown in Figure 2-18. Because this is a spectral decomposition of the pressure field, the mean values are extracted leaving the perturbation pressure. We note here that the most energetic (first mode) was seen to account for ~97.86 % of the acoustic energies at the respective frequencies for the tonal frequencies. However, for the broadband frequencies, the first modes were not sufficient to describe the physics of the flow, and thus the sum of the first two modes are presented, which have a total energy content above 80% for the respective frequencies. We need to point out that in the linear acoustic radiation regime, the energetic modes are directly responsible for the corresponding radiation. In the nonlinear regime, due to possible nonlinear changes, there may not be a one-to-one correspondence between the source at a given frequency and the radiation sound. The SPOD plots shown in Figure

2-19 & Figure 2-21 are focused on the linear acoustic regime. Note that the Energy content represents the percentage of the eigenvalue of the mode(s) in question and provided information on the average energy captured compared to the total energy at the specified frequency. We plot out the first and most energetic mode of the tonal fundamental frequency of ~180Hz for a 5400 RPM, as well as the second and third harmonics in Figure 2-19. We notice that the periodic tones are seen to radiate from the blades, with some slight contributions from the wake near the blades. At higher BPF frequencies, we see most of the tonal content radiating from the blades with no contributions from the wake. A deeper look at the first 2 modes is shown in Figure 2-20. Here, we note that at lower frequencies, the second mode accounts for some of the contributions stemming from the shear layer of the wake structure. At higher frequencies, again, this contribution diminishes.

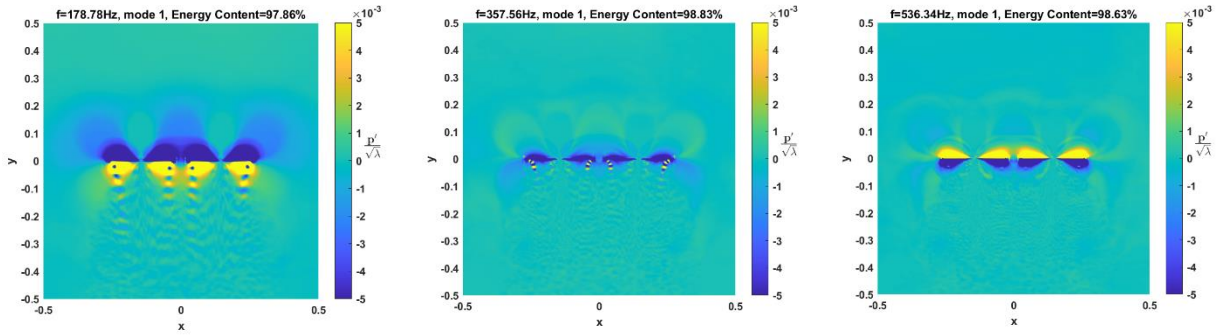

Figure 2-19 Spectral contour plots at tonal frequencies

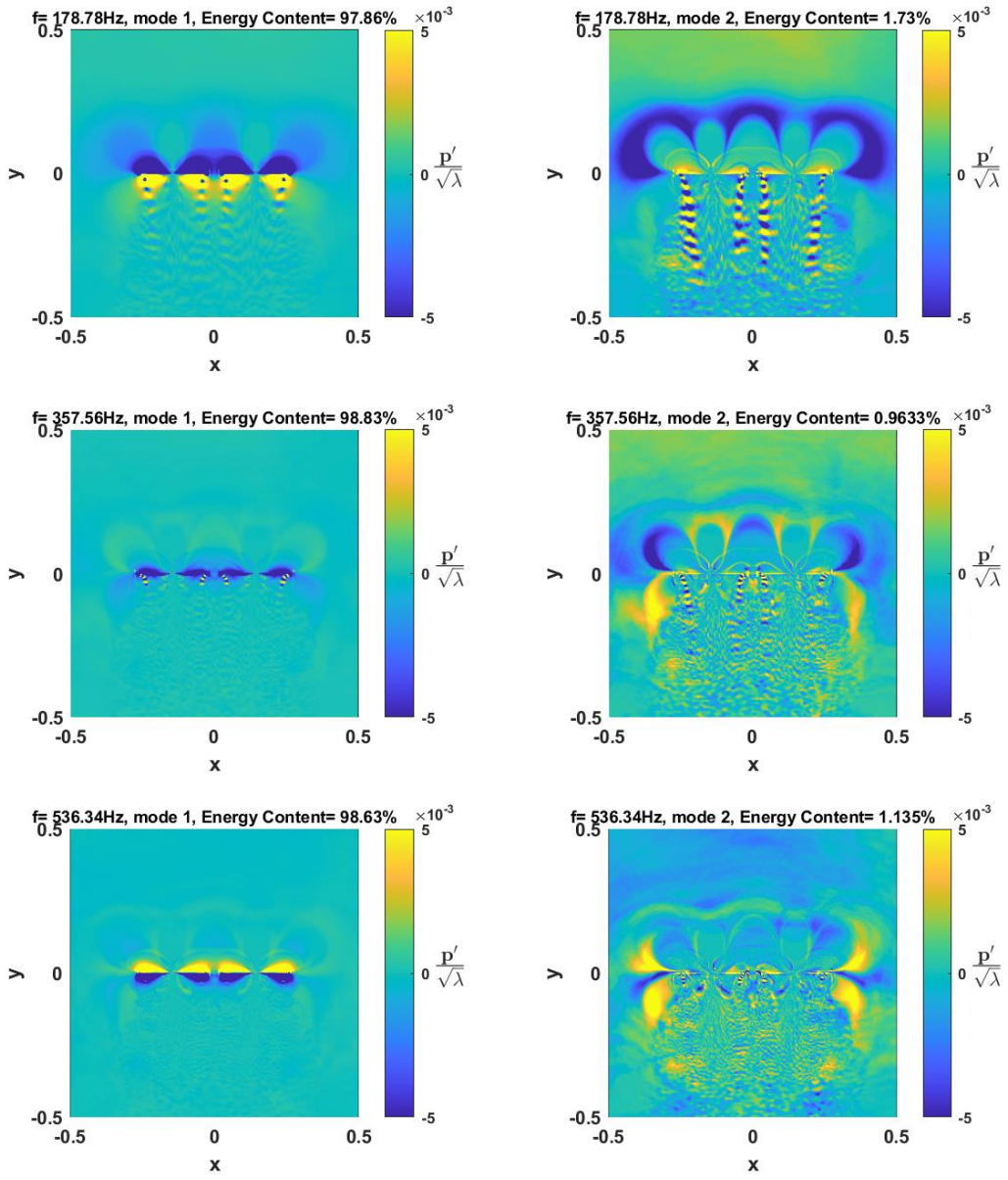

Figure 2-20 Spectral tonal contents for the first two modes.

Broadband Noise Sources

Next, we attempt to identify the broadband noise sources. Looking at the spectral plots in Figure 2-21, we plot out the frequencies corresponding to the low to mid frequency broadband noise from Figure 2-18. The lower frequencies have significant contributions from the wake. This corroborates findings by Mankbadi et al [12]. With increasing frequencies, however, the

contribution of the wake as a broadband source diminishes, and we notice some contributions in the near blade region. Again, looking at the bigger picture of the two leading modes in Figure 2-22, we see that unlike that of the tonal frequencies, the second mode contributes a significant percentage to the overall energy content. This can be explained by the fact that broadband noise is inherently a nonlinear process and requires more data to describe the physics at play.

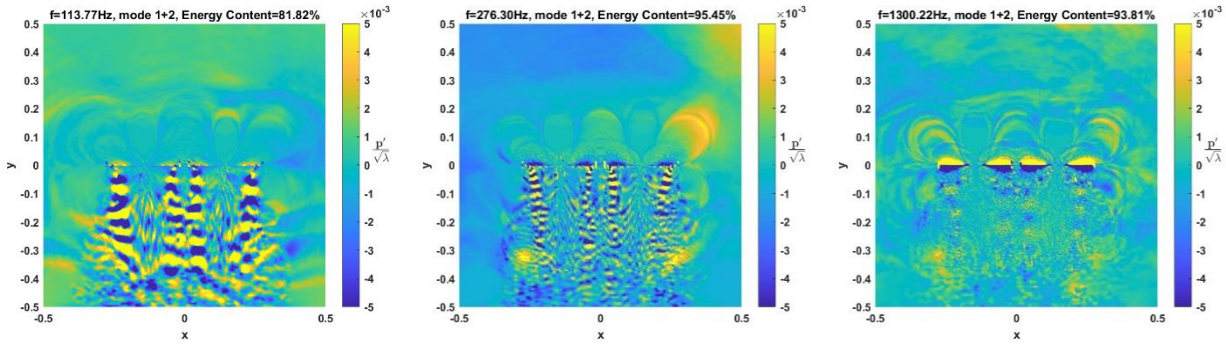

Figure 2-21 Spectral contour plots at broadband frequencies

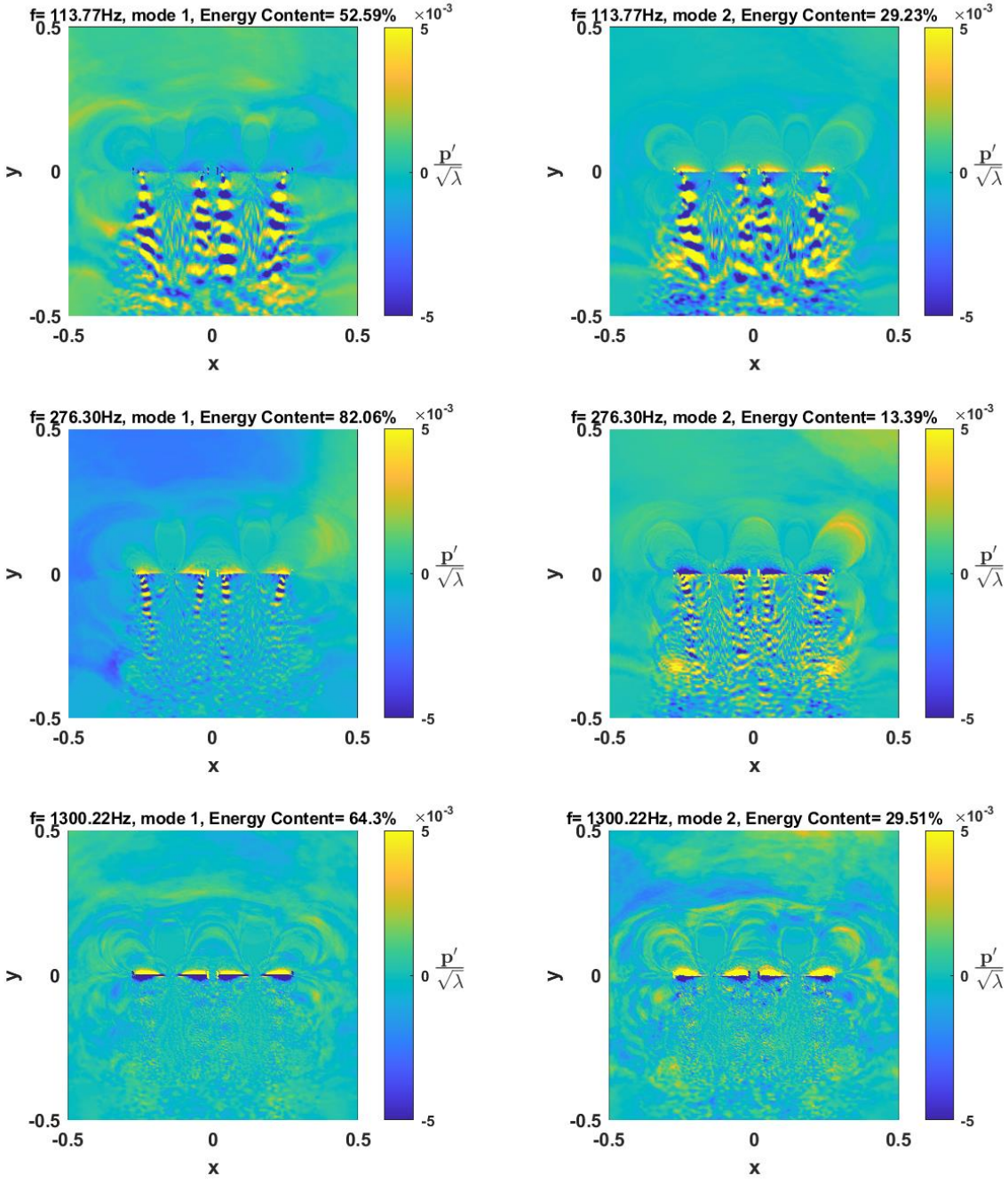

Figure 2-22 Spectral broadband contents for the first two modes.

2.3.3 Far-Field Acoustics

The Ffowcs-William Hawking's formulation is used here to extend the near field to obtain the acoustic far field. The formulation can be applied to a permeable surface or a non-permeable

surface. Since we need to capture the sources on and outside of the blade surfaces, the permeable surface is used here, though spurious signals can also arise when vortices pass through the permeable surface [91]. We avoid this by employing a top-capped control surface, with no bottom cap. The formulation applied to a permeable, non-moving surface (Figure 2-23) can be written as:

$$4\pi p'(x,t) = \int_{f=0} \left[\frac{\dot{m}}{R} + \frac{\dot{L_R}}{c\,R} + \frac{L_R}{R^2} \right]_{ret} dS;\; m = \rho u_n \tag{2.33}$$

$$L_R = \left(P_{ij}\hat{n}_j + \rho u_n\, u_i \right).\hat{R} \tag{2.34}$$

Here, *m* is the mass flux normal to the surface. We note that for the side of the cylinder, $u_n = u_r$ and $m = \rho u_r$. The pressure term $P_{ij}\hat{n}_j = \tilde{p}\,\hat{r}$, with $\tilde{p} = (\mathrm{p} - p_0)$.

The FWH cylinder is placed at a radius of 0.35m from the center of the two rotors for the DJI case. This is placed at an apt position to encompass all the sources in question, and sufficiently far from the hydrodynamic sources to avoid edge contamination and is shown in Figure 2-23. The observer is located 0.767m below rotor plane, and 1.295m away from center of the symmetry of the UAV, with an angle of 50 degrees from the center, as used by Intaratep et. al [21]. A sampling rate of $1.52x10^{-5}$seconds, comparable to experimental data by Intaratep et al [21], as well as computational results by Mankbadi et al. [12] is used. Data is collected after 30 rotor rotations. A total of 8192 samples are collected for the current case study. An FFT of the data is performed with 50% hanning windowing.

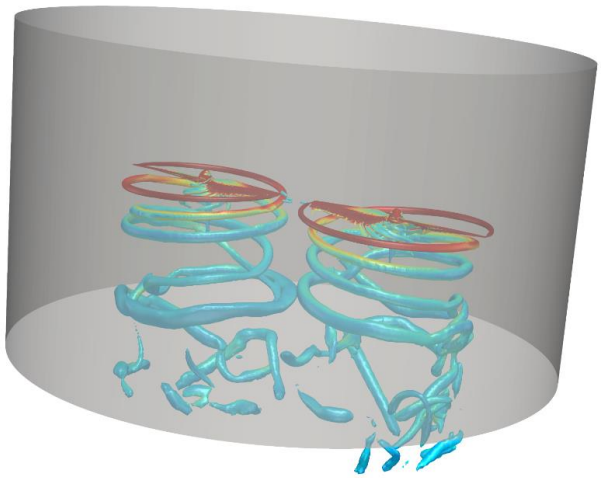

Figure 2-23 FWH Control Surface At ~3R with Q-Criterion Iso-Contours of Vorticity (DJI case)

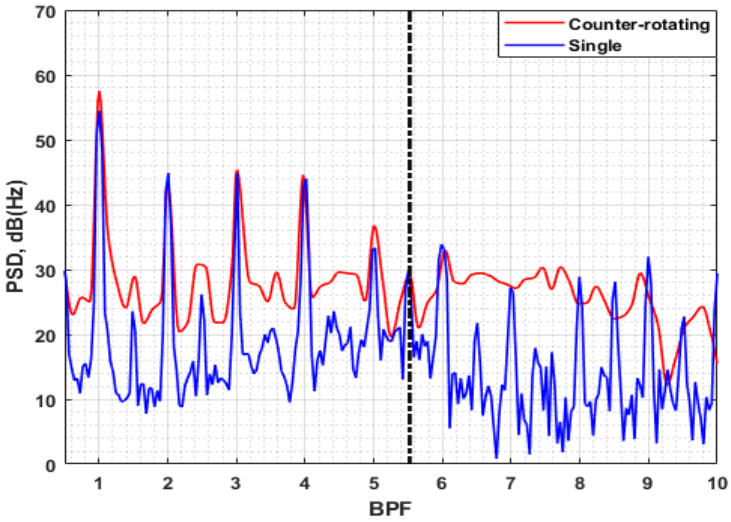

Figure 2-24 BPF Power Spectral Density of Two Counter-rotating Propellers vs Single Propeller [12]

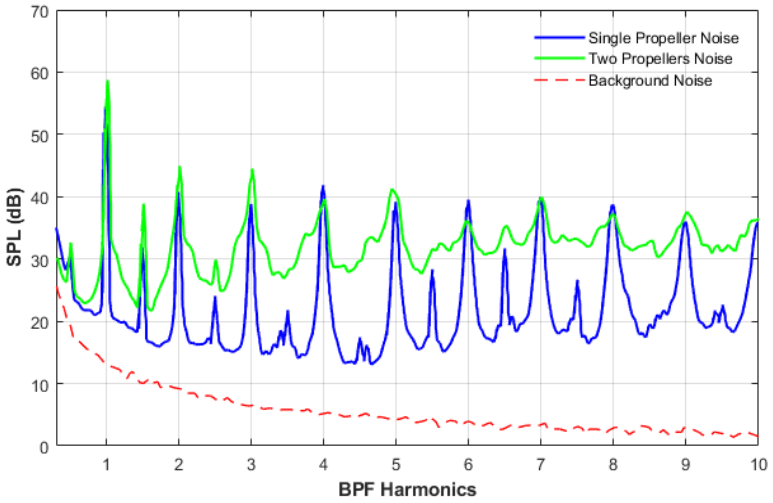

Figure 2-25 Sound Pressure Level Spectral comparison between Single Propeller and Two Propellers [17]

The resulting Power Spectral Density (PSD) of the far-field noise frequency spectrum obtained based on the pressure fluctuation time history on the FW-H surface is shown in Figure 2-24. The frequency is normalized by the blade passage frequency (BPF), which in the case of the counter-rotating propeller running at 5400 rpm, is 180 Hz. This is qualitatively compared with experimental data from Zhou & Fattah [17]. Looking at the spectra in Figure 2-24, we can make some assertions. First, there is a slight increase in the fundamental tone at the first BPF. This is typical for multi-rotor systems. We notice that the subsequent tones are about identical to those of the single propeller case. A drastic change here is seen to be the levels of the overall broadband aspects of the spectra. There is an increase of ~8 dB in the broadband spectra in the low-mid frequency range. It is worth noting that the results shown here have been processed with relatively small sample sizes (1 window of 8192 samples, resulting in frequency resolution of 4Hz). Better broadband trend and resolution can be achieved by increasing the window count. However, the overall trend of the wake structure as well as accuracy is enough for analysis of the spectra. We

also notice that the relative difference between the harmonics and the broadband reduces significantly for the two-rotor case. This is consistent with literature [17,19,21] (Figure 2-25). The reason for this observation in the spectra can be attributed to the increased wake mixing and interaction between the two propellers. We note here that the computed tonal noise at the BPF increase by 3dB due to the rotor-interaction, the experiment of Zhou & Fattah [17] also shows a similar increase of ~3dB due to the interaction of co-rotating propellers. It is worth noting that the results presented are unique to the specific blade orientation, that is the counter-rotating blades are perfectly synchronized, and in-phase, therefore having the blades end up near each other at specific periodic times. The nature of the noise generation may differ with out-of-phase rotors.

To better distinguish between the periodic contents and the broadband content and sources, we utilize a periodic averaging technique [92] on the spectral data. Figure 2-26 shows the tonal and broadband extracted data for both the single and counter-rotating cases. We notice that for the single rotor case, the broadband levels are consistent with the overall trend of the total spectrum. There is some tonal energy retained in the broadband residual spectrum at the harmonics. This could be the result of blade self-noise being excited at the harmonic frequencies, as mentioned by Intaratep et al [21]. Looking at the case of the counter-rotating rotors, we notice less of this interaction, but see an increase in the difference between the tonal content and the broadband in the mid-frequency range. This is indicative of the fact that there is tonal noise increase due to the unsteady loading of the blades near each other.

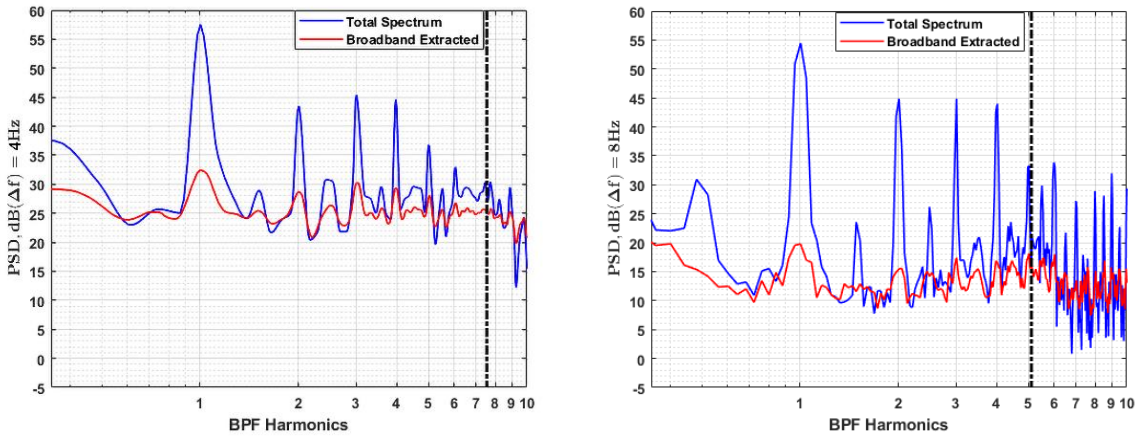

(a) (b)

Figure 2-26 Periodic Averaged Spectra (a): Counter-rotating case, (b): Single propeller case

To further elucidate the wake effects, we show spectral results for the counter-rotating case in Figure 2-27. We assume linear acoustic sources in the far-field and thus add the contributions of the two blades to obtain the spectral results. By comparing the spectral results using the blade surface as the FWH control surface to that of the top-capped cylinder for the isolated single rotor case, we see that there is some reduction in the low-mid frequency broadband levels. This means the wake has some contributions to the broadband noise levels at the lower frequencies as found by the SPOD analysis.

Additionally, we notice that the blade spectra miss the subharmonic frequencies. We postulate that the subharmonic frequencies originate from the wake vortex rollup effects. The wake can be considered as a free jet excited by the rotating propeller at the blade passage frequency, which causes the vortex roll-up at BPF/2, which causes a vortex pairing that generates noise. To verify this, we extract the time history of velocity at the shear layer of the wake, and perform a Fast Fourier Transform to determine the dominant frequency. We find that the dominant frequency is exactly 90 Hz which is exactly half of the blade passage frequency (see Figure 2-28). This explains the source of the sub-harmonics/ shaft frequencies.

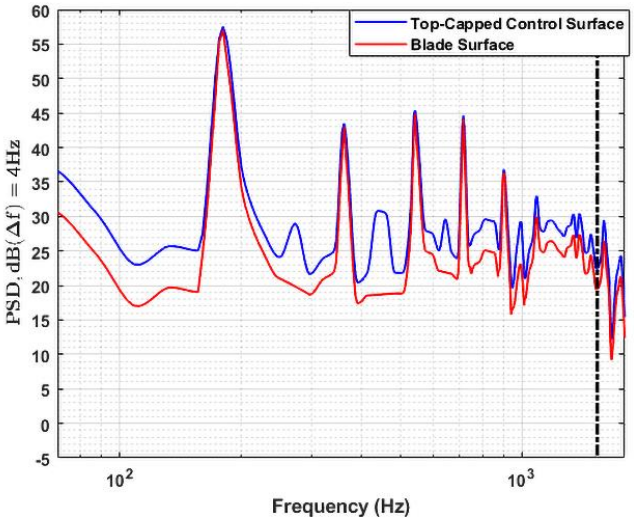

Figure 2-27 Power Spectral Density of top-capped, and Blade surface control surfaces

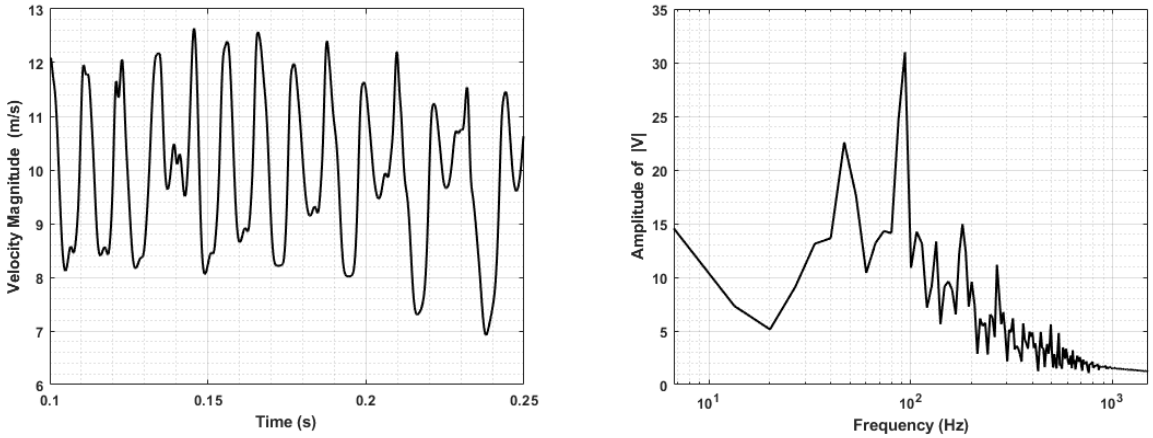

(a) (b)

Figure 2-28 (a). Velocity time History of wake evolution, (b) FFT of velocity in shear layer of wake.

Directivity Study

The directivity of the radiated noise is shown in Figure 2-29. Results are compared with single propeller data from Zawodny et al [11]. Generally, similar trends are noticed in the 1st and 2nd Harmonics as seen in the directivity plots. There is a slight increase in the sound pressure levels in the upper angles can be explained by the strong banding of acoustic waves from the constructive interferences generated from the two blades. This banding is visible in the near-field acoustic

snapshots shown in Figure 2-13. Overall, we notice an increase in the noise below the plane of rotation. This can be attributed to the persistence of the blade loading as well as the wake noise sources radiating in said directions.

Similar trends can be seen in the 2nd Blade passage frequency directivity, with an increase in SPL evident below the rotor plane. A better look at the total directivity around the 2-propeller system is shown in Figure 2-30. Comparing that of the 1st BPF with non-linear vortex lattice method (NVLM) coupled with vortex particle method (VPM) by Lee & Lee [24], we see a significant increase in the overall noise levels. This can be attributed to the unsteady loading introduced by the rotor-rotor interactions. This is corroborated by studies by Lee & Lee [24]. Increase in separation distance has been shown to result in significantly reduced noise levels especially in the upwash region as well as the downwash region of the wake. This again suggests that the greater reason for the increase in the noise levels is because of the rotor-rotor interaction as well as the wake mixing effects.

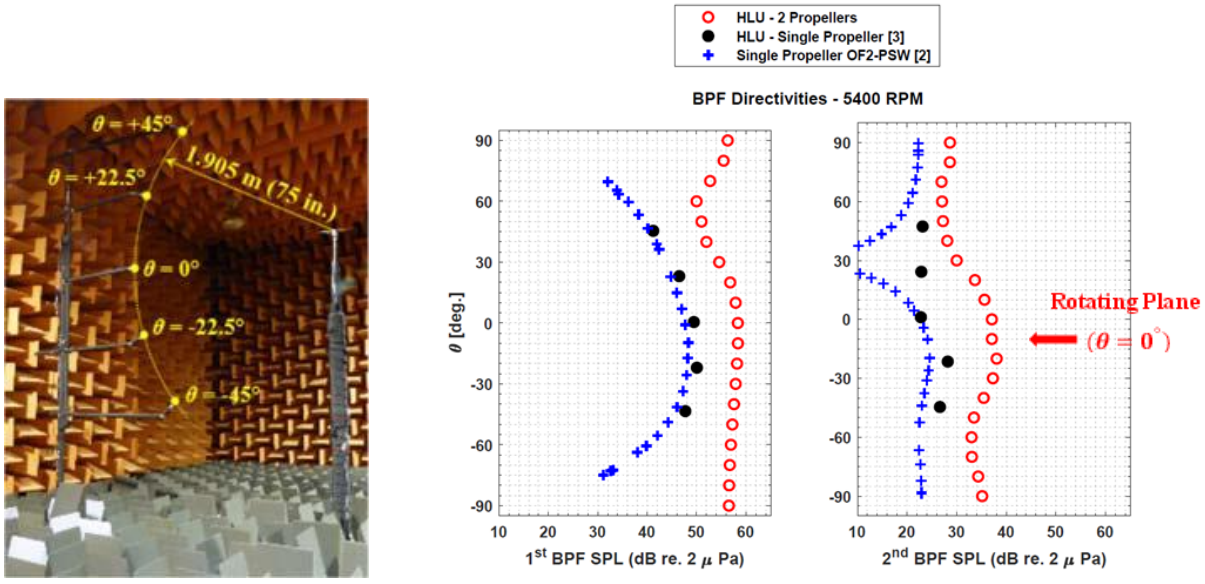

(a) (b)

Figure 2-29 (a): Experimental Setup [2] & (b): Directivity plot at 1st & 2nd Blade Passage Frequencies compared with single Propeller [11,12].

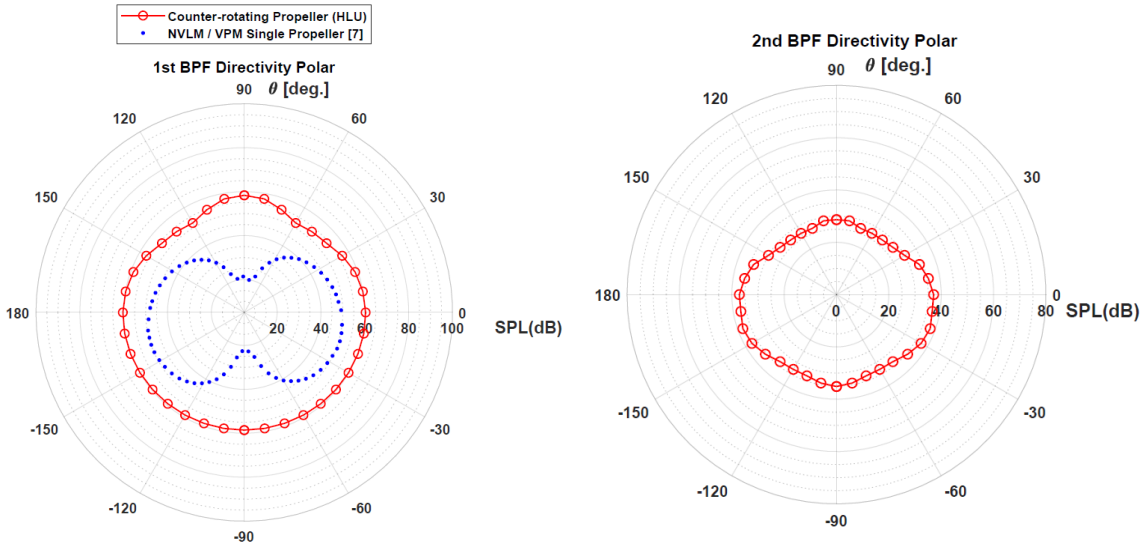

Figure 2-30 Total 1st and 2nd BPF Directivity Plots

2.4 Results – Forward Flight

Next, we look at the variations in the flow & acoustic field between the hover case and the forward flight. For this case, we utilize the T-Motor P15x5 rotors of the SUI Endurance UAV. For comparison with experimental data from Zawodny & Pettingill [20], the two T-motor rotors selected are one fore and one aft rotor of the SUI Endurance UAV. We assume symmetry about the centerline of the UAV as mentioned previously. We select one fore rotor (R1) and one aft rotor (R3) for both hover and forward flight conditions (Figure 2-4). An angle of attack $\alpha_v = 0$ is utilized for hover, and $\alpha_v = -10$ for forward flight. A vehicle speed of 15.34 m/s is utilized for forward flight. Rotor rpms of R1 = 4047 RPM and R3 = 4895 RPM is set for forward flight condition, and 4800 RPM for both rotors for hover condition to attempt to match operating conditions of the experimental data [20]. Again, the results presented hereon are divided into three sub-sections: the flow-field, the resolved near-field acoustics, and the far-field noise predictions.

2.4.1 Flow Field

We show snapshots of instantaneous velocity magnitudes, and vorticity magnitudes, which are taken after 20 rotor rotations at which a statistically steady solution has been attained for static case, and 15 rotations for in-flight case. Due to the relatively wider separation distance as well as the geometric differences, we see little to no tip-tip vortex interactions with this case. However, looking at the time history of the thrust coefficients shown in Figure 2-31, we notice the same periodic dips which is characteristic of a multi-rotor setup. In forward flight, there is a prolonged dip in thrust for the aft rotor. This could be due to the increased rotational rate of the aft rotor. The implications of this could mean that the faster the rotor goes, the more unsteady the thrust loading becomes for forward flight.

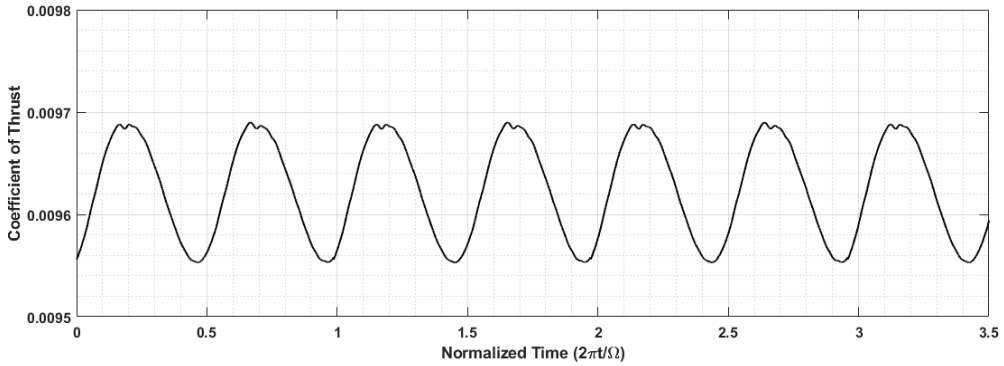

(a)

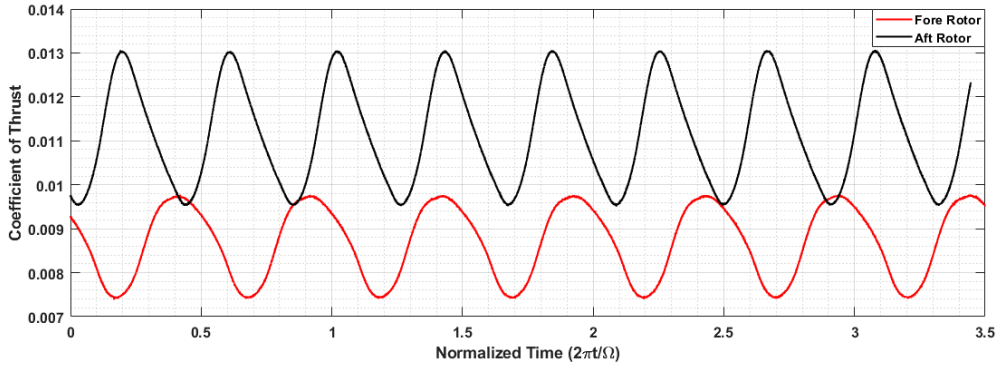

(b)

Figure 2-31 Thrust Per Rotor time history (a): Rotor at Hover, (b): Two Rotors in Forward Flight.

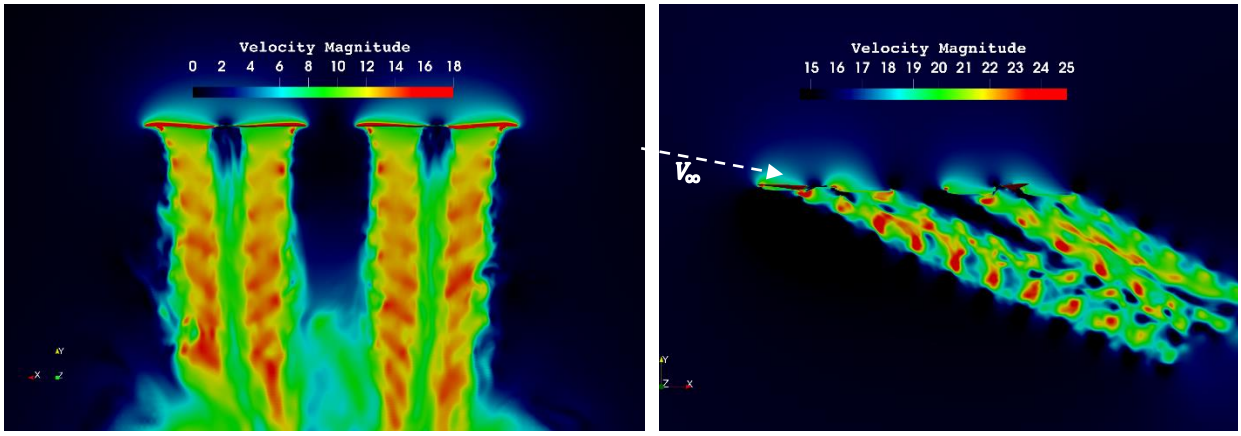

(a) (b)

Figure 2-32 Snapshot of Instantaneous Velocity Magnitude contours (a): Hover, and (b): Forward Flight

Looking at the instantaneous velocity magnitude plots, we notice that there is significant mixing of the wake in the forward flight case as opposed to the relatively undisturbed wake of the hover case. At this flight attitude, we do not see wake ingestion by the aft rotors, but we do still notice some interaction with the aft rotors albeit not as significant. Similar trends can be seen in the plots of instantaneous vorticity:

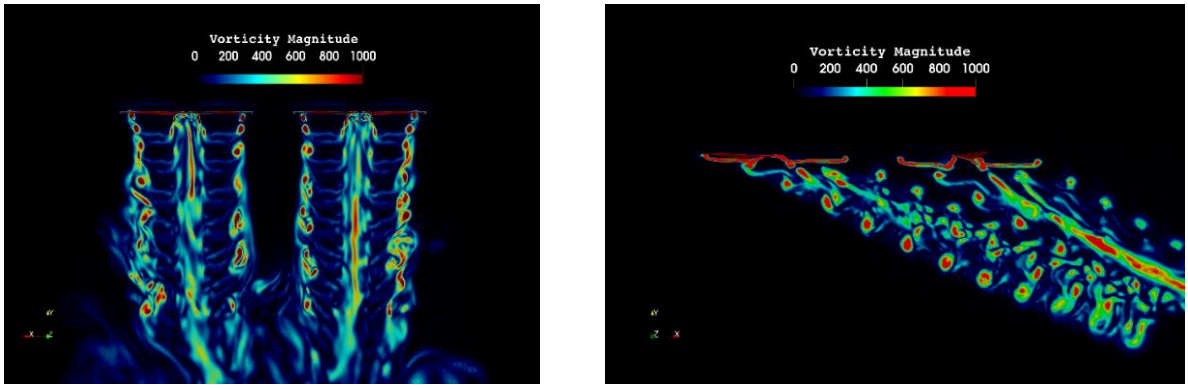

(a) (b)

Figure 2-33 Snapshot of Instantaneous Vorticity Magnitude contours (a): Hover, and (b): Forward Flight

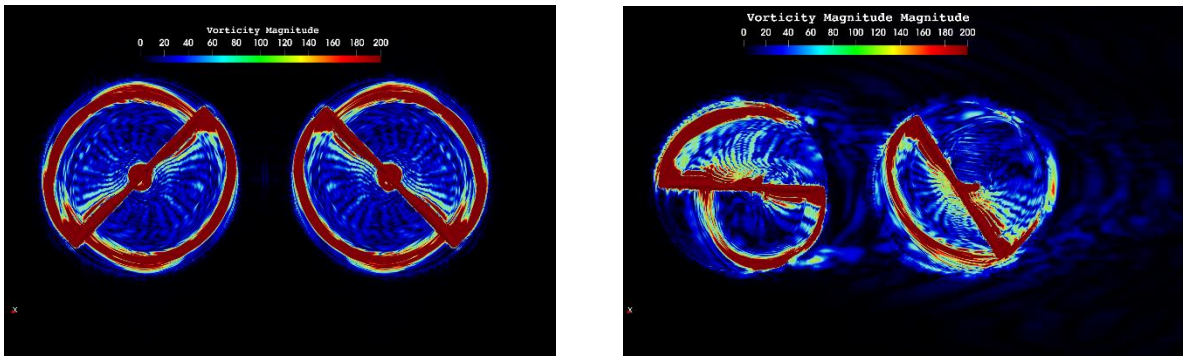

(a) (b)

Figure 2-34 In-plane snapshot of the vorticity magnitude (a): Hover, and (b): Forward Flight.

We see some vortical flow shed from the fore rotors onto the aft rotors in Figure 2-34b. This could possibly introduce some unsteadiness and be a source of broadband noise generation. A further look at the coherent structures in the Q-criterion Iso-contours in Figure 2-35, we notice that, due to the separation distance between the rotors, there is minimal wake interaction in the hover case. In the case of the forward flight, however, some of the vortices shed from the fore rotor interacts with its own wake as seen in the circled parts of Figure 2-35c. These wake vortices also interact with the wake of the aft rotor. This wake-wake, as well as tip vortex-wake mixing may be a source of broadband increase in the noise.

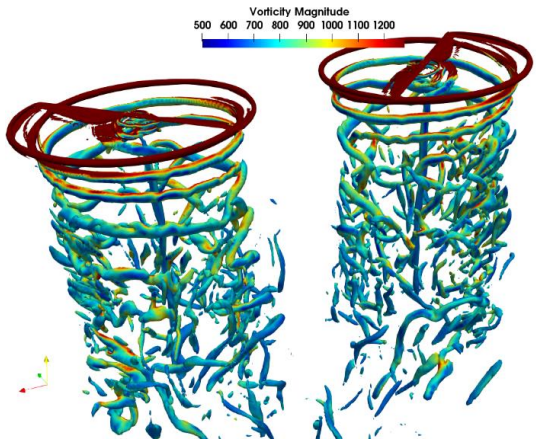

(a)

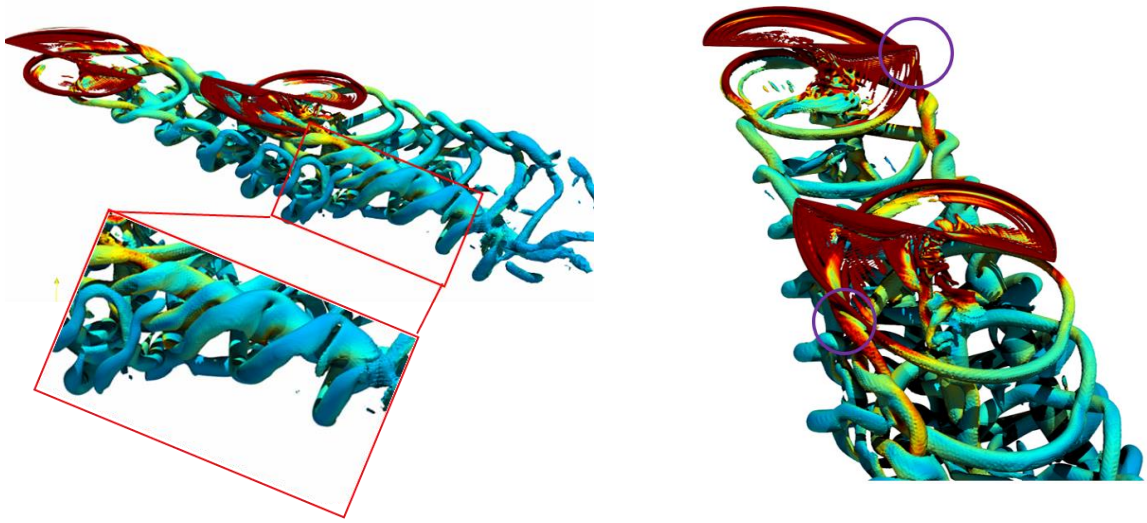

(b) (c)

Figure 2-35 Snapshot of Q-criterion iso-surfaces colored by vorticity Magnitude :(a): Hover (b): Forward Flight (Showing Wake interactions), and (c): Top view of Forward flight (Showing tip-wake interaction)

2.4.2 Near-Field Acoustics

Again, we examine the directly computed acoustic field to quantify the noise generation mechanism of multirotor systems both in hover and forward flight conditions. The same acoustic grid resolutions are utilized here.

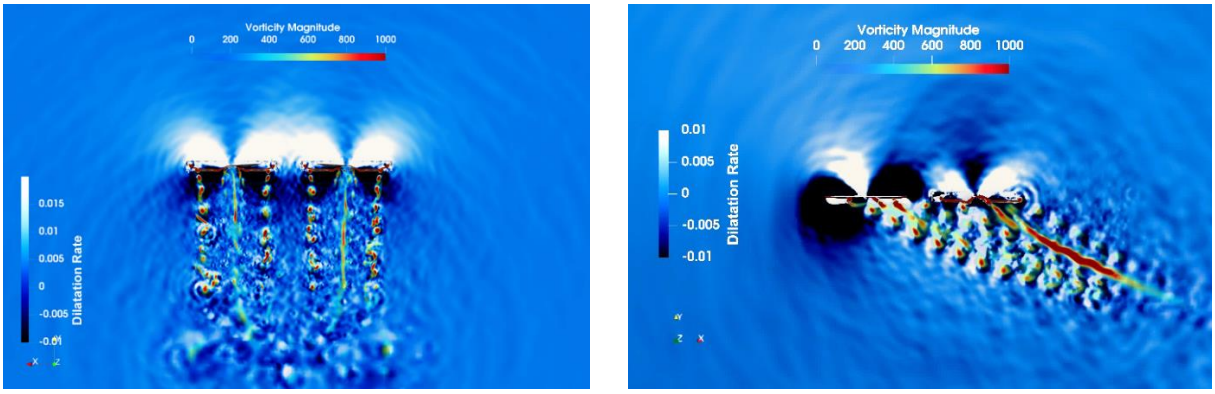

(a) (b)

Figure 2-36 Vertical slice showing snapshot of Vorticity Magnitude overlaid on Dilatation Field. (a): Hover, and (b): Forward Flight

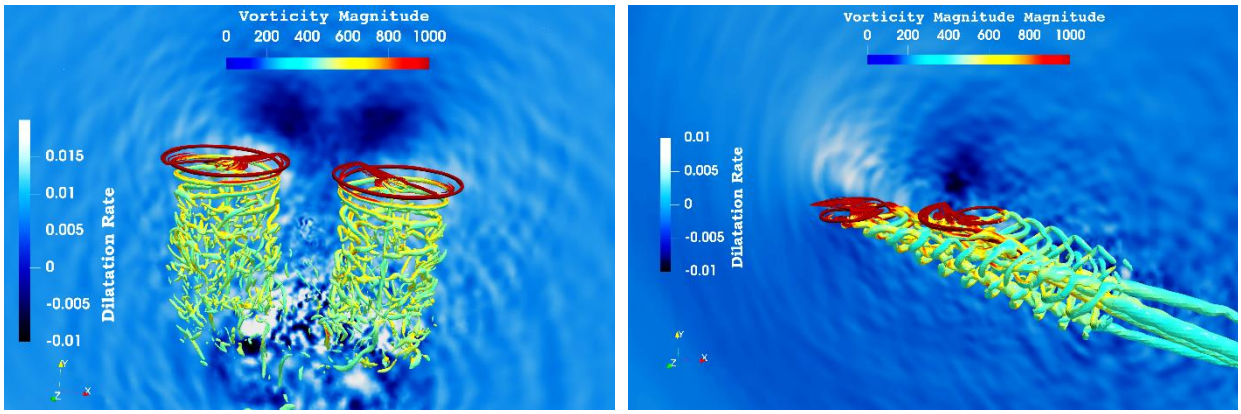

(a) (b)

Figure 2-37 Snapshot of Q-criterion with pressure fluctuations in background. (a): Hover, and (b): Forward Flight

Looking at Figure 2-36 & Figure 2-37, we can draw some preliminary conclusions. We notice a relatively ordered propagation of tonal content from the blades in the hover case. For that of the forward flight, we see a significant intersection from the rotors as well as the wakes wake. The tip vortex from the rotors interacts with the wake shedding in the front rotor. Similar conditions are seen in the aft rotor. This generates sound, as in turbulence-ingested noise, as evidenced in Q-criterion contours overlaid with the Dilatation Rate plots in Figure 2-38 and has been studied by others for a single rotor [89,90]. We see in the region of interaction, bands of rapidly changing acoustic pressure values ensue. This is indicative of a high-frequency phenomenon, possibly the generation of broadband noise.

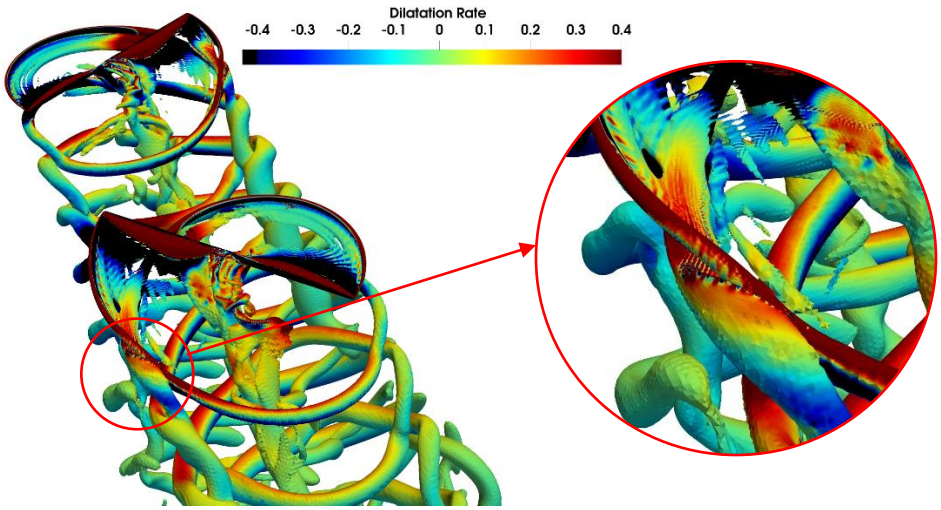

Figure 2-38 Snapshot of Q-criterion Iso-Contours overlaid with Dilatation Rate showing Tip-vortex – wake interaction in forward flight.

Tonal Noise Sources

We investigate the origin of the increase in the tonal noise in forward flight. Due to the angle of attack of the freestream velocity, and its incidence on the rotors, as well as the asymmetric nature of the rotor loading in forward flight (with an advancing side, and retreating side), there is increased static pressure experienced by the blades, which results in higher tones. Additionally, there is an increase in the unsteady loading of the blades, evident in the thrust coefficient plot in Figure 2-31. This unsteady loading occurs at "one per revolution" which increases the tones at the blade passage frequency [93].

To further identify the noise sources, again, we employ the technique of Spectral POD [32]. Note that we utilize this technique to only get the general identifiable trends in the noise sources rather than exact quantification of the sources. We select the first three tonal frequencies for both the hover and forward flight case, as well as the broadband frequencies from low to mid-frequency range from the spectral plot in Figure 2-45. Note that for the forward flight case because both rotors operate at different rotational speeds, the Δf between the fundamental tones is ~20 Hz. Due

to the prohibitive sample size required to achieve such frequency resolution, we only show an intermediary frequency (154 Hz). As such we show the first mode which shows energy contributions of ~75% because it is closer to the aft rotor BPF (162Hz), and the second mode, which shows energy contributions of ~23%. Much like the case of the DJI rotors, we see that the hover case (Figure 2-39a) has most of the periodicity originating from the blade surface, and some contributions from the near blade wake region. Increasing the BPF harmonics sees only the blade region as the source of the periodicity. This suggests that the wake noise sources are inherently a lower frequency source. Looking at that of the forward flight case, similar trends are noticed. An additional feature we see is some interaction of waves from the aft rotor with the wake. This is perhaps due to the interaction of the on-coming flow with the rotors.

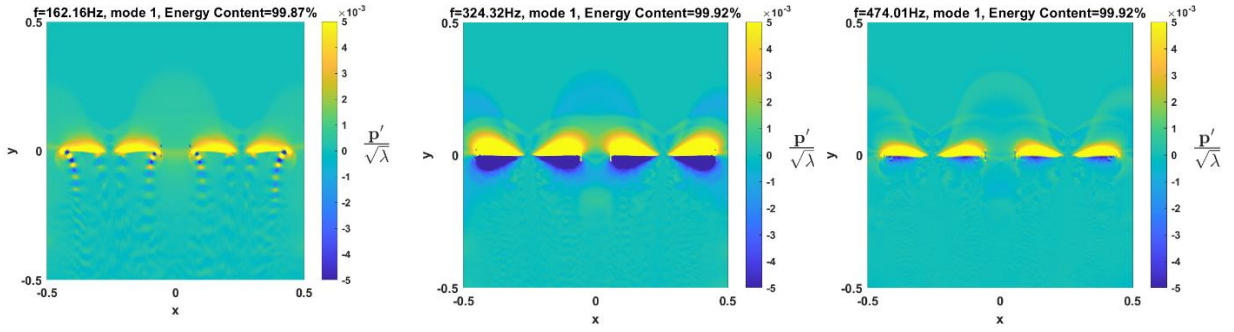

(a): Hover Case

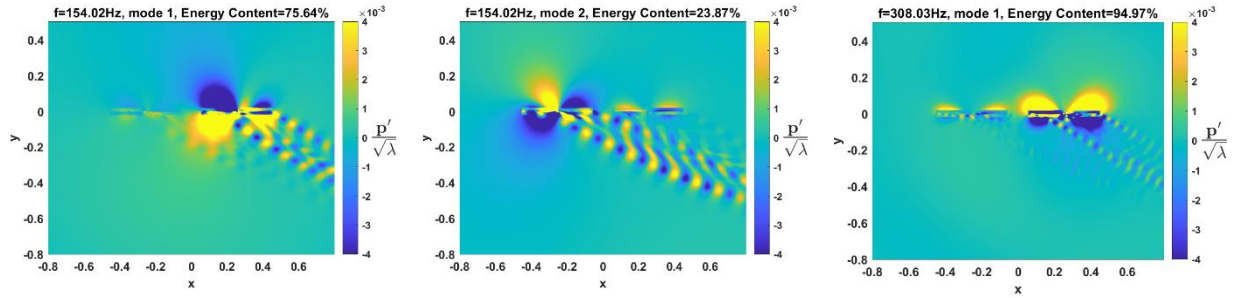

(b): Forward Flight Case

Figure 2-39 Spectral contour plots at tonal frequencies

Broadband Noise Sources:

Switching to the broadband frequencies, we notice again similar trends for the hover case as discussed earlier with the DJI cases. We look at spectral contours in Figure 2-40. For the forward flight case, however, we notice some interesting phenomena. First, the first mode is not sufficient to describe majority of the flow physics, and as such, we present the first two modes, which have energy levels >~85% on average. Additionally, at low broadband frequencies, we see some contributions from the blade region, as well as the wake. We also see some interaction of the pressure waves from the fore rotors with that of the aft rotors. With increasing frequency, however, the contribution of the wake is diminished. Additionally, we notice some back scattering of pressure behind the aft rotors. This is postulated to be a result of the tilt of the rotors in forward flight and their interaction with the on-coming stream of velocity. The pressure pulses generated by the fore rotors get deflected rearwards by the relative motion of the rotors in forward flight.

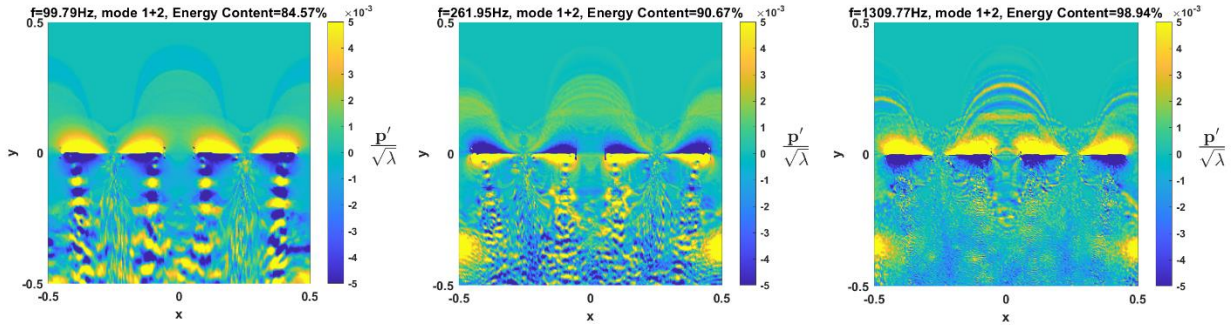

(a): Hover Case

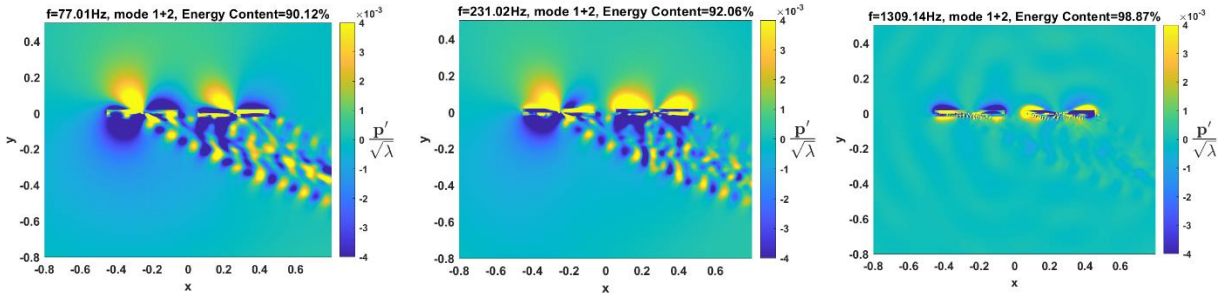

(b): Forward Flight Case

Figure 2-40 Spectral contour plots at broadband frequencies

To correlate the source of the broadband noise with the aerodynamic features, we look at the wake effects in forward flow. It is known that the effects of mean flow incidence on a rotating source is equivalent to an unsteady acoustic source [94]. Also, from the linear acoustic theories, by converting the convective wave equation to a simple wave equation, it has been shown that there is some influence of uniform flow on overall noise levels [94,95]. From Figure 2-40, we can identify and confirm that some broadband contributions arise from the wake effects in the lower frequencies, but we cannot explicitly quantify this source. We also look at the vorticity magnitude in the rotor plane. We see in Figure 2-34 that there is unsteady vortical flow shed from the fore rotors interacting with the aft rotor. Blade-vortex interaction is well known to be a source of broadband noise [96]. This, coupled with the interaction with the on-coming flow, generates some additional broadband noise when the blades interact with its own tip vortex as well as the wake, as shown in Figure 2-38.

Additionally, we notice that there are some broadband sources originating from the blades (Figure 2-40), we attempt to identify the sources by extracting vertical cuts across the blades at 0.72 Radii. We show streamlines of the velocity magnitude for the static case, as well as the advancing and retreating blade of the forward flight case (Figure 2-41). There is a separation bubble in each case with that of the advancing side being larger due to the stronger boundary layer development and significantly higher surface velocity. The retreating blade has clearly defined separation bubble that is moved closer towards the leading edge and shows total blade stall. The phenomenon of large-scale separation is known to increase low frequency broadband noise [97,98]. By plotting the root mean square (RMS) of pressure on the blades shown in Figure 2-42, we see stronger development of the turbulence boundary layer noise for the forward flight case.

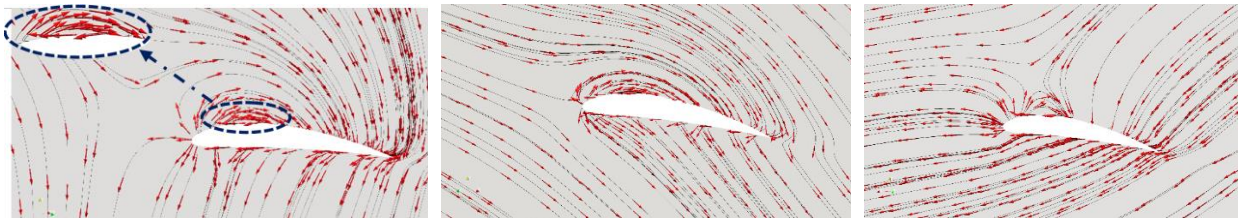

(a) (b) (c)

Figure 2-41 Streamlines of Velocity Magnitude on blades of (a): Hover, (b): Advancing side Forward Flight, (c): Retreating side Forward Flight.

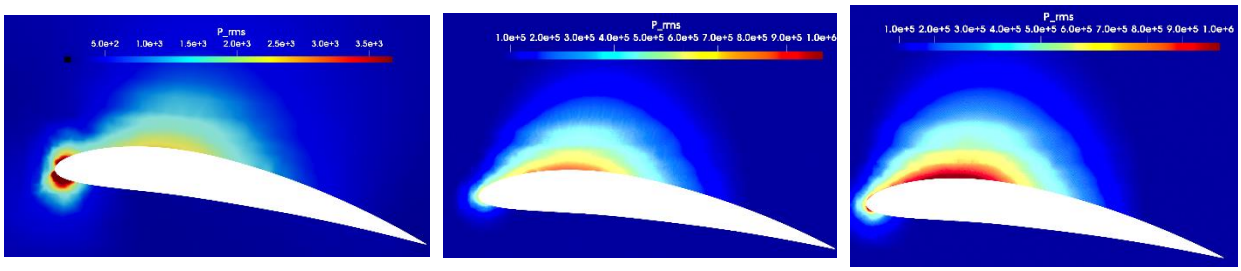

(a) (b) (c)

Figure 2-42 Snapshot of Root Mean Square (RMS) of Pressure near blades of (a): Hover, (b): Advancing side Forward Flight, (c): Retreating side Forward Flight.

2.4.3 Far-Field Acoustics

The Ffowcs-William Hawking's formulation is again used here to extend the near field to obtain the acoustic far field. A sampling rate of $1.25x10^{-5}$seconds, comparable to experimental data by Zawodny & Pettingill [20], is used. Data is collected after 30 rotor rotations. A total of 16384 samples are collected for the current case study. An FFT of the data is performed with 75% hanning windowing. Power spectral density, and sound pressure level (SPL) plots with frequency resolution of 5 Hz are shown, as well as OASPL directivity plots with integral frequency range of 100Hz to 1.3kHz. For this case, the top-capped control surface cylinder is placed at a radius of 0.5m from the center of the two rotors for the hover case and angled at ~10 degrees for the forward case and is shown in Figure 2-43.

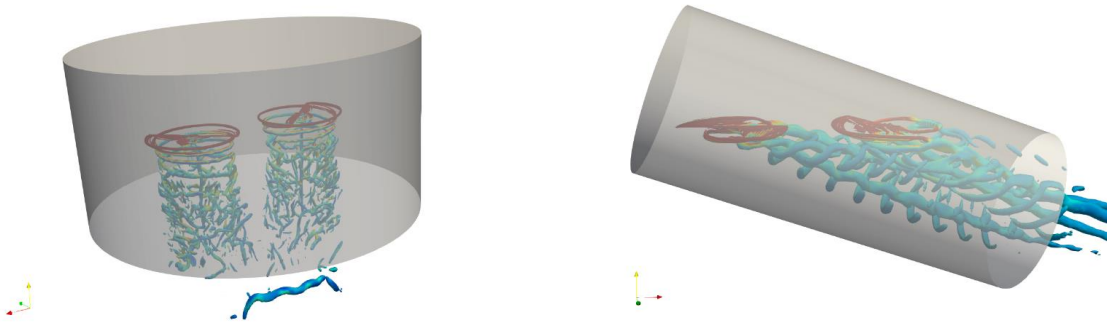

(a) (b)

Figure 2-43 FWH Control Surface At ~2.6R with Q-Criterion Iso-Contours of Vorticity. (a): Hover case, (b): Forward Case (T-motor Case)

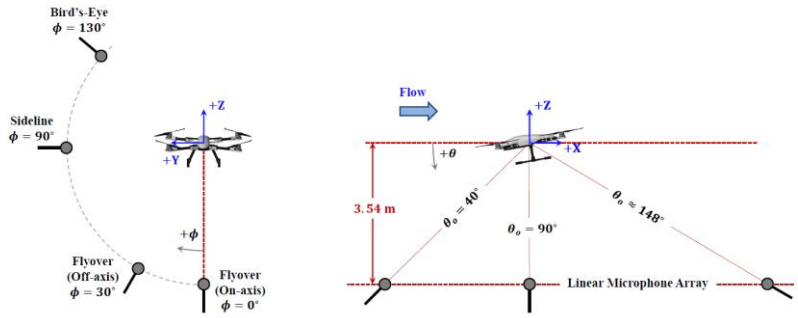

Figure 2-44 Schematic showing the Microphone locations for far-field measurement [20].

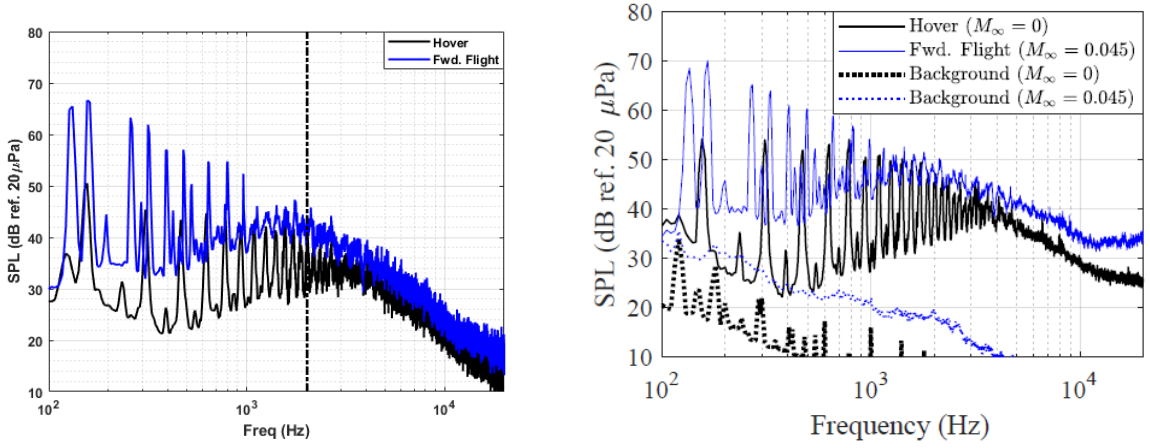

(a) (b)

Figure 2-45 On-axis flyover acoustic comparisons at 70^o geometric observer location between hover and forward flight conditions (a): HLES computation, (b): Experimental data [20]

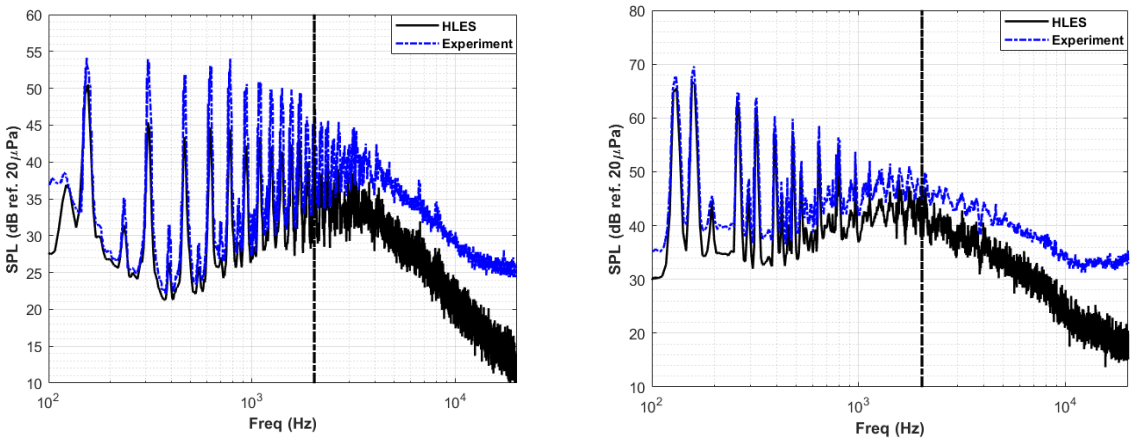

(a) (b)

Figure 2-46 On-axis flyover acoustic comparisons at 70° geometric observer location between HLES & Experimental data [20]. (a) Hover; and (b) Forward flight

Looking at the spectral plots in Figure 2-45 & Figure 2-46 we notice that for the hover case, we see a single fundamental tone or peak tone and its harmonics, this is because both rotors are operating at approximately the same rotational rate of 4800 RPM. This corresponds to a Blade Passage Frequency of ~160 Hz, comparable to that of Zawodny & Pettingill [20]. For the Forward flight case, we see two peak tones in the experimental data. This is attributed to the relatively different rotational rates of the two rotors with the aft rotor operating at a higher RPM, typical of small-scale fixed-pitch rotor systems such as these. By matching the same rotating conditions numerically, as mentioned earlier, the computational approach is seen to predict the spectra for the observer location quite closely by capturing the two BPF harmonics at approximately 130 Hz and 160 Hz.

We also notice quite an increase in tonal or periodic noise content in the forward flight case. In the case of Zawodny et al., we see ~16dB increase, whereas our computation sees about 15dB increase. The reason for the increase could be attributed to an increase in the blade loads due to

the increased inflow velocity realized by the blade sections as a result of the convection of the oncoming velocity stream. Also, the convection of the uniform flow increases the strength of the boundary layer and the loading on the blades, which increases the strength of the tones in forward flight. An additional noise occurs due to the unsteady loading generated by the rotating blades in the uniform flow, which occurs at the blade passage frequency. The difference in the levels between our computation and experimental data from Zawodny & Pettingill [20] can be attributed to the fact that we assumed symmetricity and computed using two rotors instead of all four rotors. There is a slight roll-off in the harmonics of the hover case. This is possibly due to the absence of a fuselage in our computations and may be accounted for by rotor-airframe interactions as mentioned by Zawodny & Pettingill [20]. Some tonal energy in the subsequent harmonics is seen in the hover case because although the rotors do not have transfer of vortical structures between them, their acoustic pressures do interact and get excited at the blade passage frequency harmonics.

Pertaining to the broadband noise levels, we see similar trends of increased content for the forward flight case. This was reported to be due to rotor fore-aft wake interaction [20] and is also seen in Figure 2-35, and Figure 2-38. We notice that the broadband levels are slightly lower than that of the experimental data. This is perhaps due to the absence of the fuselage. Another source of the broadband noise increase is the elevated blade self-noise (turbulent boundary layer noise, deep stall noise, and trailing edge noise) as discussed earlier. The radiation/deflection of the rotor pressures rearwards and their interaction with the wake could also influence the broadband noise increase and is seen more clearly in Figure 2-40. To better distinguish between the periodic contents and the broadband content and sources, we again utilize the periodic averaging technique [92] on the spectral data. Figure 2-47 shows the tonal and broadband extracted data. We notice

some increase in broadband levels between the fundamental tones of the two rotors. This may indicate some interference effects between the rotors in forward flight.

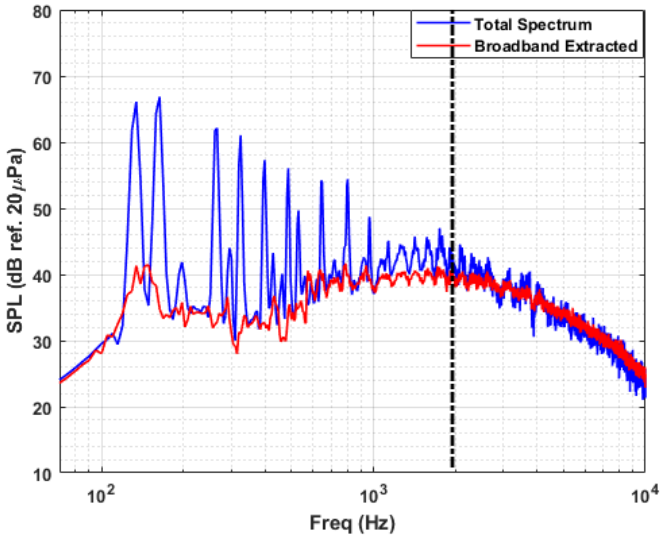

Figure 2-47 Periodic Averaging of SPL for Forward flight

To separate the effects of the blades and the wake noise sources, we again present spectral results for the forward flight case using the blade surfaces as FWH control surfaces, compared to the cylindrical control surface approach that encompasses all the sources (both blade and wake) in Figure 2-48. We again see that the low-mid frequency broadband levels are less in the blade surface sources. This indicates that the wake contributes comparably to the broadband noise at the lower frequency ranges. Additionally, we notice a slight increase in unsteadiness in the case of the aft rotors, which may indicate some acoustic interference from the fore rotors.

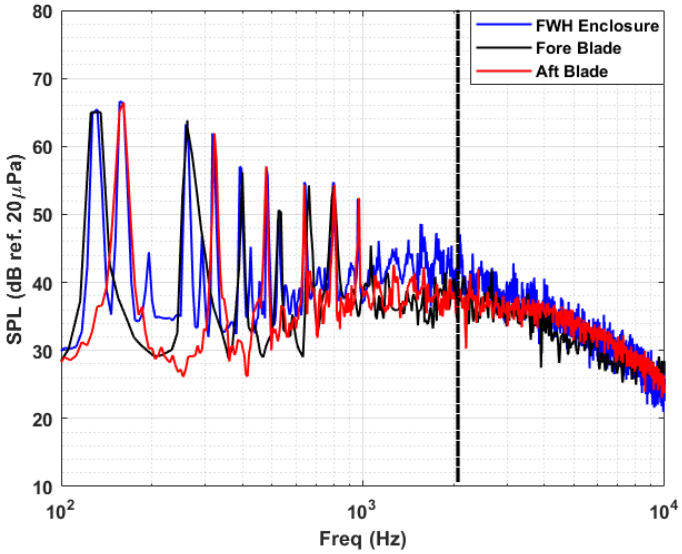

Figure 2-48 SPL spectra of Forward flight case comparing Blades to Cylindrical Enclosure.

Directivity Study

Next, we look at the directivity plots for both the hover case, as well as the forward flight case. We plot out the Overall Sound Pressure Level (OASPL) for both cases (Figure 2-49). An integral frequency range of 100Hz to 1.1kHz (resolution cut-off frequency) is utilized. We notice a significant increase in the overall noise levels in the case of the forward flight case across all rotor azimuths. There is ~3dB difference with experimental data [20]. This is attributed to the fact that the experimental data was obtained with all four rotors with a fuselage, whereas our computation only used two isolated rotors. Also, we notice that due to signal pollution by the downwash, the experimental data omitted directivity values between 70 and 110 degrees for the hover case. The FWH computation did not have this limitation. Due to the range of integral values used for the OASPL computation, we see that the wake region would generally act as an impedance to the tonal content but would increase the broadband (higher frequency) content due to the mixing effects. This BBN increase may not be captured in the directivity due to the acoustic cut-off frequency, and thus shows a reduced OASPL levels.

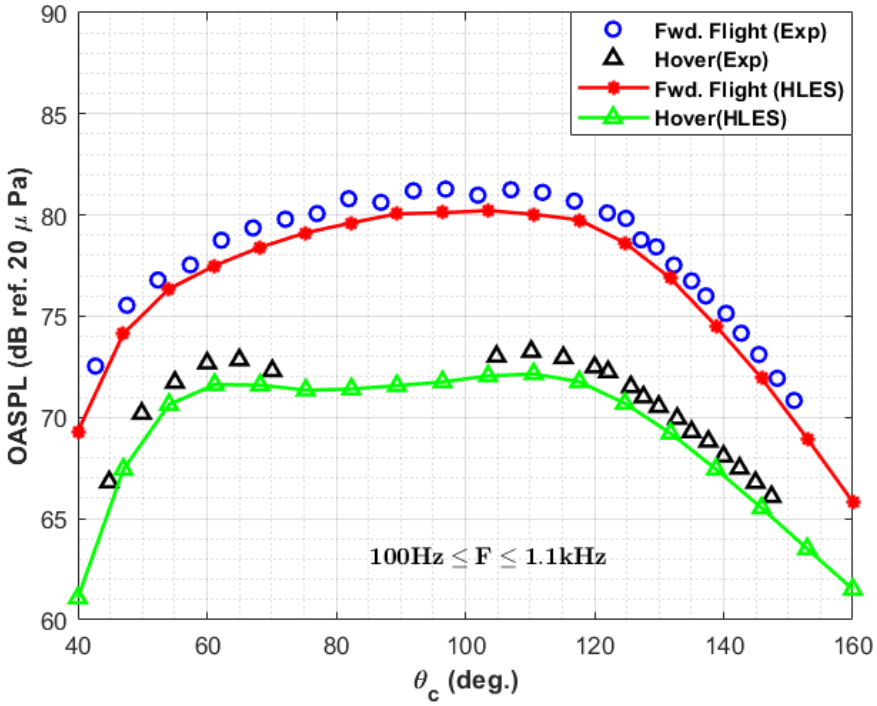

Figure 2-49 On-axis flyover OASPL plot comparing Hybrid-LES-URANS computation to Experimental data [20].

2.5 Interim Conclusions

A study of noise generation due to the rotor-rotor interactions at hovering condition, as well as in forward flight were presented here. Near field flow properties as well as the acoustics were resolved using Hybrid Large Eddy Simulation (LES) -Unsteady RANS (HLES). Ffowcs-Williams & Hawkings' integral technique was then used to extend the resolved near-field acoustics to the far field.

2.5.1 Hovering

These simulations enabled us to understand the changes to the aerodynamics and the acoustic field resulting from the rotor-rotor interactions. Some interesting observations are:

(1) The loading on the blades now includes a periodic component, in addition to the classical steady component (Figure 2-11). This periodic component is produced by the approach of

a blade of one of the propellers toward a blade of the other rotor (Figure 2-17). This, along with the direct interaction of the propagating tonal noise causes modification of the tonal noise. This is a phenomenon that can be utilized in trim optimization via phase synchronization.

(2) Our simulations predicted well the sound spectra consistent with the experimental observations Zhou and Fattah [17]. Both the simulations as well as the experiment, have shown significant increase of the BBN (of the order of 10 dB.) for the two hovering rotors vs the isolated one. By examining the resolved near and far fields acoustics, and by conducting Spectral Proper Orthogonal Decomposition (SPOD), and periodic averaging, we were able to identify the mechanisms leading to this increase in the BBN: In addition to BBN sources from the blades and from the wakes, additional new sources include:

   a. The gap between the two rotors. In this new mechanism, an intense vortex generation and interaction are observed in the gap between the two rotors (Figure 2-12). This was also associated with an increase in the turbulence kinetic energy in this region, and an upward jet-like flow, indicating an additional source of BBN. The enhanced TKE in the gap (Figure 2-10b) and the associated pressure fluctuations (Figure 2-14b) could potentially be sources of the broadband noise.
   b. The interaction of the two wakes contributing at the low-frequency range (Figure 2-21), and
   c. The enhanced pressure fluctuations on the blades were caused by the vortex-blade interactions.

2.5.2 Forward Flight

We then moved towards validation against experimental data under forward flight conditions. Some of our key results are summarized here. We show in Figure 2-45 our simulations of the two inline rotors at the forward flight compared to the corresponding case in hovering. Further detailed examination revealed results consistent with previous observations[20,22,23] as well as the mechanisms involved.

In particular, Figure 2-45 shows that our predicted spectra are in good agreement with experimental observations [20]. The convection effect can partially explain the observed enhancement in the tonal and BBN, but this only amplifies the radiation of the sources, not the sources themselves.

As in hovering case, the passing of one rotor blades by the other rotor blades creates periodic loading. This, along with the direct interaction of the radiated tones increase the tonal noise.

For the BBN, both the simulations as well as the experiment show significant increase in the BBN (as large as 15 dB). In addition to the convection-enhancement effect, the blade and wake sources, and the gap flow, the simulations revealed some interaction- specific mechanisms for BBN enhancement in forward flight:

1. The vortical structure of the forward rotor impacts both its blades as well as the wake flow of the aft rotor (Figure 2-35 & Figure 2-38). This leads to the generation of BBN.
2. More significantly, we see in Figure 2-41 & Figure 2-42 a sizable separation bubble (deep stall) on the aft rotor blades generating significant BBN due to the instability of the separated shear layer and reattachment.

3 Application of Data Reduction Techniques to Modeling Rotor Noise

High-Fidelity computations are often used in predicting the tonal and broadband noise of propellers and rotors associated with Advanced Air Mobility Vehicles (AAMV). But LES is both CPU and storage intensive. We present here an investigation of the feasibility of reduction methods such as Proper Orthogonal Decomposition as well as Dynamic Mode decomposition for reduction of data obtained via HLES to be used further to obtain additional parameters. Specifically, we investigate how accurate reduced models of the high-fidelity computations can be used to predict the far-field noise.

3.1 Numerical Approach

As discussed in Chapter 1.1, several options exist for model reductions in literature. We explore two of such methods for their level of accuracy after reduction of the original data has been performed:

3.1.1 Proper Orthogonal Decompositon (POD)

POD is generally utilized in both experimental and numerical fields to extract dominant flow features. There exist numerous formulations for POD, however, we utilize the snapshot method [99]. The general formulation is to decompose a field vector, $X'(x,t)$ into a set of spatial functions $\Phi_r(x)$ and its random set of time coefficients $a_r(t)$:

$$X'(x,t) = \sum_{r=1}^{\infty} a_r(t)\Phi_r(x) \tag{3.1}$$

The original dataset u is constructed such that the matrix is a time series in that $u = u[x, y, time]$. The general algorithm for the snapshot method is shown here:

- Extract the fluctuating components of the flow by subtracting the mean:$X' = X - X_{mean}$

- Next the correlation matrix of the snapshot matrix $C = X'X'^T$
- We then find the eigenvalue and vectors of the correlation matrix such that:

$$[a_r\ \lambda] = eig(C) \tag{3.2}$$

Where a_r are the temporal modes.

- The spatial modes are reconstructed as $\Phi_r(x) = X' * a_r$
- The reconstructed field $\widetilde{X_r} = a_r * \Phi_r(x)$

Another approach to the algorithm involves the use of the singular value decomposition (SVD) method, where the correlation matrix and eigen value steps can be replaced by:

$$C = U\Sigma V^T \tag{3.3}$$

And a_r is redefined as:

$$a_r = \Sigma_r V_r^T\ \&\ \Phi_r = U_r \tag{3.4}$$

3.1.2 Dynamic Mode Decomposition (DMD)

The DMD algorithm was originally created to build on the limitations of POD. One of POD's limitations is the inefficiency in identifying structures in flow fields that are heavily time dependent. DMD computes the set of dynamic modes which are each associated with a frequency and a decay/growth rate. It is useful for finding correlations with coherent structures in the domain and has the capability to consider the temporal dimension as well in the form of an FFT.

We first start the algorithm by splitting the snapshot matrix into two – the first one start from $t = 1$ to $t = n - 1$. And the second matrix goes from $t = 2$ to $t = n$.

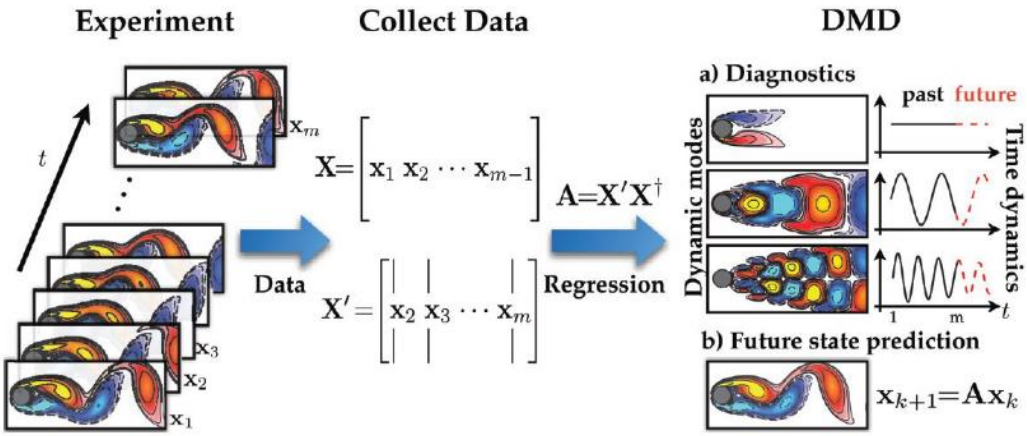

Figure 3-1 Overview of DMD for vortex shedding of a cylinder[99]

Next, the following equations are used for the development of the DMD:

- The equation that relates each snapshot to the next:

$$X' = AX \tag{3.5}$$

- Next, a singular value decomposition of X is generated:

$$C = U\Sigma V^T \ \ or\ in\ MATLAB,\ \ [U,S,V] = svd(X) \tag{3.6}$$

- Given the rank or number of modes for reconstruction, r, $[U,S,V]$ are truncated from 1 to r. The Low-rank subspace matrix is computed as:

$$\tilde{A} = U_r^T * X' * V_r * S_r^{-1} \tag{3.7}$$

- Next the eigenvalues λ and eigenvectors ω are obtained:

$$[\omega, \lambda] = eig(\tilde{A}) \tag{3.8}$$

- The reconstructed reduced order model is then given as:

$$x(t) = \sum_{j=1}^{r} \Phi_j e^{\omega_j t} b_j = \Phi\, exp(\Omega t) * b;\ where\ b = \ \Phi^{-1} * X_1 \tag{3.9}$$

Here, x(t) represents the variables of interest, say pressure, or velocity. With this reconstruction, we can extend the data set for different variables.

3.1.3 Choice of Mode Truncation

The general goal of these reduction methods is to identify the minimum number of modes that can describe a system without significant loss of information. This usually requires a metric for specifying the truncation. For the POD case, the algorithm allows for a simple method of ranking the weights of each mode by comparing the singular values to the original data. For DMD, however, this is not so straightforward as there is no longer a singular matrix for comparison. To remedy this, two approaches can be utilized. The first one is to define a hard limit called the optimal hard threshold, τ, for the singular value truncation such that [99]:

- If $\boldsymbol{X} \in \mathbb{R}^{n \times n}$ then

$$\tau = (4/\sqrt{3})\sqrt{n}\gamma \tag{3.10}$$

- If $\boldsymbol{X} \in \mathbb{R}^{m \times n}$ and $m \ll n$ then $(4/\sqrt{3})$ is replaced by the aspect ratio $\beta = \frac{m}{n}$:

$$\tau = \lambda(\beta)\sqrt{n}\gamma \tag{3.11}$$

$$\lambda(\beta) = \left(2(\beta + 1) + \frac{8\beta}{(\beta + 1) + (\beta^2 + 14\beta + 1)^{\frac{1}{2}}} \right)^{\frac{1}{2}} \tag{3.12}$$

Where γ is a known noise magnitude of the system. If the noise of the system is not known as most real-world applications, the median singular value can be used to estimate the system. The equation for this estimation is discussed by Gavish & Donoho [100].

The second more common approach is the energy truncation method. By using the Singular value decomposition approach, the singular value matrix Σ is used to gain insights into the total energy of the system such that:

$$\sigma_r = \frac{diag(\Sigma_r)}{sum\{diag(\Sigma_r)\}} * 100\% \tag{3.13}$$

We define the truncation value, r to be the minimum of (σ_r >convergence value), where we specify for the POD case, the convergence value of 95% of the total energy of the system.

3.2 Inputs and Methodology

We consider here the flow and acoustic fields associated with an isolated propeller of a UAV. In the computational domain, the unsteady flow field and the acoustic near field are directly resolved numerically. The Hybrid LES-URANS (HLES) approach is adopted here as discussed in Chapter 2.1.2. The governing equations for the entire computational domain are the compressible, unsteady Favre-Averaged Navier-Stokes equations [67] as shown in Eq.(2.1) to Eq. (2.7).

The overarching goal of this study is to explore the feasibility of these Decomposition methods to predict the far-field noise. The far field noise is computed using Farassat's 1A formulation [80] of Ffowcs-Williams-Hawkings Equations (FWH)[64] as shown in Eq. (2.26). The formulations are modeled in MATLAB. The inputs needed for Eq. (2.26) are pressure, velocity, and their time derivatives. These are interpolated onto a porous top-capped control surface as shown in Figure 3-2.

Figure 3-2 Control Surface for Integration

The interpolation process is done in OpenFOAM, and data is output as a series of VTK files. These are then imported into MATLAB using the vtk toolbox[101].

For validation, we choose the case with an RPM of 6000 [12]. Spectral results are compared with experimental work by Intaratep et al [21], with the observer point shown in Figure 3-3:

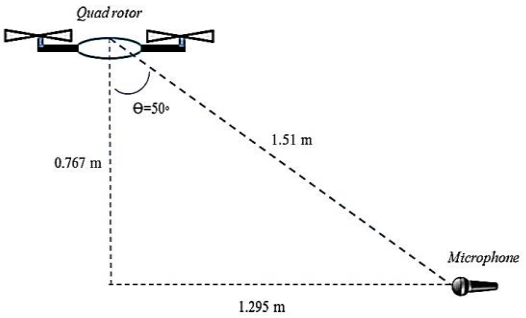

Figure 3-3 Observer location point [21]

The general workflow of the computations and framework is shown in Figure 3-4.

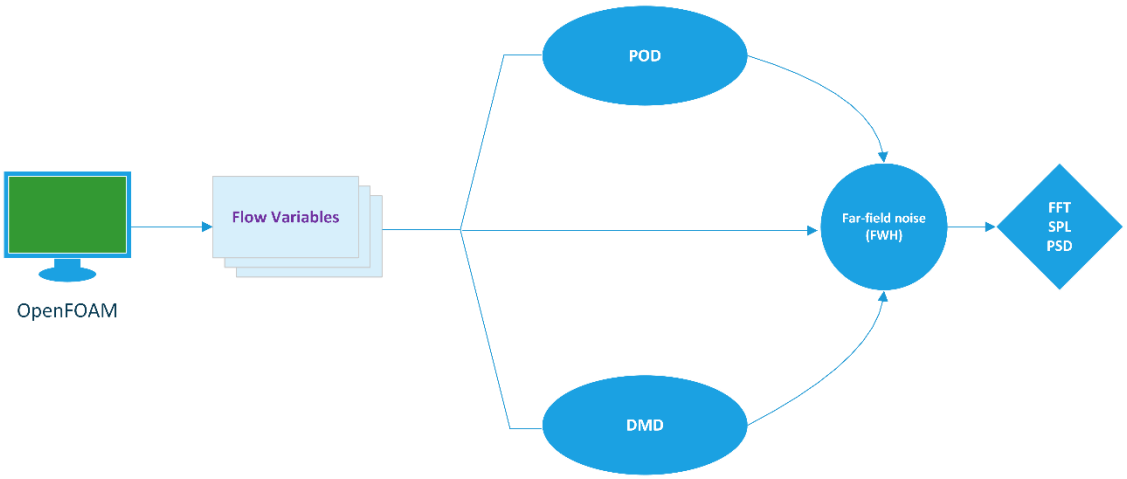

Figure 3-4 Schematic showing the workflow.

3.3 Results

We utilized high-fidelity computations of a single rotor in hover, at 6000 RPM. We show results from the computation of the near-field dilatation rate of the single isolated propeller [12]:

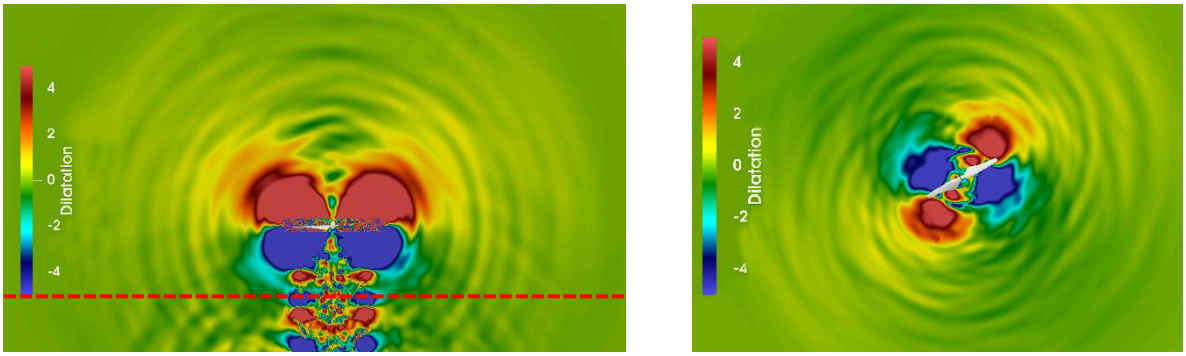

Figure 3-5 Vertical slice (left) and Horizontal slice (right) of the Dilatation Field [12]

We see that there are contributions both from the blades and the wake. To compute the far-field noise, we utilize a top-capped control surface encompassing both blade and wake noise sources (see Figure 3-2). Next, we show the far-field noise spectra compared with the experiments. A frequency resolution of (Δf) of 8 Hz which corresponds to 2^{14} samples was utilized in the Power Spectral Density Plot:

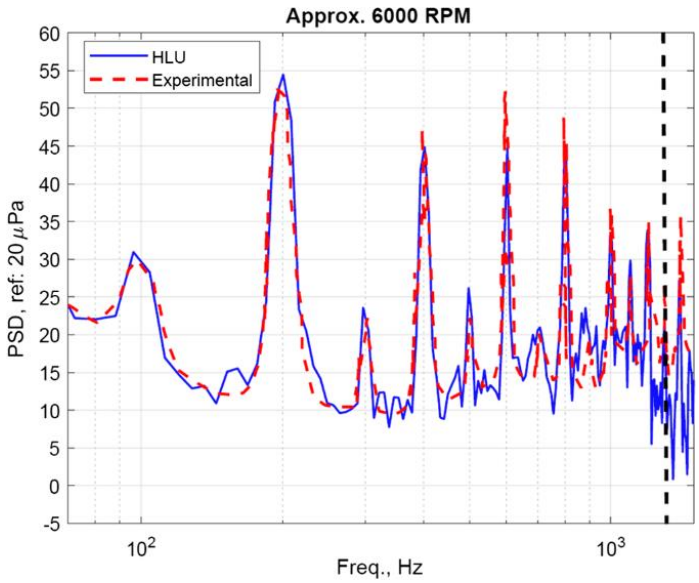

Figure 3-6 Power Spectral Density Plot compared with experimental data[21].

The spectral data above required about 600 CPU hours on an HPC with 360 processors using OpenFOAM. This is prohibitively expensive as it takes a lot of computational time and storage without an option to re-run for a different observer location after the fact.

3.3.1 Near-Field Data Reduction

As mentioned earlier, the data is extracted and interpolated onto a cylindrical surface in OpenFOAM. The desired primitive variables of interest for the eventual FWH computations are velocity, pressure, and their time derivatives. Data is collected at a sample rate of $1x10^{-5}s$. 6,755 samples are collected and utilized for the reduced order analyses.

To verify the performance of the models, we utilize an integral metric:

$$\tilde{X} = \int X dS \tag{3.14}$$

Where X is the variable of interest.

POD Results

For the POD case, we elect to use the energy truncation method for defining the mode cut-off needed for the singular value decomposition. A convergence criterion of $\sigma_r > 95\%$ is selected.

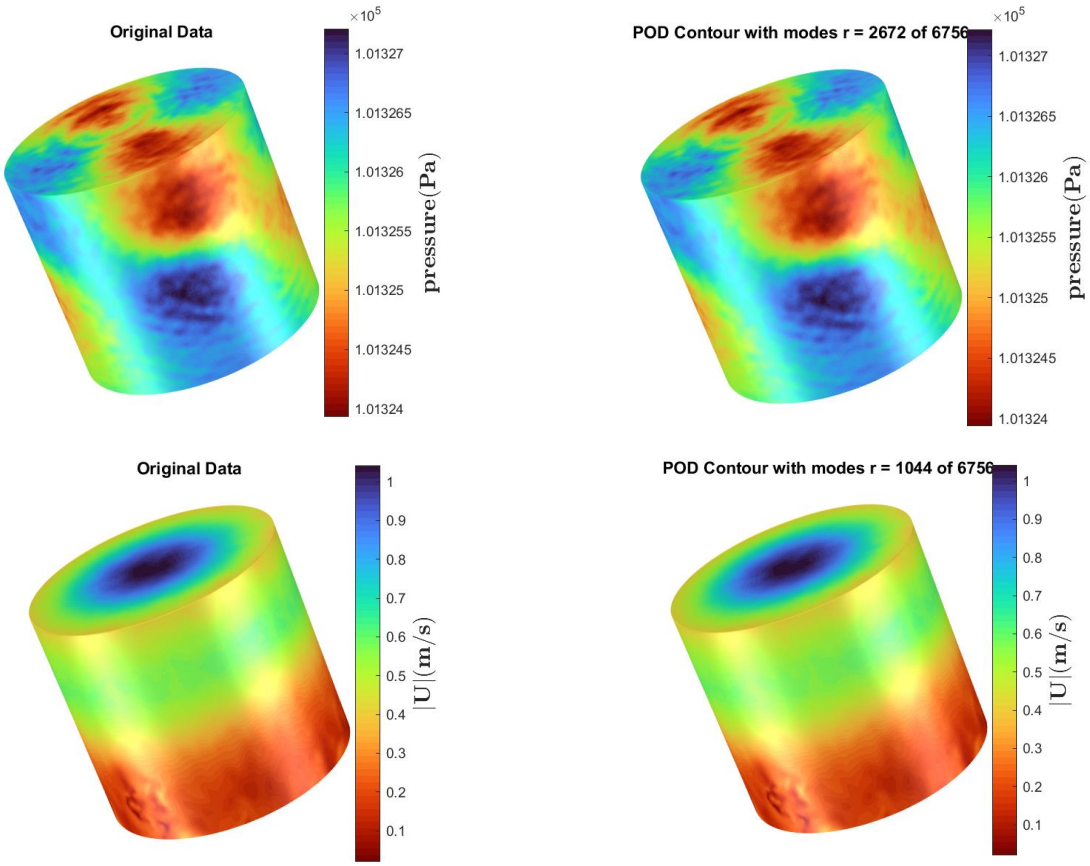

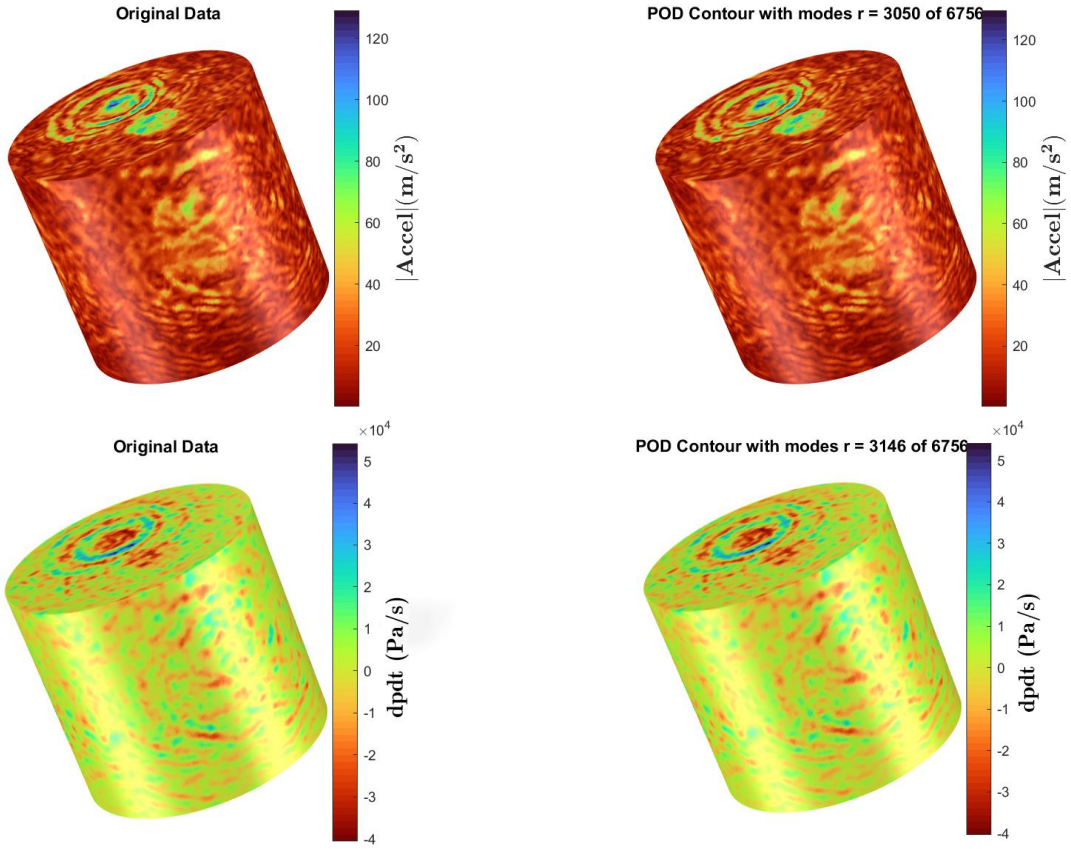

Figure 3-7 Instantaneous snapshot surface contours of variables at t=0.01s. Left: Original Data, Right: Reduced Data (POD)

Looking at the contour plots in Figure 3-7, we see that there is a great reconstruction of the near-field parameters. Results show that the velocity can be reconstructed with the first 15% of the modes which corresponds with over 95% of the total energy of the system. For pressure, however, due to the increased fluctuations, requires significantly more modes to properly represent the system at about 40% of the energy. Inherently, POD in its native form is a sort of linearization of a system and can struggle to represent higher order systems. With the optimization approach for selecting the truncation modes, we notice that the time derivative of velocity and pressures both require a significantly larger number of modes to properly represent the system at about 46-50% of the total number of modes.

Using the integral metric specified in Eq. (3.14), we investigate the accuracy of the POD reconstruction over the entire time history.

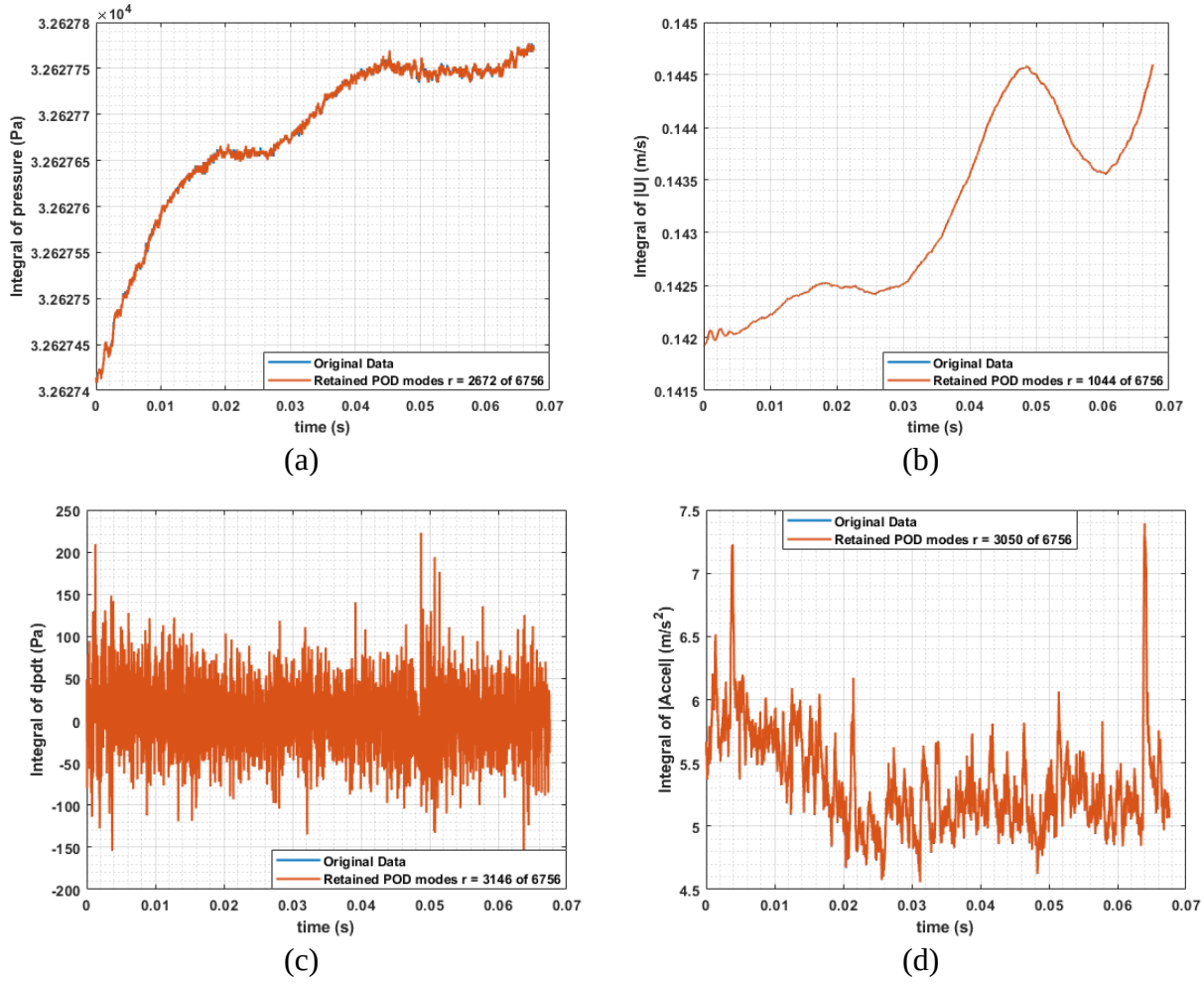

Figure 3-8 Integral metric for performance of POD reconstruction

Overall, great reconstruction of the data is seen across all timesteps. Looking at the pressure plot (Figure 3-8a), there is a slight underprediction with a room mean square error (rmse) of $3.25x10^{-5}$. Similarly, for velocity magnitude (Figure 3-8b), a rmse of $4.08x10^{-5}$. Larger deviations exist for the time derivatives with pressure derivative (Figure 3-8c) having the largest rmse of 223.93, and acceleration (Figure 3-8d) with rmse of 0.3564. One merit of the POD method is that it can be used to model the parameters of interest as an input to a neural network architecture

for control within the specified design space. It can also be used as a quick interpolation for different sampling times for comparison with any experimental result. The major demerit of this method is that it cannot, in its default form, be used as an extrapolation or future prediction method, and thus cannot be used to extend the time series for better FFT resolution.

DSMD Results

For the DMD case, we first elect to use the optimal hard threshold approach for the mode truncation. We utilize case #2; Eq. (3.11) & (3.12) for the computation of the mode truncation.

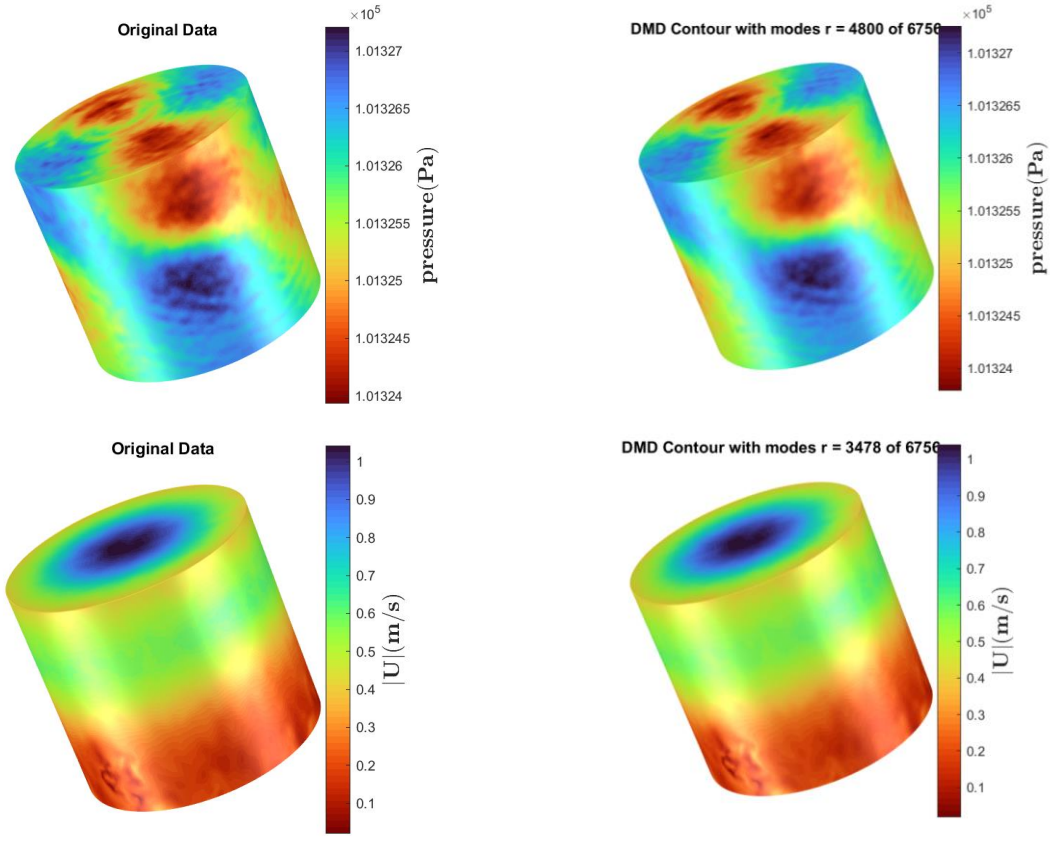

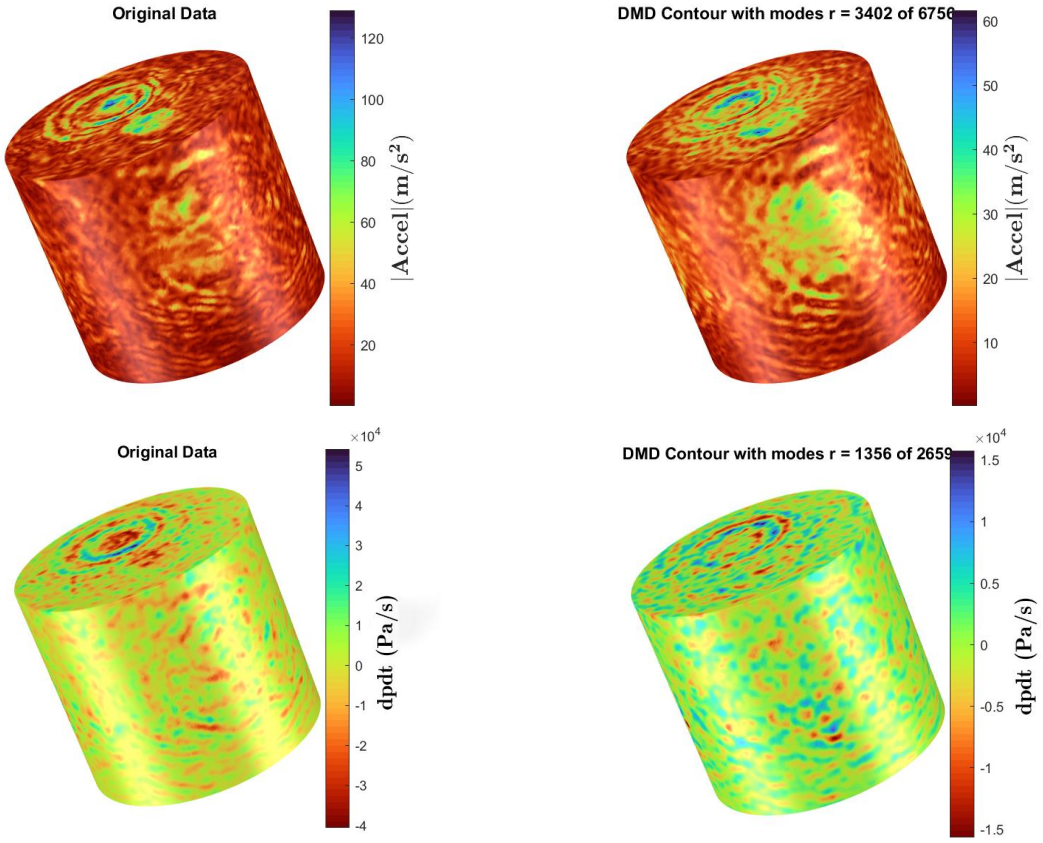

Figure 3-9 Instantaneous snapshot surface contours of variables at t=0.01s. Left: Original Data, Right: Reduced Data (DMD)

Looking at the contour plots, we notice good reconstruction of the velocity magnitude, as well as the pressure albeit not as good as results from POD case. Particularly, there is a loss of fluctuations in the case of the pressure contours, which may affect the broadband aspect of the noise. Also, we see very poor reconstruction of the time derivatives. The reconstruction of the time coefficients is based on an initial estimate of the original data rather than all the modes like in the POD. Hence, this causes severe deviations from the original data if the mode truncation is not performed well. We take a closer look by plotting the integral metric for the desired parameters.

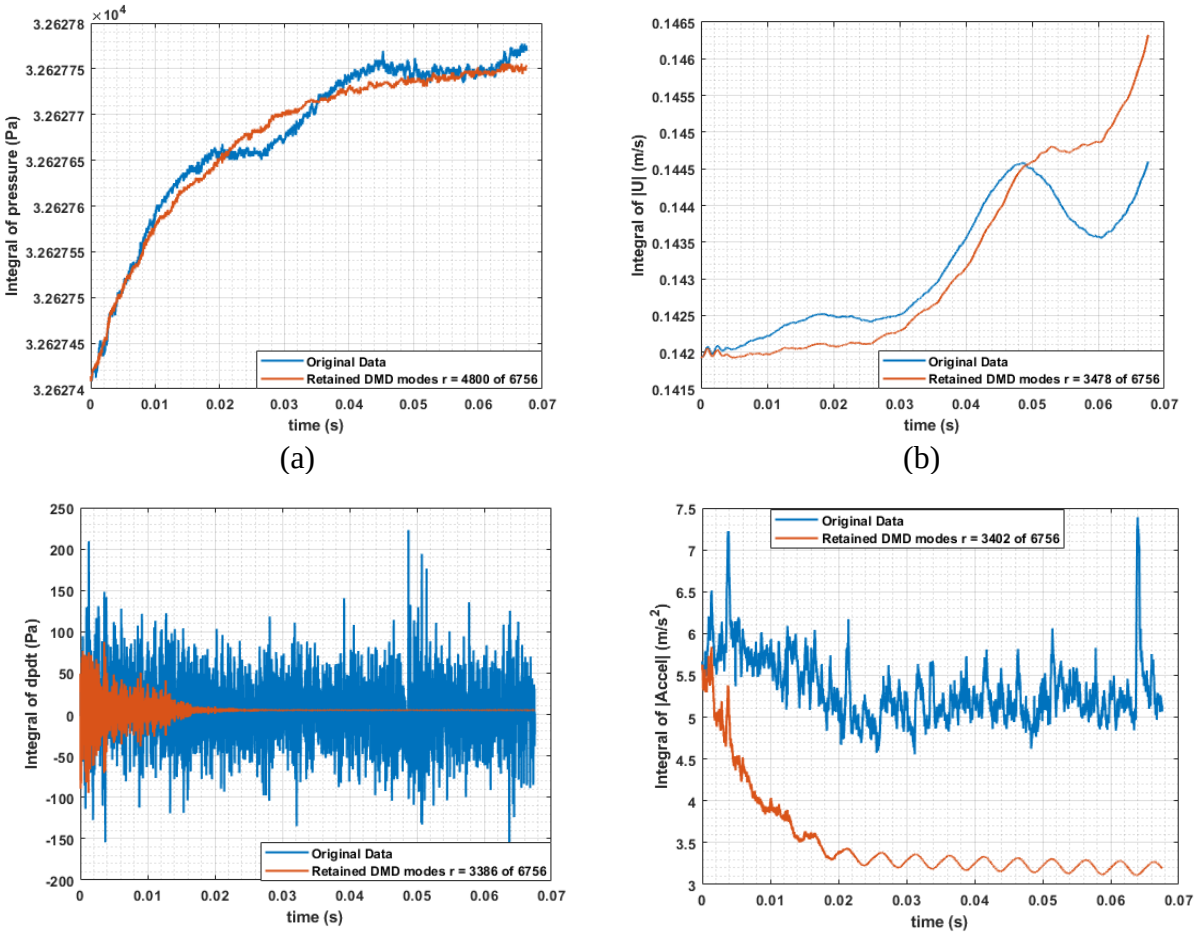

Figure 3-10 Integral metric for performance of DMD reconstruction (Optimal hard threshold)

Here, we see a good trend for the pressure, although there is some loss of unsteadiness which may translate into loss of broadband content in the far-field noise. A reported rmse of 0.0033 is obtained for pressure. The velocity magnitude shows good reconstruction in the first few time steps but deviates quite significantly afterwards with a rmse of 0.0074. Both the time derivatives are predicted extremely poorly and are not usable for further computations. To remedy this, we apply the energy truncation approach with a convergence criterion of $\sigma_r > 99.8\%$. Comparable improvements are seen in the pressure and velocity time derivatives at the expense of a significantly increased number of modes required. It is important to note that using all the modes does not automatically improve the reconstruction accuracy and does cause the mode amplitudes

for the time coefficients to grow exponentially to unreasonably large values. As such the cut-off criterion must be chosen carefully.

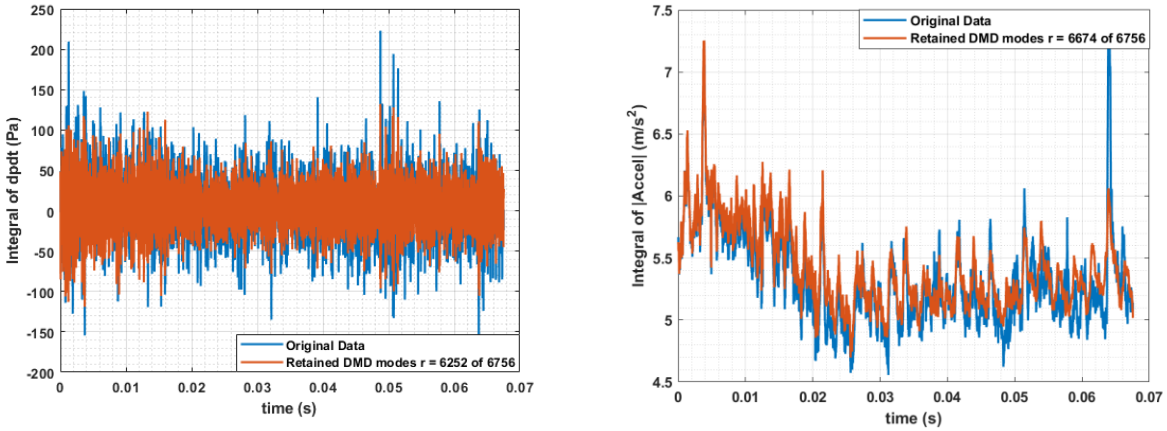

Figure 3-11 Integral metric for performance of DMD reconstruction (Energy Truncation Approach)

A merit of the DMD approach is that it can be used for future prediction or forecasting of the time series via the time coefficient reconstruction in the algorithm. However, the accuracy of the prediction might need to be investigated, perhaps using a predictor-corrector method could increase its fidelity. This could then be implemented in a control system for active noise control of rotors.

3.3.2 Far-Field Acoustic Pressure & Spectral Reconstruction

The reconstruction parameters are used as input to the formulation 1A of the Ffowcs Williams-Hawkings equations [80] (Eq.(2.26)). The resulting far-field acoustic pressure time history is compared with the original HLU computations in Figure 3-12. For clarity, we show the results for only one blade rotation, that is for a 6000-rpm case, a time window of 0.01 seconds.

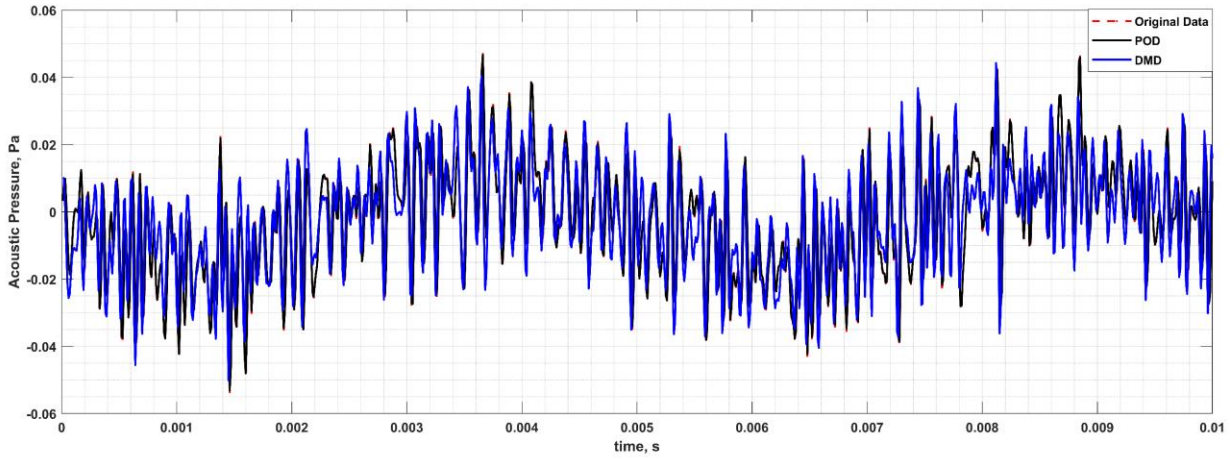

Figure 3-12 Far-field acoustic pressure time history comparison between reduced order models and HLES over one rotor rotation.

Very good reproduction is seen in the POD case compared with the HLES results with some slight underpredictions in the fluctuations (a rmse of 0.0018). For the DMD case, however, there are notable variations in the pressures, with some under-resolution of the fluctuations seen, which may, again, result in poor broadband reproduction. The general peaks and troughs are however captured quite well. A reported rmse of 0.0145 is obtained.

Spectral Reconstruction

The resulting power spectral density (PSD) plot from the HLES computations (Figure 3-6) was obtained using a frequency resolution (Δf) of 8 Hz. The reduced order models can only be resolved to (Δf) of 16 Hz due to the smaller sample size. To better compare, we first re-compute the PSD of the HLU to match that of the reduced order models for better comparison of their performance. In Figure 3-13, we compare the two resolutions of the HLU case with the experimental data [21]. We note that there is a slight over prediction of the low frequency broadband mainly because there isn't much resolution there and thus misses those points. However, the general trends are good enough for comparison with the reduced order models.

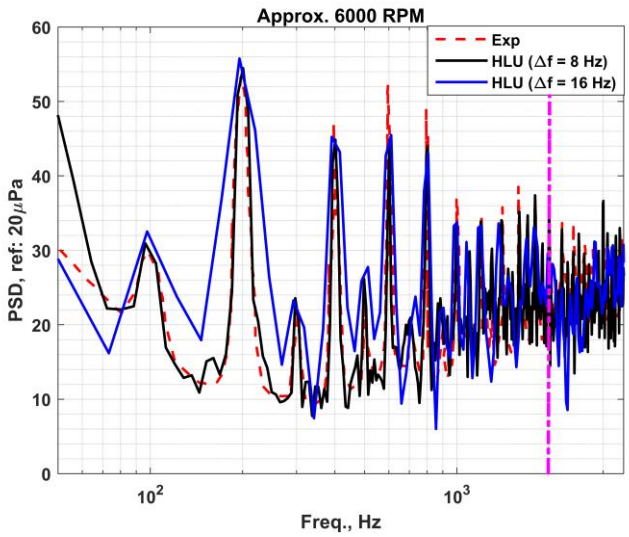

Figure 3-13 PSD plot comparing effect of frequency resolution of HLU to Experimental data [21]

Next, we compare the results of the POD and DMD spectral reconstruction with that of the comparably resolved Original HLU dataset. Figure 3-14 shows that the POD can reproduce, unsurprisingly the spectra quite well, almost matching that of the original data. With the DMD case, it can capture the tonal levels for the first few harmonics perfectly, but completely misses the broadband content. Additionally, it does not capture the shaft rate harmonics or the sub-harmonics, which indicates that it does not capture the contribution of the wake sources which have been proven to be the source of the sub-harmonics [12].

Also, note that the cut-off frequency for the DMD case seems to drop off quite sooner than that of the original dataset. This may be due to the linearization performed in the time coefficient reconstruction.

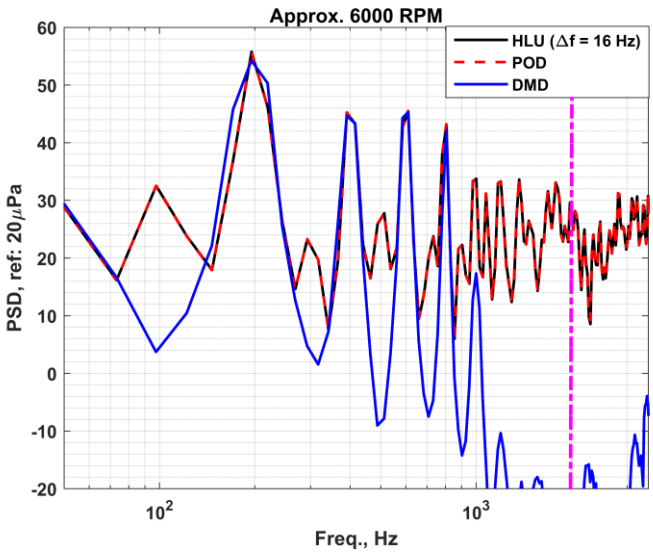

Figure 3-14 PSD plot comparing Original Data with the Reduced Order Models

3.4 Interim Conclusions

Overall, two data reduction techniques have been explored, and their application to acoustic pressure prediction discussed. The input parameters were pressure, velocity, and their time derivatives. The test case selected was an isolated UAV rotor [12], with rotational rate of 6000 rpm. Snapshots of the data mapped onto a cylindrical surface were utilized in the POD and DMD reconstruction, with an eventual FFT performed to ascertain their spectral performance. A critical step in the development of the data reduction was the choice of the mode truncation. Two methods were mentioned – the mode energy truncation approach, and the optimal hard threshold method.

The POD method utilized was the snapshot method using the singular value decomposition approach. The truncation method used was the mode energy truncation. The results showed near-perfect data reconstruction with as low as only 15% of the mode energies needed in the case of the velocity magnitudes, with the time derivatives needed slightly higher percentages for good reconstruction. The spectral performance showed matching reproduction with the original dataset.

The POD reduced model can be utilized for interpolation of the dataset for various sampling times for FFT computations at significantly lower computational cost.

The model can also be used for multiple acoustic computations at different observer locations without re-running high-fidelity computations. An added benefit of this model is that multiple cases can be made and used as input into a more sophisticated neural network architecture for acoustic predictions.

The DMD method is significantly more complicated of the two methods. Because it attempts to reconstruct the time coefficients using an initial guess from the modes, the mode truncation becomes critical in the success of the model. The optimal hard threshold method was first tested with some successes in the primitive variables -pressure and velocity but failed in the time derivatives. Using the mode energy truncation method with a convergence > 99.8% increased the accuracy of the predictions significantly. However, this resulted in a very high number of modes needed for reconstruction.

A look at the spectral performance showed that it is only capable of reconstructing and predicting the tonal content, but completely misses out on the broadband. This is in part due to the algorithm not being able to resolve fluctuations in the data evident in Figure 3-9. For frameworks requiring only tonal predictions, this model would work great, and can be used for forecasting of data, which may be useful for active control applications.

Subsequently, there is a need to investigate more novel DMD approaches such as the extended DMD[102], and the forward-backward DMD [103], with some extensions to account for control systems[104]. Additionally, extensions to the POD method can be investigated for extrapolation of the data such as the Krylov-based POD [105]. These approaches show promise of a reduced order model based acoustic prediction system that could result in faster turnaround time for design.

4 Active Multi-Rotor Noise Control

Rotor noise reduction techniques can be classified into passive or active noise control. Passive technologies include, for example, blade sweep to reduce tip speeds [47], leading/trailing edge serrations [106], blade count, [48] etc. While these technologies help in reducing noise, there is usually a penalty on performance. Active Noise Control (ANC) is an alternative approach that differs from the passive techniques, in that it is engaged only when needed. Since AAMV noise may be particularly critical as it approaches the target observer, or during take-off and landing, ANC may be an appropriate technology, which we will explore here.

AAMV noise is characterized by tonal and BBN. At low frequencies the tonal noise is larger than the BBN, but at medium to high frequency the BBN dominates [12]. As such both types of noise need to be suppressed. Additionally, at typical tip Mach Numbers greater than 0.65, thickness noise begins to be very significant. We start here by focusing on the in-plane thickness noise, since it is deterministic, and as such a deterministic control system can be designed. Prior work on ANC was focused on a single rotor control using a point actuator. However, for AAMV we need an ANC for multirotor systems. Therefore, we present here a new approach, which builds on the previous work, focused on AAMV with their characteristics multi-rotors and operating conditions and geometry.

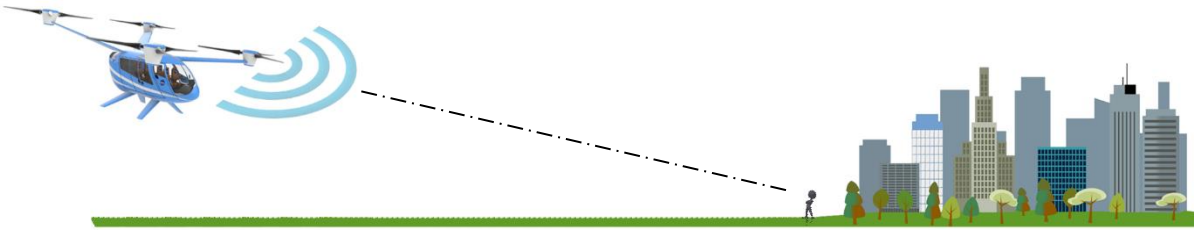

Figure 4-1 Typical eVTOL configuration showing direction of community noise.

The outline of this section is as follows. First, we provide the formulation and results to achieve complete cancellation of two rotor noise for a single point observation. This is then extended into noise reduction over a zone of silence. AAMV rotors are usually smaller than those of helicopters. As such, single point actuation may not be practical, and we explore novel technique using an embedded array of micro actuators instead. We explore the use of piezo speakers as an actuator.

4.1 Geometry & Thickness Noise formulation

4.1.1 Geometry

We consider here the case of two inline rotors, with two blades each, in forward flight with the objective of determining a loading signal created by a point actuator embedded on each blade. We focus on the in-plane thickness noise, and we use FWH to determine the appropriate actuation signal as was done earlier by Gopalan & Schmitz [107] and Yang et al [66] for the case of a single-bladed single rotor. Before this actuation signal is determined, computation of the in-plane thickness noise itself is needed for the 2-bladed two inline rotors.

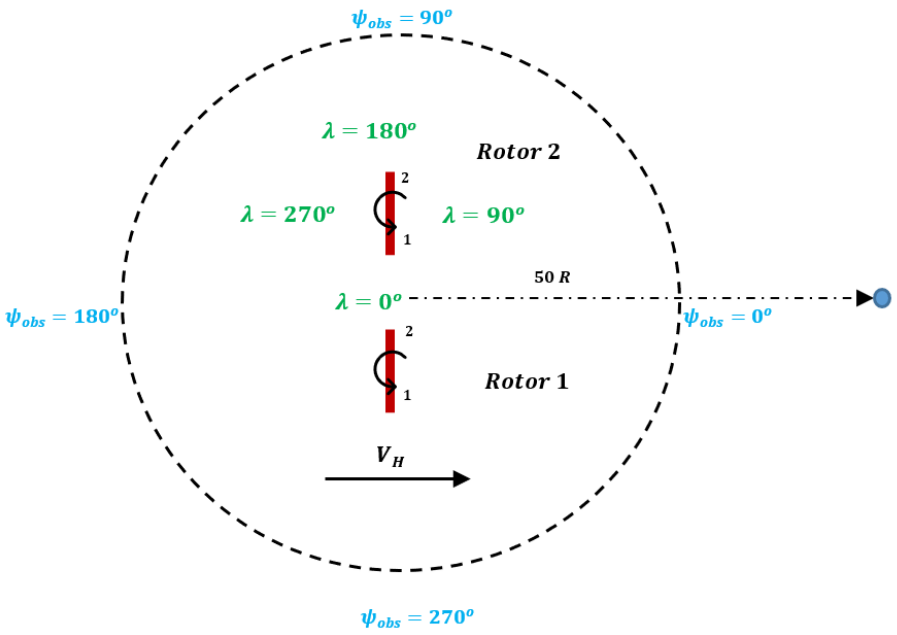

Figure 4-2 Schematic of Two rotors case.

4.1.2 Thickness Noise Formulation for Multi-Rotor Systems.

As our focus is on multi-rotor noise, we develop our own code to predict thickness noise based on the FWH Formulation 1A equations[80]. This will enable us to extract integrand terms for further analysis. The blade geometry is developed in OpenVSP, and exported to MATLAB, where the FWH equations are utilized for far-field thickness noise prediction:

$$4\pi p_T'(x,t) = \sum_{nB*nR} \left\{ \int_{f=0} \left[\frac{\rho_o(\dot{U}_n + U_{\dot{n}})}{r(1-M_r)^2} \right]_{ret} dS + \int_{f=0} \left[\frac{\rho_o U_n (rM_r + c(\dot{M}_r - M^2))}{r^2(1-M_r)^3} \right]_{ret} dS \right\} \quad (4.1)$$

Where nB is number of blades per rotor, and nR is the number of rotors.

Two main algorithms exist for this formulation[108],

- Retarded time formulation requires selecting an observer time range and iterating at each blade position to satisfy the retarded time equation, $t = \tau + \frac{r}{c}$. This was seen to be computationally expensive[108] and thus was not used.

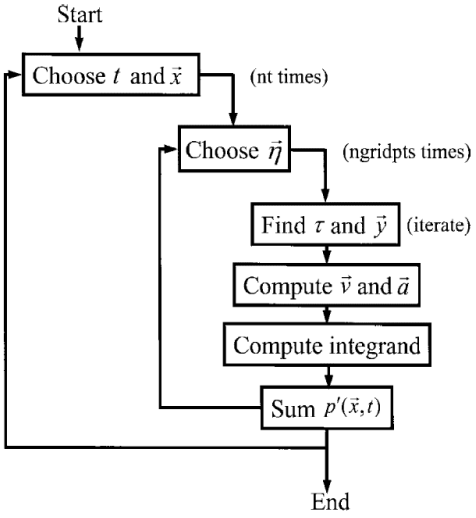

Figure 4-3 Schematic of Retarded-time algorithm [108]

- Source time-dominant algorithm, where we choose a source time range, which is easy, and each point is already in source time domain, thus requires only one blade transformation (rotation) after which a corresponding observer time is computed and

then interpolated before summing the contribution from each source on the blade at the observer point.

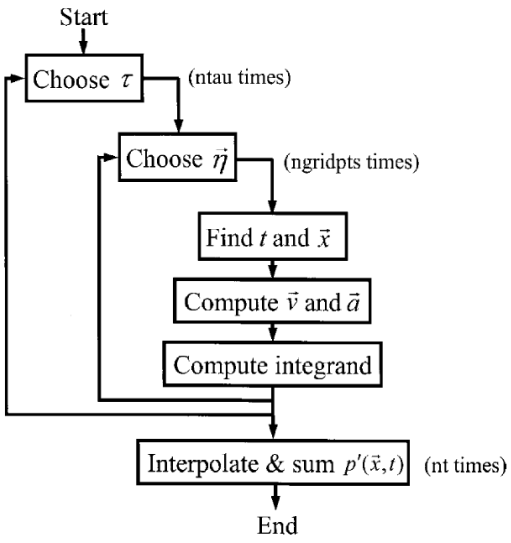

Figure 4-4 Schematic of source-time dominant algorithm[108]

This is what is used in WOPWOP code [109], and what is implemented here. First, a source time, (τ) is specified and the blade geometry is loaded. The observer location is also specified in $\vec{x}(t)$. Based on the RPM, the time for one complete revolution is calculated. The blade is discretized into chordwise and spanwise stations and is split into upper and lower surfaces.

The blade motion of each point on the blade surface is described using the transformation matrix. Given each point on the blade as $\vec{y}_i(\tau)$, the blade rotation or the point rotation at the next point in the blade azimuth is given as $\vec{y}_{i+1}(\tau) = [T]\,\vec{y}_i(\tau)$, where $[T]$is the rotational matrix:

$$[T] = \begin{bmatrix} cos\psi & -sin\psi & 0 \\ sin\psi & cos\psi & 0 \\ 0 & 0 & 1 \end{bmatrix} \tag{4.2}$$

With the blade in the blade-fixed frame of reference, that is in static or original position, a point in this state, $\vec{\eta}(\tau) = \begin{pmatrix} x \\ y \\ z \end{pmatrix}$;

$$\vec{\eta}_{i+1}(\tau) = [T_i]\vec{\eta}(\tau) + \eta_{Forward} \tag{4.3}$$

$$[T_i] = \begin{bmatrix} \cos(\psi i) & -\sin(\psi i) & 0 \\ \sin(\psi i) & \cos(\psi i) & 0 \\ 0 & 0 & 1 \end{bmatrix} \tag{4.4}$$

where ψ is the azimuthal increments of the blade rotation in radians, $\eta_{Forward}$ are translational position computed as $\vec{V}_\infty * d\tau$. The surface normal vectors are also computed as $\vec{n}(\tau) = \begin{pmatrix} \hat{u} \\ \hat{v} \\ \hat{w} \end{pmatrix}$. The variation of the new surface normal for each blade-fixed frame is also given as:

$$\vec{n}_{i+1}(\tau) = [T_i]\vec{n}(\tau) \tag{4.5}$$

The derivative of the surface normal with respect to time, $\dot{n}$ is then computed as:

$$\dot{\vec{n}}_{i+1}(\tau) = [S_i(\omega)][T_i]\vec{n}(\tau) \tag{4.6}$$

$[S_i]$ is the skew symmetric matrix for the rotation, and is computed also as:

$$[S_i(\omega)] = [T_i]^T * [\dot{T_i}] \tag{4.7}$$

$$[\dot{T_i}] = \omega * \begin{bmatrix} -\sin(\psi i) & -\cos(\psi i) & 0 \\ \cos(\psi i) & -\sin(\psi i) & 0 \\ 0 & 0 & 0 \end{bmatrix} \tag{4.8}$$

The corresponding velocity and acceleration are then computed as:

$$\vec{v}(\vec{\eta}, \tau) = \left[\overrightarrow{V_\infty}\right] + [S_i(\omega)][T_i]\vec{\eta}(\tau) = U; \tag{4.9}$$

$$[\dot{T_i}] = \Omega * \begin{bmatrix} -\sin(\psi i) & -\cos(\psi i) & 0 \\ \cos(\psi i) & -\sin(\psi i) & 0 \\ 0 & 0 & 0 \end{bmatrix} \tag{4.10}$$

The distance from each point on the blades' surfaces to the observer is calculated using the relation:

$$r = |\vec{x} - \vec{y}| = \sqrt{(x_1 - y_1)^2 + (x_2 - y_2)^2 + (x_3 - y_3)^2} \tag{4.11}$$

$$\hat{r_i} = \frac{(\vec{x} - \vec{y})}{r} \tag{4.12}$$

Where $\vec{x}$ are the source coordinates, and $\vec{y}$ are the observer coordinates.

After these are computed, the integrands are calculated, and the observer times are calculated for each individual point using $t = \tau + \frac{r}{c}$, where τ is the source time. This is done because each point on the blade emits an acoustic pressure that arrives at different times for the specified observer. Since the pressure emission from each source reaches the observer at a different time, we interpolate the values onto a fixed desired observer time range.

Now that all the source contributions are on the same scale (accounting for the times they all arrive at the observer location), we then sum them up to get the total thickness pressure value for that blade sections over the time range. This cycle is repeated for all the other blade sections and summed first for the upper and lower surfaces individually, then integrated again to obtain the far-field location thickness pressure. The entire procedure described uses the source-time dominant algorithm discussed by Brentner et al[110]. A linear superposition is utilized to sum up the effects of each blade and each rotor for a given observer location. With focus on the thickness noise, we notice the interaction effects due to the varying arrival times of the noise at the observer are pronounced as either overlapping or shifted peaks.

To validate our thickness noise solver, we use the $1/7^{th}$ scale UH-1H model rotor, which is an untwisted blade with NACA 0012 airfoil section. The rotor radius is 1.045m, and a chord of 0.0762m, giving an aspect ratio of 13.7. The observer location is placed at 3.09 Radii away in the rotor plane. A hover tip Mach number, $M_H = 0.88$ is used. We set $nB = nR = 1$ for this test case. Results are compared with experimental data by Purcell [111] in Figure 4-5.

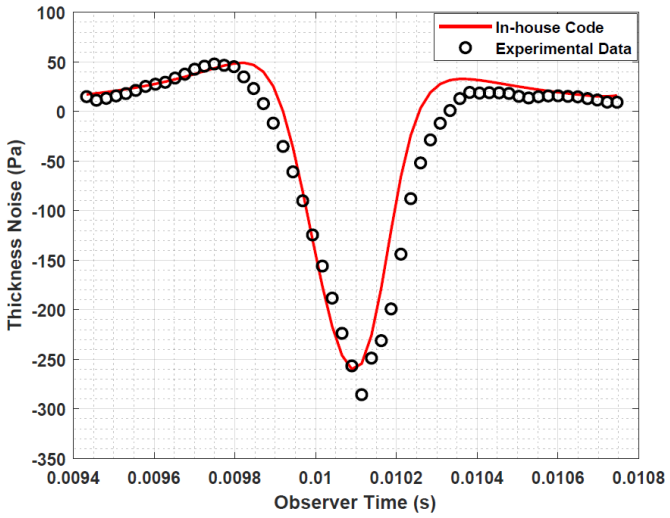

Figure 4-5 Thickness Noise Acoustic Pressure for UH-1H Model Rotor [111].

To investigate the relevance of in-plane thickness noise in a typical eVTOL rotor configuration, we plot out the thickness noise (Figure 4-6) for the same rotor, UH-1H with two blades at a tip Mach number M_T =0.40, with an advancing tip Mach number M_{AT}=0.66, and advance ratio, $\mu = 0.40$. The observer is located at 50 Radii away. The results show that at these relatively lower tip speeds, the thickness noise is far larger than the steady loading noise in the in-plane direction. Unsteady loading noise, however, is not modeled here. Future extensions of this approach would investigate the effects of unsteady blade loads.

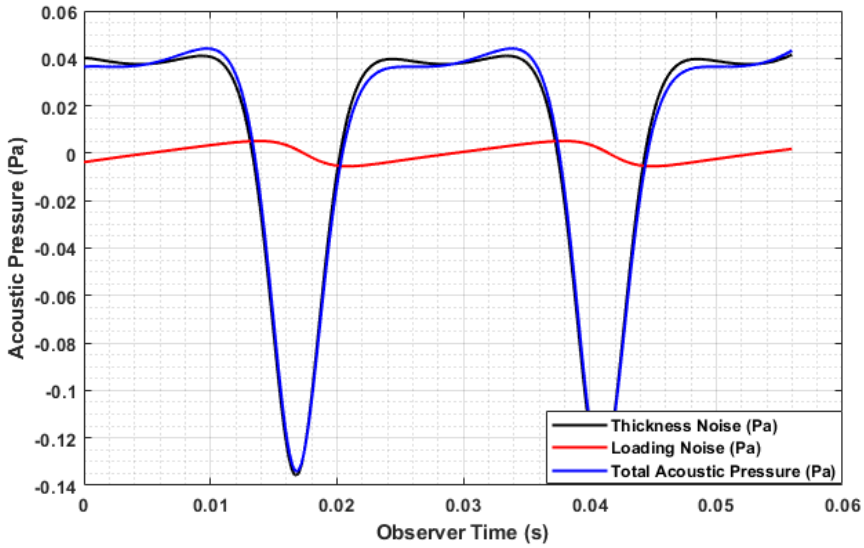

Figure 4-6 Acoustic Pressure, M_{AT}=0.66 showing relevance of thickness noise.

4.2 Formulation & Noise Reduction at a Single target Observer.

With the validation of the thickness noise prediction satisfied, we move on to develop formulations for the loading solutions needed to nullify the far-field thickness noise.

4.2.1 Formulation

From the Formulation 1A [112], the total acoustic pressure at an observer point is given as:

$$p'(x,t) = p'_T(x,t) + p'_L(x,t) \tag{4.13}$$

Where $4\pi p'_T(x,t)$ is given in Eq. (4.1), and

$$4\pi p'_L(x,t) = \sum_{nB*nR} \left\{ \frac{1}{c_o} \int_{f=0} \left[\frac{\dot{L}_r}{r(1-M_r)^2} \right]_{ret} dS + \int_{f=0} \left[\frac{L_r - L_M}{r^2(1-M_r)^2} \right]_{ret} dS \right. \\ \left. + \frac{1}{c_o} \int_{f=0} \left[\frac{L_r((r\dot{M}_r + c_o(M_r - M^2))}{r^2(1-M_r)^3} \right]_{ret} dS \right\} \tag{4.14}$$

To find the loading solution, we set $\sum p'_{L_i}(x,t) = -p'_T(x,t)$. If we assume the blade surface to be a compact source, the loading noise formulation becomes:

$$p'_{L_{Anti}}(x,t) = \frac{1}{4\pi c_o}\sum_{i=1}^{nB*nR}\left[\frac{1}{r_i(1-M_{r_i})^2}\frac{\partial L_{r_i}}{\partial \tau} + \frac{c_o L_{r_i}}{r_i^2(1-M_{r_i})} + \frac{L_{r_i}\left(r_i\dot{M_{ri}} + c_o M_{r_i} - c_o M^2\right)}{r^2(1-M_{r_i})^3}\right]_{ret} \tag{4.15}$$

Here L_r is the component of the loading solution in the radiation direction, nB & nR are the number of blades and number of rotors respectively. The loading equation can then be reconstructed into an ODE:

$$\frac{dL_{r_i}}{d\tau} + p(\tau)L_{r_i} = r(\tau) \tag{4.16}$$

Where:

$$p(\tau) = \sum_{i=1}^{nB*nR}\left[\frac{c_0\left(1-M_{r_i}\right)^2 + r_i\dot{M}_{r_i} + c_0\left(M_{r_i} - M^2\right)}{r_i\left(1-M_{r_i}\right)}\right] \tag{4.17}$$

$$r(\tau) = -4\pi c_0\, {p_T}'/_{\varepsilon}\sum_{i=1}^{nB*nR} r_i\left(1-M_{r_i}\right)^2 \tag{4.18}$$

The above ODE is solved for L_{r_i}, and then sum them over the number of blades to obtain the total noise control. The ODE is periodic at about 2π for an initial condition:

$$\xi = L_r(0) = \frac{L_{r_h}(2\pi)\int_0^{2\pi} r(s)/L_{r_h}(s)ds}{1 - L_{r_h}(2\pi)} \tag{4.19}$$

L_{r_h} is the solution of the homogeneous ODE, with $L_{r_h}(\tau) = e^{-\frac{c_0}{r}\tau}$. Analytically, the solution of this heterogeneous ODE is of the form:

$$L_r(\tau) = e^{-p(\tau)\tau}\left(\int e^{p(\tau)\tau} r(\tau)d\tau + C_1\right) \tag{4.20}$$

After obtaining the initial loading solution, $L_{r_i}(\tau)$, Eq. (4.15) is then solved by feeding the values of the thickness noise, p'_T, and getting values of r, M_r, and M from the computation of the

thickness noise. Here, ε is the weighting for the anti-noise strength per actuator. For equal contributions, $\varepsilon = nB * nR$. A fourth order Runge-Kutta algorithm is employed to solve for the loading "anti-noise" solution, which is then fed into Eq. (4.15) to find the corresponding anti-noise pressure signal.

4.2.2 Reduction at a single target observer

For all subsequent results, we utilize the 1/7th scale UH-1H rotor as indicated earlier, with a span of 1.045m, typical of most eVTOL rotors. We duplicate the blade count to two blades, and the rotor count to 2 rotors as shown in Figure 4-2. A tip Mach number M_T =0.40 is utilized, with an advancing tip Mach number M_{AT}=0.66, and advance ratio, $\mu = 0.40$. The observer location is set at 50 radii away from the rotor hub, in the rotor plane at $\psi_{obs} = 0^o$, and $\lambda = 90^o$, where λ is the angle in the blade reference frame (See Figure 4-2). The control point is placed at 0.9R, and 0.5 chord. We apply the formulations to that of a multi-rotor system. We utilize two rotors separated by 1 meter. Here, we set $nB = nR = 2$.

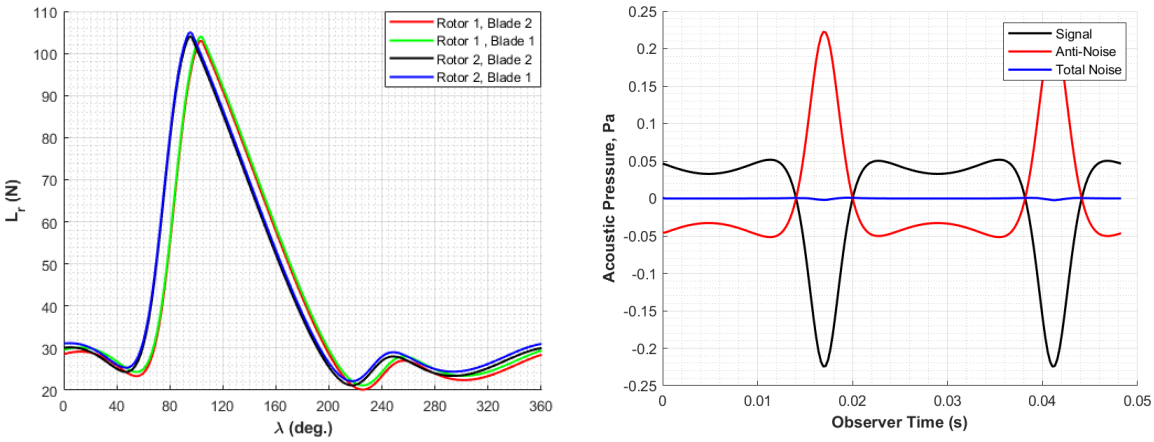

(a) (b)

Figure 4-7 Loading Solution (L_r) for all 4 blades, (b): Total Thickness noise at target observer.

Figure 4-7 shows the loading solutions for all 4 actuators, and their corresponding anti-noise pressures. We see similar loading distributions across the blades. The subtle differences are

attributed to the relative positions of the rotors from the center of the two rotors, and the variation in radiation direction, *r* about the rotor azimuth. Also, we note that the blade azimuth is offset from the observer azimuth by ~90^{o}, and the center of rotation of each rotor differs from that of the observer azimuth. As the observer location decreases, the relative difference between the blade reference frame and that of the observer frame increases. A plot of the near- & far-field instantaneous acoustic pressure contours in the x-z or horizontal plane (See Figure 4-8) is shown in Figure 4-9.

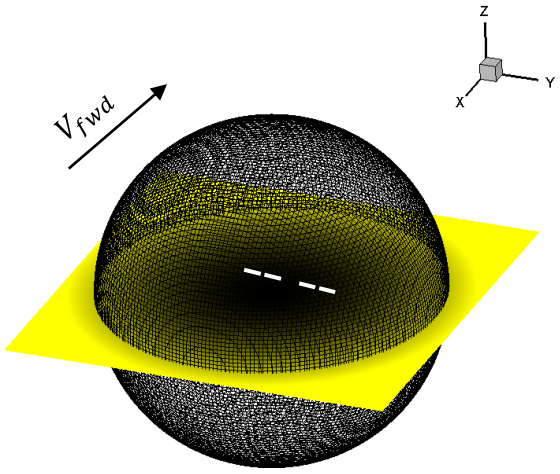

Figure 4-8 Schematic showing sphere of observer locations and slice at Z=0.

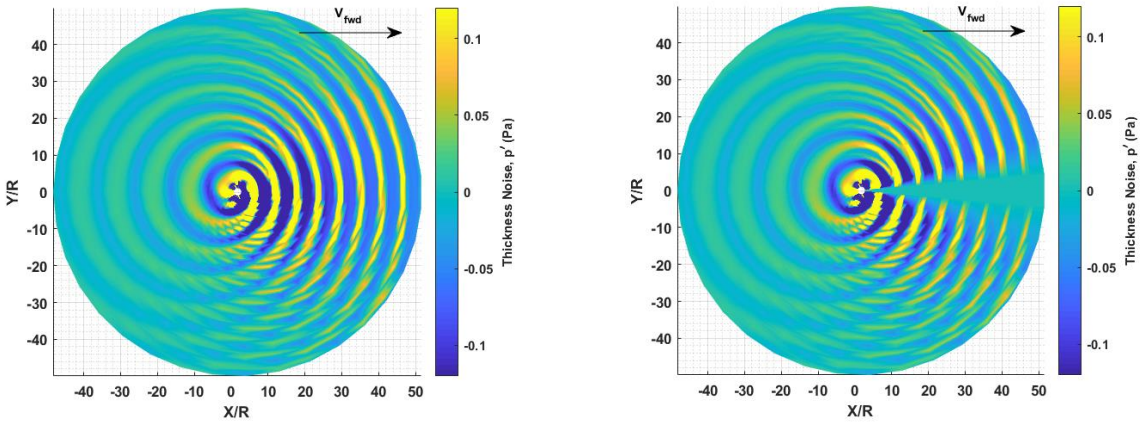

(a) (b)

Figure 4-9 Contour plots of acoustic pressure showing (a): No control, and (b): With control for a single observer at $\psi_{obs} = 0^o$

4.3 Formulation & Noise reduction over an azimuthal range of target observers

In practical applications, the need arises for noise reduction over a zone of observers rather than a single-point observer. As such, we extend our formulations introduced in section 2 above using an optimizer, to cover an azimuthal zone of observers. This concept is similar to that of Yang et. al [66] but is extended to two inline rotors (Figure 4-10), and one actuator per blade.

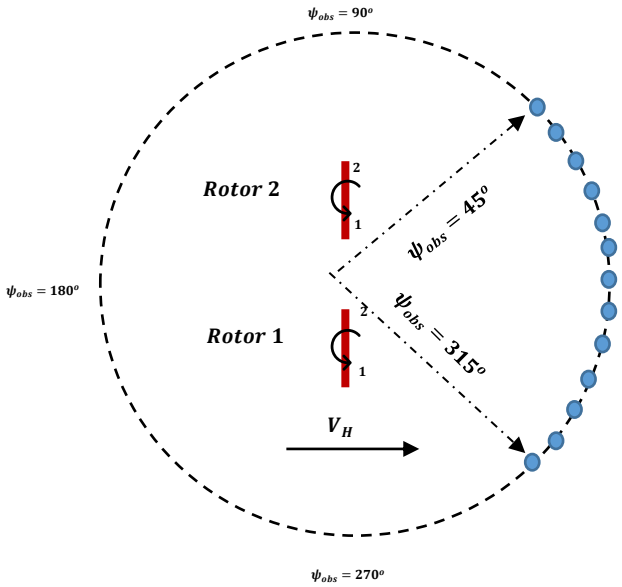

Figure 4-10 Schematic showing range of target observers in the rotor azimuth.

4.3.1 Zone Formulation

First, the loading solution in its current form, would not work for multiple observers as it is dependent on the individual observer position, that is $L_r = \vec{L} \cdot \hat{r}$, where $\hat{r}$ is the unit radiation direction from source to the observer. Instead, we need to find a loading solution, that would be optimized to reduce the noise in a range of observers in the rotor azimuth (in-plane). To do this, we introduce a new loading term, L_{rA}, such that:

$$L_{rA} = \sum_{i=1}^{nObs*nB*nR} K_i L_{r_i} \tag{4.21}$$

Where L_{r_i} is the individual loading solutions for the specific observer location, K_i is the coefficients that needs to be solved, and $nObs$ is the number of observers. To account for the relative positions of the actuators we define the loading vector $\overrightarrow{L_i}$ as a combination of span-wise and chord-wise forces such that:

$$\overrightarrow{L_{r_i}} = \begin{bmatrix} F_c \\ -F_s \end{bmatrix} \cdot r_i = \begin{bmatrix} F_c \\ -F_s \end{bmatrix} \cdot \begin{bmatrix} sin\,(\psi_{obs} - (nB-1)*\pi - \lambda\,) \\ cos\,(\psi_{obs} - (nB-1)*\pi - \lambda\,) \end{bmatrix} \tag{4.22}$$

To solve for the coefficients, we set up a "fitness" function, *f:*

$$f = \sum_{i=1}^{nObs} \left\{ p_{T_i'} + \frac{1}{4\pi c_0} \left[\frac{1}{r_i(1-M_{r_i})^2} \frac{\partial L_{rA}}{\partial \tau} + \frac{c_o L_{rA}}{r_i^2(1-M_{r_i})} + \frac{L_{rA}\left(r_i \dot{M}_{r_i} + c_o M_{r_i} - c_o M_i^2\right)}{r_i^2(1-M_{r_i})^3} \right]_{\text{ret}} \right\} \tag{4.23}$$

This equation is then solved using a genetic algorithm with a goal to drive the function, *f* to a minimum. For subsequent computations, we elect a target observer range $\psi_{obs} = 315^o - 45^o$.

4.3.2 Reduction at a zone of observers

We show the results for the model 2-bladed multi-rotor (UH-1H). Here, we optimize four actuators – that is one actuator per blade. By optimizing the loading solution that is needed to reduce the noise in the target area, the loading solution obtained is shown in Figure 4-11. We plot out the optimized loading solutions of each blade rotated to the initial blade position corresponding to $\lambda = 0^o$. For $\psi_{obs} = 315^o$ to 45^o , the corresponding range for the blade frame of reference would be $\lambda = 45^o$ to 135^o. Additionally because of the relative positions of the rotors, referring to Figure 4-10, Rotor 1 is closer to $\psi_{obs} = 315^o$ and hence has a stronger actuation strength in the initial regions, whereas Rotor 2 is closer to $\psi_{obs} = 45^o$ and hence activates more strongly in the later regions.

Looking at the optimized loading solution in Figure 4-11, we can see that the larger amplitude region is slightly larger. This is because the loading solution needs to be able to actuate over a broader range. We can speculate that the larger the target area about the rotor azimuth, the longer the actuation period would be. We can also notice that, unlike the single observer case, the anti-noise actuator is not as effective in complete cancellation of the total thickness noise at the given observer, rather, the "optimal" solution is found such that there is the most reduction in all observers in the desired range, and thus some penalties are accrued.

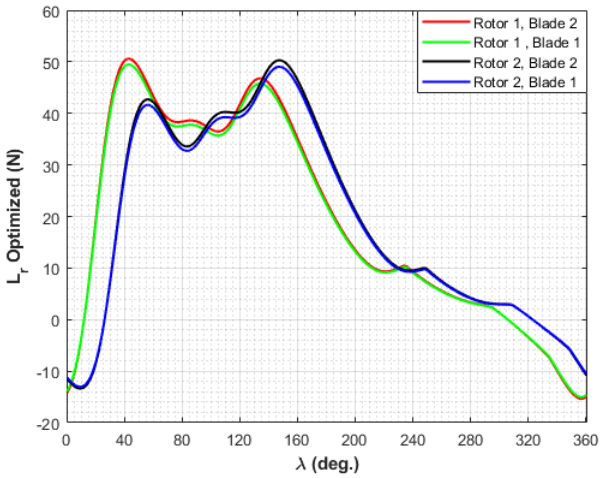

Figure 4-11 Optimized Loading Solutions, L_r for each blade.

For a more meaningful representation of the loading, we plot out the spanwise (F_s), and the chordwise (F_c) loads computed from Eq. (4.22), in Figure 4-12. Here, we see a more positive amplitude in the advancing phase for the spanwise loading which mostly corresponds to the target observer zone, and a more oscillatory chordwise loading in the target observer range.

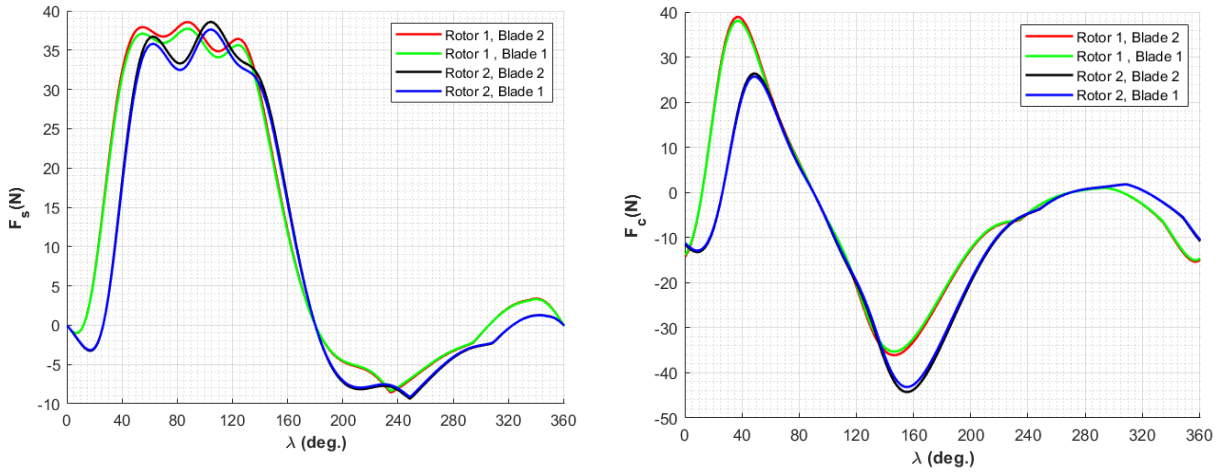

(a) (b)

Figure 4-12 (a) Spanwise Loading (F_s) & (b) Chordwise Loading (F_c).

To verify, again, we compute the total thickness noise at the target region. We again select the observer azimuth ($\psi_{obs} = 0^o$) (see Figure 4-13). There is a reduction of 9dB at $\psi_{obs} = 0^o$, and about 3dB increase at $\psi_{obs} = 180^o$. Additionally, we plot the instantaneous pressure fluctuations in the near field in Figure 4-14.

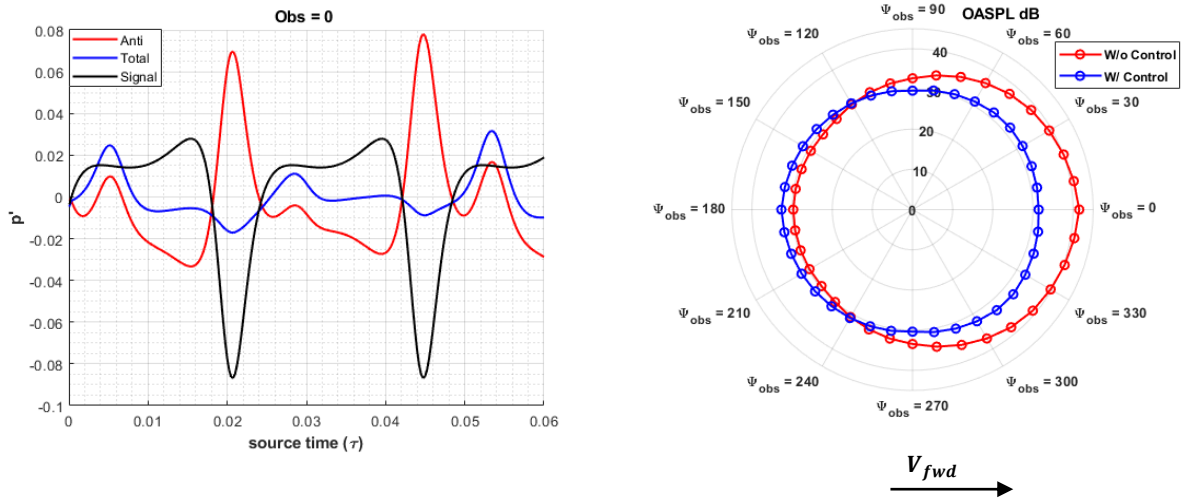

(a) (b)

Figure 4-13 (a): Total Noise at target observer, $\psi_{obs} = 0^o$& (b): OASPL Directivity with and without control.

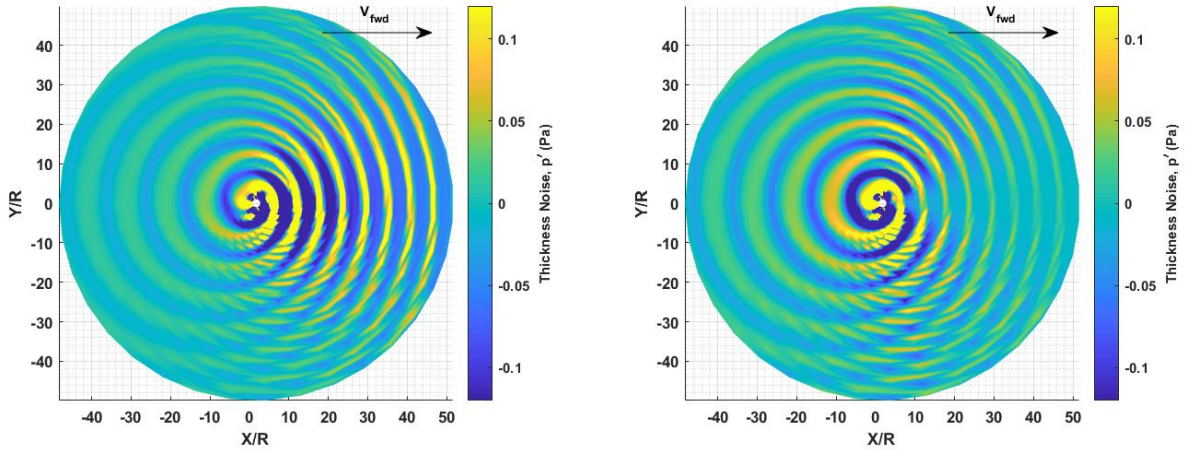

Figure 4-14 Contour plots of acoustic pressure showing (a): No control, and (b): With control for a zone of observers.

Here, we see an optimized anti-noise signal. However, we also see that there is an increase in noise away from the target observer range. This is perhaps due to the fact that there are more tuning parameters for this case – four actuators – which increases the flexibility of the solver to find a better optimal solution. Also, because of the phase shift in the pressure around the rotor azimuth, the peak-to-peak anti-noise signals would not exactly match those away from the target zone and may add to the noise rather than decrease it. It is worth noting that most multi-rotors and even helicopters fly with a downward tilt, and as such, the region away from the target observer range would be pointed upwards away from the general populace (see schematic in Figure 4-1).

4.4 Distributed Array of Actuators Per Blade

The above methodologies have been shown to be quite effective in reducing the in-plane thickness noise. Conventionally, active control of in-plane thickness noise methods has been either cumbersome or present some structural challenges [62] and may affect the aerodynamic performance of the rotors. To remedy this problem, a distributed array of acoustic actuators is

suggested. We assumed a point source formulation [113], however, practically, a piezo speaker with an area of 18 mm x 20 mm and can be as small as 1 mm thickness [114]. This makes embedding these speakers a relatively easier option. Additionally, the placement of these could potentially be optimized for rotor performance gain by improving sectional lift. A series of actuators reduces the load per actuator needed for total cancellation. As such, a series of actuators per blade is proposed to reduce the acoustic radiation power required per actuator.

4.4.1 Formulation for a Single target observer

We now augment our formulations to account for a series of actuators ($nAct$) on the blade. This is like the null approach discussed by Gopalan & Schmitz [107], where they discuss multiple mechanical actuators (fluidic injectors) on the blade but was not feasible due to the practicality of it. For the smaller eVTOL rotor, the method of acoustic drivers may be feasible. This is because the thickness noise is directly related to the thickness of the blades, as well as the blade tip speeds. This would mean for smaller eVTOL rotors, the acoustic signatures would be less in magnitude, and thus would require a relatively lower anti-noise actuation power for the desired cancellation. The corresponding loading anti-noise solutions become:

$$p'_{L_{anti}}(x,t) = \frac{1}{4\pi c_o}\sum_{k}^{nAct}\left\{\sum_{i=1}^{nR*nB}\left[\frac{1}{r_{i,k}(1-M_{r,k_i})^2}\frac{\partial L_{r_{i,k}}}{\partial \tau} + \frac{c_o L_{r_i,k}}{r_{i,k}^2\left(1-M_{r_{i,k}}\right)} + \frac{L_{r_i}\left(r_{i,k}\dot{M_{ri,k}} + c_o M_{r_{i,k}} - c_o M_k^2\right)}{r_{i,k}^2(1-M_{r_{i,k}})^3}\right]\right\}_{ret} \tag{4.24}$$

With the same ODE being given in Eq. (4.16), where $p(\tau)$ & $r(\tau)$ are now given as:

$$p(\tau) = \sum_{k=1}^{nAct}\sum_{i=1}^{nB*nR}\left[\frac{c_0\left(1-M_{r_{i,k}}\right)^2 + r_{i,k}\dot{M}_{r_{i,k}} + c_0\left(M_{r_{i,k}} - {M_{i,k}}^2\right)}{r_{i,k}\left(1-M_{r_{i,k}}\right)}\right] \tag{4.25}$$

$$r(\tau) = -4\pi c_o \, {p'_T}/{\varepsilon} \sum_{k=1}^{nAct} \sum_{i=1}^{nB*nR} r_{i,k}\left(1 - M_{r_{i,k}}\right)^2 \tag{4.26}$$

This gives a number of tuning parameters, ε, for the contribution of each actuator towards the target observer noise. For more flexibility, the tuning weights can be optimized using a similar optimization technique discussed earlier. We define the objective function, *f*:

$$f = p_{T_i} + \sum_{i=1}^{nAct} \left\{ \frac{1}{4\pi c_0} \left[\frac{1}{r_i(1 - M_{r_i})^2} \frac{\partial L_{ri}}{\partial \tau} + \frac{c_0 K_i L_{ri}}{r_i^2\left(1 - M_{r_i}\right)} + \frac{K_i L_{ri}\left(r_i \dot{M}_{r_i} + c_0 M_{r_i} - c_O M_i^2\right)}{r_i^2 (1 - M_{r_i})^3} \right]_{\text{ret}} \right\} \tag{4.27}$$

Here, we solve the weighting values K_i using the same optimizer discussed earlier. With this approach, we could enforce a condition such that the peak loading per actuator does not exceed a specific value. We test this approach for a two-bladed rotor with four actuators located at r/R of 0.95, 0.75, 0.65, & 0.55, and x/c of 0.95, 0.55, 0.35, and 0.25 respectively. We apply an upper limit of 0.5, and a lower limit of 0.10 to the optimizer to avoid a case where it turns off all but one actuator, which would be a viable solution, but not optimal.

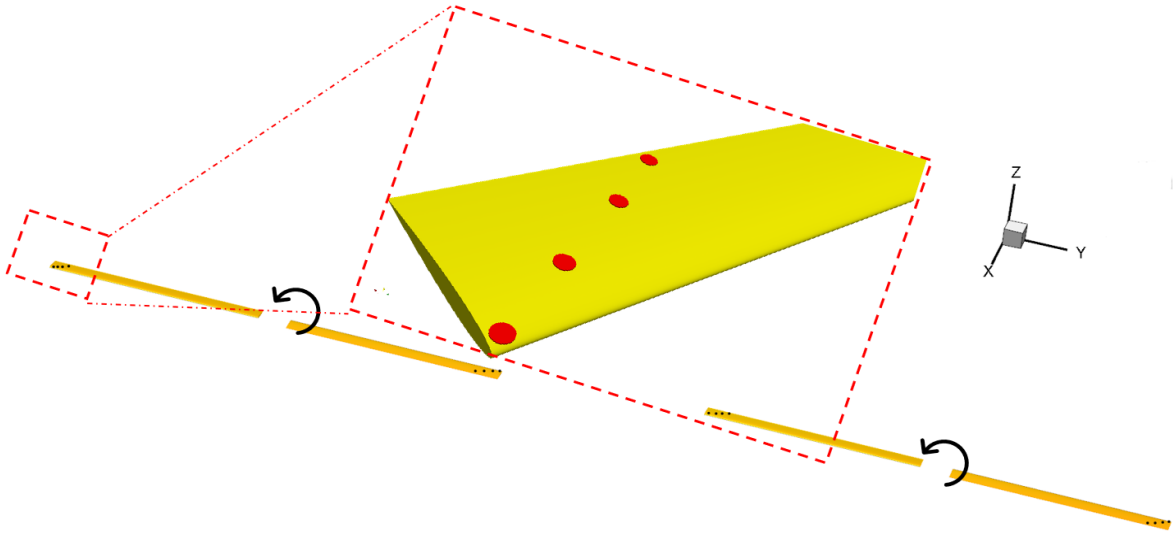

Figure 4-15 Schematic of Placement of piezo speakers (red circles) on rotor blade.

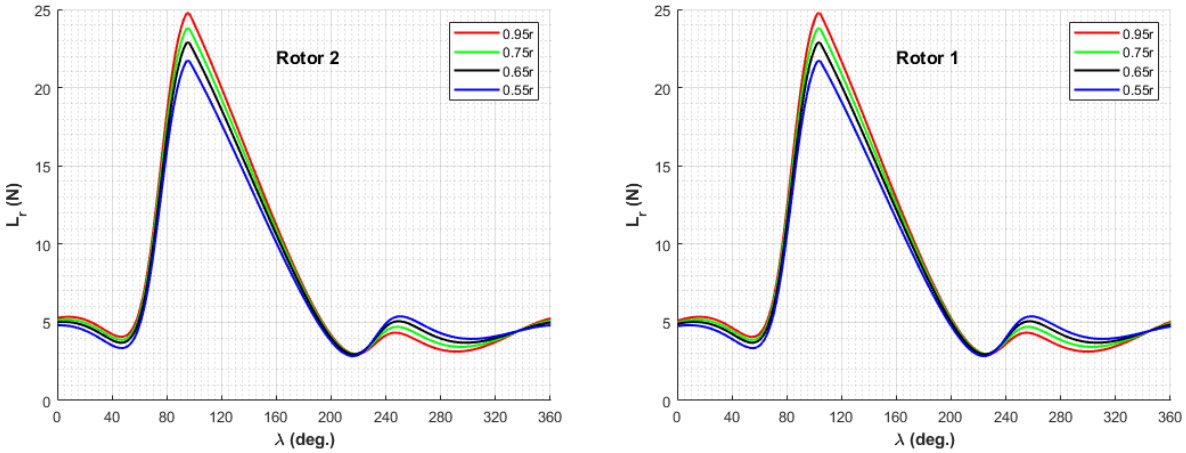

(a)

(b)

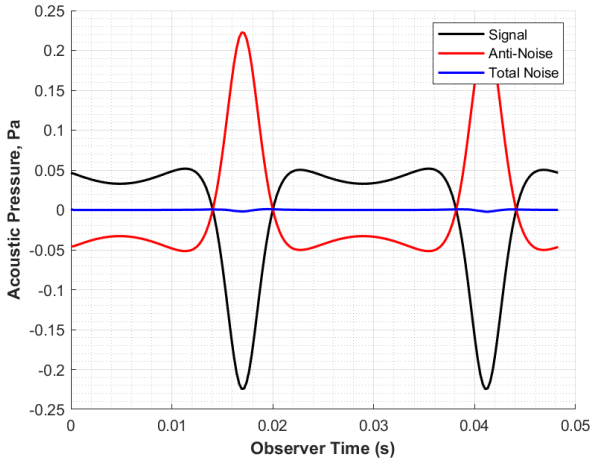

(c)

Figure 4-16 (a & b): Optimized Loading solutions for each actuator, (c): Corresponding Noise at target observer.

Looking at the results in Figure 4-16, we see that the algorithm applied multipliers to the loading solutions, with more actuation power given to position actuator 0.95r. Note that we show here only a single blade per rotor as the results per blade is identical. There is a slight phase difference between Rotor 1 and Rotor 2, again due to the relative positions with respect to the target observer. To validate this result, the sum of the individual loading solutions (shown as Total in Figure 4-16a & b) is obtained and used to compute the corresponding anti-noise signal. The results show, again near-perfect cancellation at the target observer (Figure 4-16c). With the

amplitudes significantly reduced, the acoustic energy needed to achieve the same effect would also be significantly reduced. The size of such a speaker is relatively small, and thus could be incorporated in a blade design without aerodynamic penalties.

4.4.2 Formulation for Target Zone of Observers

Next, we extend the theory to handle a target area, as performed earlier. Here, we need to include an extra tuning term, B_j which would be used to optimize all the actuators for all observers in the target azimuth. The new optimization function, f is given as:

$$f = \sum_{j=1}^{nObs} \left[\left[p_{T_j'} + \sum_{i=1}^{nAct*nB*nR} \left\{ \frac{1}{4\pi c_o} \left[\frac{1}{r_{i,j}(1-M_{r_{i,j}})^2} \frac{\partial L_{ri,j}}{\partial \tau} + \frac{c_o B_j K_i L_{ri,j}}{r_{i,j}^2 (1-M_{r_i})} + \frac{B_j K_i L_{ri,j} \left(r_{i,j} \dot{M}_{r_{i,j}} + c_o M_{r_{i,j}} - c_o M_{i,j}^2 \right)}{r_{i,j}^2 (1-M_{r_{i,j}})^3} \right]_{ret} \right\} \right] \right] \tag{4.28}$$

Such that, the new loading solution per actuator would then be:

$$L_{rA,i,j} = \sum_{j=1}^{nObs*nR*nB} B_j K_i L_{r,j} \tag{4.29}$$

This function is looped over each blade and each rotor, and thus the number of tuning parameters would increase. For a case of 4 actuators per blade, we would have 4**nObs*nB*nR* parameters, where "*nObs*" is the number of observer points in the target area. Again, we utilize the same test case of the two-bladed UH-1H rotor and set the target observer to be in the range of 315^o to 45^o in the rotor azimuthal plane. By tuning a total of 4**10*2 = 80* parameters using the genetic algorithm function in MATLAB, the optimized loading solution per actuator is shown in Figure 4-17. The subsequent span-wise and chord-wise loading are also shown in Figure 4-18.

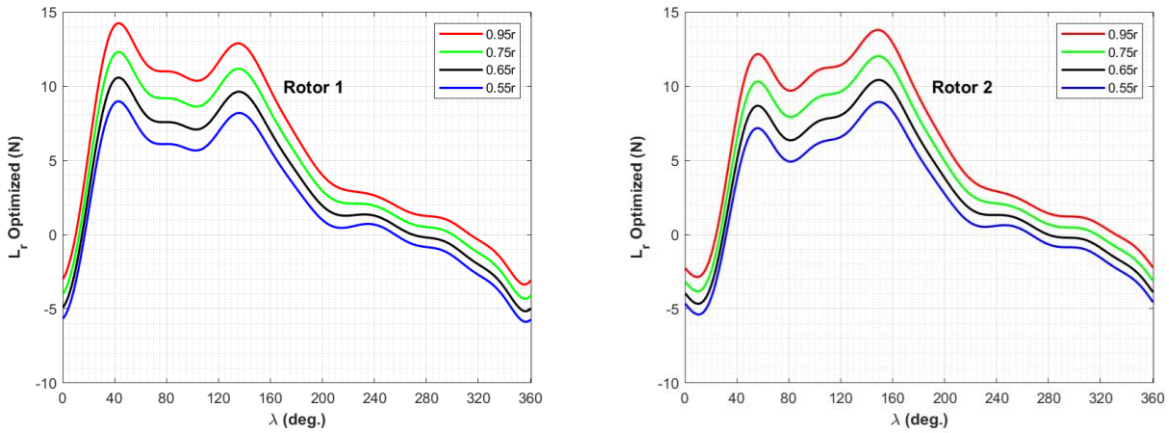

Figure 4-17 Optimized Loading solutions for each actuator per blade.

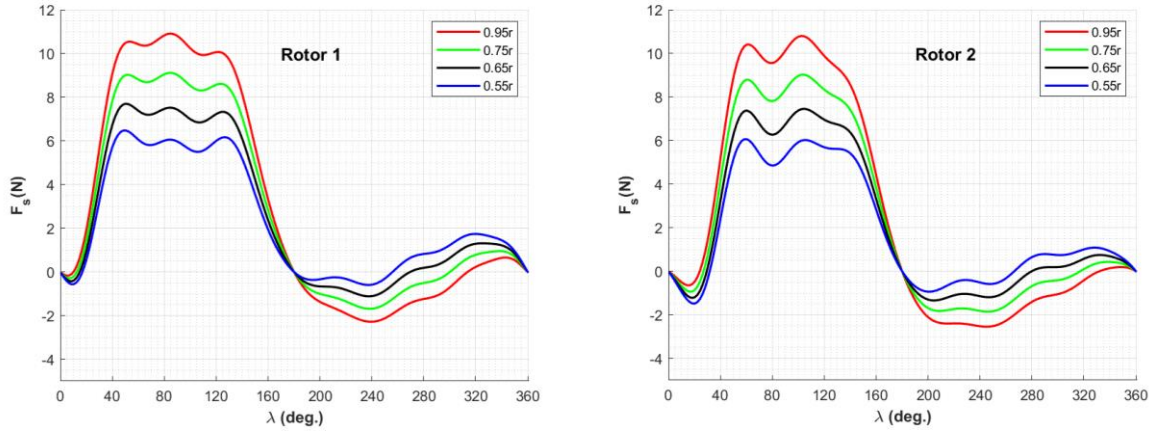

(a) (b)

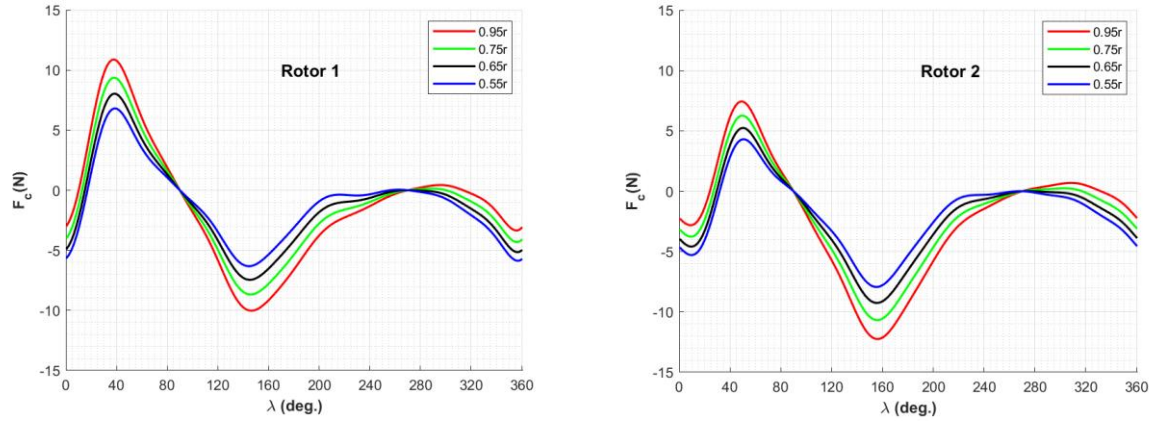

(c) (d)

Figure 4-18 (a), (b): Spanwise Loading (F_s) & (c), (d): Chordwise Loading (F_c).

4.4.3 Directivity of Micro actuators

From a physical perspective, the speaker would be radiating normal to the diaphragm. However, in the formulations, a thickness noise is modeled as monopoles, whereas a loading force is modeled as a dipole. Ideally, we would want a dipole source to radiate in the direction of the observer. Realistically, the speakers are monopolar in nature. To remedy this, we suggest placing two speakers side-by-side with a phase difference to replicate a dipolar volume displacement. Due to the omni-directional nature of the acoustic speakers, there would be comparable acoustic energy in the radiation direction. We compute this acoustic forcing in that direction from L_r (see Figure 4-19).

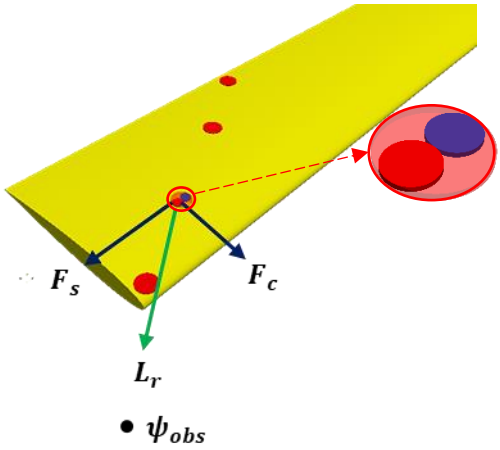

Figure 4-19 Sketch showing the directivity of the forces and the loads in relation to the observer as well as the dual piezo speaker configuration.

To investigate the actuation of the micro-speakers in a dipole source configuration, we take a look at the anti-noise signals shown in Figure 4-18. Focusing on the resultant force in the observer direction, $\boldsymbol{L_r}$, the actuation can be represented by the equation:

$$L_{r_{act}}(\psi) = a_0 + \sum_{i=1}^{8} [a_i \, cos(i\psi) + b_i sin\,(i\psi)] \tag{4.30}$$

This can be split into two formulations for each half of the piezo actuation system such that:

$$L_{r_{act1A}}(\psi) = \frac{a_0}{2} + \sum_{i=1}^{8} [a_i \, cos(i\psi)] \tag{4.31}$$

$$L_{r_{act1B}}(\psi) = \frac{a_0}{2} + \sum_{i=1}^{8} \left[b_i \cos\left(i\psi - \frac{\pi}{2}\right)\right] \tag{4.32}$$

Where a_i & b_i are the amplitudes of the sine and cosine functions of each harmonic frequency of 1-8/rev, and a_0 is a constant. The spanwise and chordwise components can be obtained by multiplying the equations with that of Eq.(4.22) above. We show in Figure 4-20 the chordwise force component for a single actuator at 0.95r.

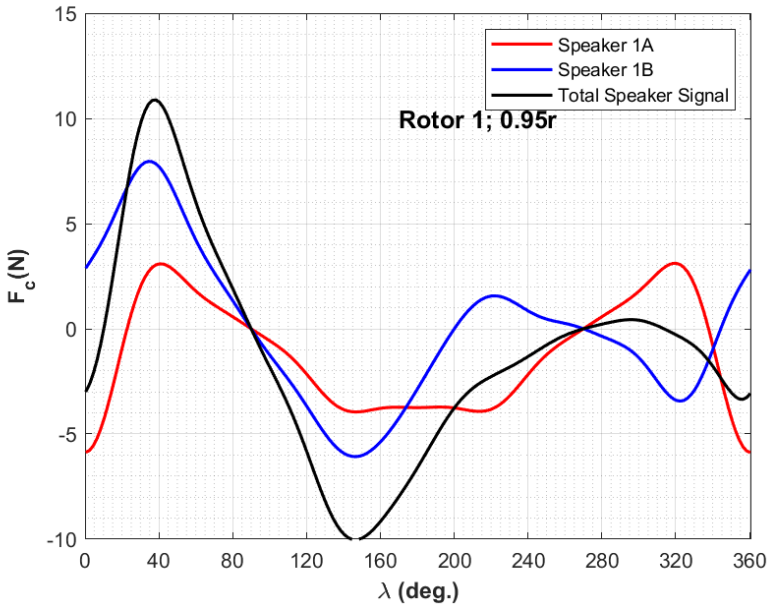

Figure 4-20 Chordwise force component showing dipole split between two adjacent piezo speakers at 0.95r.

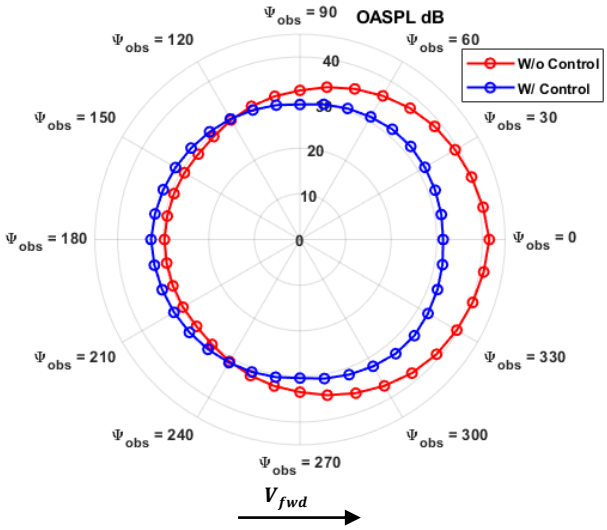

Figure 4-21 OASPL Directivity with and without control.

Again, to prove the validity of the solution, we compute the far-field anti-noise pressure, and plot out the OASPL directivity in Figure 4-21. We see a slightly imperfect total cancellation. This occurs because the loading actuator must account for each observer peak, which is offset, and is not at the same temporal location. For the solver to find the most optimal signal, there would be some peaks in-between the main peaks, and thus would result in reduced main pressure peak, but would also introduce new peaks per observer location, and thus would result in less-than-ideal noise cancellation. The method of distributed loading actuators has been shown here to be a valid approach to reducing the loading magnitudes, while still resulting in similar outcomes as that of the singular actuator.

4.5 Interim Conclusions

An Active Noise Control (ANC) methodology to reduce the thickness noise in multi-rotor systems typical of Advanced Air Mobility Vehicle (AAMV) is developed here.

In the first part of the analysis, we considered the case where a single point actuator is embedded in each blade surface of two rotors in forward flight. There are several interchangeable

choices of such actuators, but we assume here that it is an acoustic signal. We use FWH formulation to determine what loading signal is needed to cancel the total noise at the selected observer point. We were able to achieve complete cancellation at the selected observer point with the analytically computed loading signal. Our solution differs from the previous ones since we are applying the theory to two rotors in forward flight. As a check, our solution reduces to that of Yang et. al (Ref. 13) when the distance between the two rotors is sufficiently large.

For this technology to be useful in real applications, it needs to reduce the noise not at a single point, but over a zone of points as the target area. Therefore, the formulation is extended by applying an optimizer to find a loading solution to handle a target area. By applying this method to a two-bladed multi-rotor system, we see about as much as 9 dB reduction in the target area.

It can be seen that the actuation loading needed to achieve the noise reduction is proportional to the size of the area targeted, and therefore could be large for practical applications. Thus, a new idea is devised to distribute the loads needed for the noise cancellation, with a set of micro speakers embedded in the blade surface. The magnitude or weighting of each of the actuators was optimized using a genetic algorithm such that the total effects of the actuators would cancel the thickness noise at the target area. Thus, we managed to achieve the same noise reduction as that of a single actuator, but now with multiple micro speakers embedded on the blades. Since the actuation needed to create a loading force must be dipole-like in nature, each actuator was formulated as two sub micro speakers' side by side with a phase lag such that the signal is a dipole in nature.

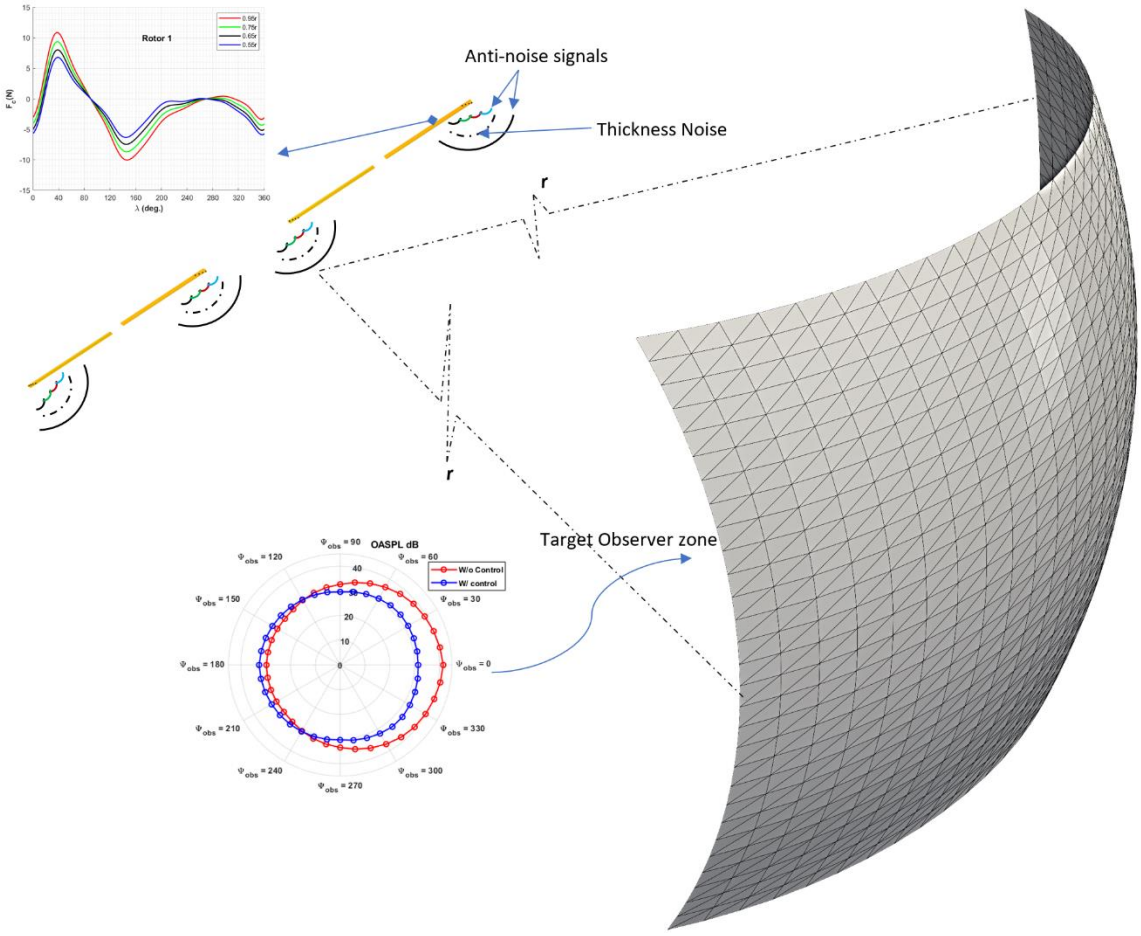

Figure 4-22 Summary schematic of the noise control methodology.

5 Summary and Future Work

This chapter summarizes the key findings for each section and discusses their relevance.

5.1 High-Fidelity Simulation of Multi-rotor Noise

The first part of this research was to investigate the various noise sources for multi-rotor systems. A high-fidelity simulation of two in-line counter-rotating propellers in hover, and in forward flight conditions are performed. Near field flow and acoustic properties were resolved using Hybrid LES-Unsteady RANS. Far-field sound predictions were performed using Ffowcs-Williams-Hawkings formulation. The two-propeller results in hovering are compared with that of the single propeller. This enabled us to identify the aerodynamic changes resulting from the proximity of the two propellers to each other and to understand the mechanisms causing the changes in the radiated sound. We then considered the forward flight case and compared it with the corresponding hovering case. This enabled us to identify the aerodynamic changes resulting from the incoming stream. By examining the near acoustic field, the far-field spectra, the Spectral Proper Orthogonal Decomposition, and by conducting periodic averaging, we were able to identify the sources of the changes to the observed tonal and broadband noise. Some of the key findings were as follows:

- The loading on the blades includes a periodic component, in addition to the classical steady component. This periodic component is produced by the close proximity of the two rotors.
- An intense vortex generation and interaction are observed in the gap between the two rotors. This was also associated with an increase in the turbulence kinetic energy in this region, and an upward jet-like flow, indicating an additional source of BBN.

- The interaction of the two wakes contributes to the broadband noise at the low-frequency range.
- The enhanced pressure fluctuations on the blades are caused by the blade-vortex interactions.
- Specific to forward flight case, the convection effect can partially explain the observed enhancement in the tonal and BBN, but this only amplifies the radiation of the sources, not the sources themselves.
- In addition to the convection-enhancement effect, the blade and wake sources, and the gap flow, the vortical structure of the forward rotor impacts both its blades as well as the wake flow of the aft rotor. This leads to the generation of BBN.
- A sizable separation bubble (deep stall) on the aft rotor blades generates significant BBN due to the instability of the separated shear layer and reattachment.

Overall, a detailed investigation of the noise sources of multi-rotor systems has been presented here, and the insights gained are critical to urban air mobility planning, as some flight conditions might have deleterious acoustic signatures. This deepens our understanding of multi-rotor noise generations and serves as a steppingstone for investigation and development of active noise control techniques.

5.2 Reduced Order Modeling of Rotor Noise

High-Fidelity computations are often used in predicting the tonal and broadband noise of propellers and rotors associated with Advanced Air Mobility Vehicles (AAMV). But LES is both CPU and storage intensive. An investigation of the feasibility of reduction methods such as Proper Orthogonal Decomposition as well as Dynamic Mode decomposition was performed for reduction of data obtained via HLES to be used further to obtain additional parameters. Specifically, we

investigated how accurate reduced models of the high-fidelity computations can be used to predict the far-field noise. It was found that POD was capable of reconstructing accurately the parameters of interest with 15-40% of the total mode energies, whereas the DMD could only reconstruct primitive parameters such as velocity and pressure loosely. A rank truncation convergence criterion > 99.8% was needed for better performance of the DMD algorithm. In the far-field spectra, DMD could only predict the tonal contents in the lower- mid frequencies while the POD could reproduce all frequencies of interest. The limitation of DMD was seen to be a result of the initial value reconstruction approach of the time series. Additionally, the selection of the rank is highly sensitive in the case of the DMD, and as such some extension formulations such as a forward-backward method may be useful.

5.3 Active Rotor Noise Control for Multi-Rotor AAMV

Next, an Active Noise Control (ANC) technology is developed to reduce the in-plane thickness noise associated with multi-rotor Advanced Air Mobility Vehicles (AAMV).

First, we considered the case where a single point actuator is embedded in each blade surface of two rotors in forward flight. We assume here that it is an acoustic signal. The Farassat's 1A formulation is utilized to determine what loading signal is needed to cancel the thickness noise at the selected observer point. We were able to achieve complete cancellation at the selected observer point with the analytically computed loading signal.

Next, the formulations are extended to a zone of target observers. Due to the increased number of tuning parameters, a genetic algorithm is implemented in MATLAB to tackle this problem. A loading solution is obtained such that an overall reduction in the noise is obtained in the target region. By applying this method to a two-bladed multi-rotor system, we see about as much as 9 dB reduction in the target area.

A new idea is then devised to distribute the loads needed for the noise cancellation, with a set of micro speakers embedded in the blade surface. This reduced the amplitude strain on each actuator. Additional extensions to the formulations are devised. The new formulations were shown to perform similar to that of the single actuator per blade approach but with reduced amplitude requirements per actuator per blade. This showed great promise in an approach for active multi-rotor noise control for AAMVs that is actually practical, with relatively lower structural demerits.

5.4 Future Work

Several prongs can be extrapolated from this work. The following are some of the ideas that may need to be further explored:

- Aero-acoustic analysis of multi-rotor systems in ground effects mimicking take-off or landing.
- Effects of gust on AAMV, and the response in blade loading & acoustic radiation
- An analysis of rotor systems in dusty and rainy conditions.
- A high-fidelity computation of an AAMV system with ANC to simulate how efficient our ANC control approach would work under more realistic conditions such as unsteady blade loading, turbulent flow, atmospheric absorption, etc.
- A closed loop feedback controller can also be looked at for the case of the AAMV especially in take-off and landing, where we could measure the noise at a radius near the vehicle, and compute and radiate an anti-noise in real time.
- Additionally, the use of reduced order models and machine learning such as long-short-term modeling (LSTM) or convoluted neural networking to predict the noise to account for the time retardation and lag for the deployment of the anti-noise signal could be an interesting study.

REFERENCES

[1] NASA. Urban Air Mobility. *https://www.nasa.gov/aero/nasa-embraces-urban-air-mobility*. https://www.nasa.gov/aero/nasa-embraces-urban-air-mobility. Accessed Nov. 6, 2021.

[2] Runway Safety | Federal Aviation Administration. https://www.faa.gov/newsroom/runway-safety-0. Accessed May 19, 2022.

[3] Brookhouser, P. E. "Prevention of Noise-Induced Hearing Loss." *Preventive Medicine*, Vol. 23, No. 5, 1994. https://doi.org/10.1006/pmed.1994.1111.

[4] Franssen, E., van Wiechen, C., Nagerlkerke, N., and Lebret, E. "Aircraft Noise around a Large International Airport and Its Impact on General Health and Medication Use." *Occupational and Environmental Medicine*, Vol. 61, No. 5, 2004. https://doi.org/10.1136/oem.2002.005488.

[5] Haines, M., Stansfeld S. A., Job, R., Berglund, B., and Head, J. "Chronic Aircraft Noise Exposure, Stress Responses, Mental Health and Cognitive Performance in School Children." *Psychological Medicine*, Vol. 31, No. 2, 2001. https://doi.org/10.1017/S0033291701003282.

[6] Stansfeld, S., Berglund, B., Clark, C., Lopez-Barrio, I., Fischer, P., Öhrström, E., Haines, M., Head, J., Hygge, S., van Kamp, I., and Berry, B. "Aircraft and Road Traffic Noise and Children's Cognition and Health: A Cross-National Study." *The Lancet*, Vol. 365, No. 9475, 2005. https://doi.org/10.1016/S0140-6736(05)66660-3.

[7] U.S. Department of Transportation (DOT), and Federal Aviation Administration (FAA). Code of Federal Regulation (CFR) - Title 14: Aeronautics and Space - Part

36. Noise Standards: Aircraft Type and Airworthiness Certification - Subpart B: Noise Levels for Transport Category and Jet Airplanes. & Subpart H: Helicopters.

[8] Johnson, W., Silva, C., and Solis, E. *Concept Vehicles for VTOL Air Taxi Operations*. 2018.

[9] Hubbard, H. H. *Aeroacoustics of Flight Vehicles: Theory and Practice Volume 1: Noise Sources*. 1991.

[10] Rizzi, S., Huff, D., Boyd, D. D., Bent, P., Henderson, B., Pascioni, K., Sargent, C. D., Josephson, D., Marsan, M., He, H., and Snider, R. *Urban Air Mobility Noise: Current Practice, Gaps, and Recommendations*. 2020.

[11] Zawodny, N. S., Boyd, D. D., and Burley, C. L. "Acoustic Characterization and Prediction of Representative, Small-Scale Rotary-Wing Unmanned Aircraft System Components." *72nd American Helicopter Society, Paper #4*, 2016.

[12] Mankbadi, R. R., Afari, S. O., and Golubev, V. v. "High-Fidelity Simulations of Noise Generation in a Propeller-Driven Unmanned Aerial Vehicle." *AIAA Journal*, Vol. 59, No. 3, 2021. https://doi.org/10.2514/1.J059117.

[13] Yang, Y., Liu, Y., Li, Y., Arcondoulis, E., and Wang, Y. "Aerodynamic and Aeroacoustic Performance of an Isolated Multicopter Rotor during Forward Flight." *AIAA Journal*, Vol. 58, No. 3, 2020, pp. 1171–1181. https://doi.org/10.2514/1.J058459.

[14] Jia, Z., and Lee, S. Acoustic Analysis of a Quadrotor Evtol Design via High-Fidelity Simulations. 2019.

[15] Casalino, D., van der Velden, W. C. P., and Romani, G. “Community Noise of Urban Air Transportation Vehicles.” *AIAA Scitech Forum*, 2019. https://doi.org/10.2514/6.2019-1834.

[16] Greenwood, E., Brentner, K. S., Rau, R. F., and Ted Gan, Z. F. “Challenges and Opportunities for Low Noise Electric Aircraft.” *International Journal of Aeroacoustics*, Vol. 21, Nos. 5–7, 2022, pp. 315–381. https://doi.org/10.1177/1475472X221107377.

[17] Zhou, T., and Fattah, R. “Tonal Noise Acoustic Interaction Characteristics of Multi-Rotor Vehicles.” *AIAA Aeroacoustics Conference*, Vol. 23, 2017. https://doi.org/10.2514/6.2017-4054.

[18] Shukla, D., and Komerath, N. “Multirotor Drone Aerodynamic Interaction Investigation.” *MDPI - Drones*, Vol. 2, No. 4, 2018, pp. 1–13. https://doi.org/10.3390/drones2040043.

[19] Feight, J. A., Jacob, J. D., and Gaeta, R. J. “Acoustic Characterization of a Multi-Rotor UAS as a First Step towards Noise Reduction.” *AIAA SciTech Forum*, Vol. 55, 2017. https://doi.org/10.2514/6.2017-1174.

[20] Zawodny, N. S., and Pettingill, N. A. “Acoustic Wind Tunnel Measurements of a Quadcopter in Hover and Forward Flight Conditions.” *Inter-Noise*, 2018, pp. 487–500.

[21] Intaratep, N., Alexander, W. N., Devenport, W. J., Grace, S. M., and Dropkin, A. “Experimental Study of Quadcopter Acoustics and Performance at Static Thrust Conditions.” *22nd AIAA/CEAS Aeroacoustics Conference*, 2016. https://doi.org/10.2514/6.2016-2873.

[22] Wang, H., Zang, B., Celik, A., Rezgui, D., and Azarpeyvand, M. “An Experimental Investigation of Propeller Noise in Forward Flow.” *25th AIAA/CEAS Aeroacoustics Conference, 2019,* 2019. https://doi.org/10.2514/6.2019-2620.

[23] Alexander, N., and Whelchel, J. “Flyover Noise of Multi-Rotor SUAS.” *INTER-NOISE and NOISE-CON Congress and Conference Proceedings*, 2019, pp. 2548–2558.

[24] Lee, H., and Lee, D. J. “Rotor Interactional Effects on Aerodynamic and Noise Characteristics of a Small Multirotor Unmanned Aerial Vehicle.” *Physics of Fluids*, Vol. 32, No. 4, 2020. https://doi.org/10.1063/5.0003992.

[25] Diaz, P. V., and Yoon, S. “High-Fidelity Computational Aerodynamics of Multi-Rotor Unmanned Aerial Vehicles.” *AIAA SciTech Forum*, 2018. https://doi.org/10.2514/6.2018-1266.

[26] Cadieux, F., Barad, M., Jensen, J., and Kiris, C. *Predicting Quad Copter Drone Noise*. 2019.

[27] Alvarez, E. J., and Ning, A. “Modeling Multirotor Aerodynamic Interactions through the Vortex Particle Method.” *AIAA Aviation 2019 Forum*, 2019. https://doi.org/10.2514/6.2019-2827.

[28] Nguygen, C., and Kelly, J. “A Users Guide for the NASA ANOPP Propeller Analysis System.” *NASA CR-4768*, 1997.

[29] Rizzi, S. A., Zawodny, N. S., and Pettingill, N. A. “On the Use of Acoustic Wind Tunnel Data for the Simulation of SUAS Flyover Noise.” *25th AIAA/CEAS Aeroacoustics Conference*, 2019. https://doi.org/10.2514/6.2019-2630.

[30] Lumley, J. L. “Coherent Structures in Turbulence.” *Transition and Turbulence*, 1981, pp. 215–242. https://doi.org/10.1016/B978-0-12-493240-1.50017-X.

[31] Berkooz, G., Holmes, P., and Lumley, J. L. “The Proper Orthogonal Decomposition in the Analysis of Turbulent Flows.” *Annual Review of Fluid Mechanics*, Vol. 25, No. 1, 2003, pp. 539–575. https://doi.org/10.1146/ANNUREV.FL.25.010193.002543.

[32] Towne, A., Schmidt, O. T., and Colonius, T. “Spectral Proper Orthogonal Decomposition and Its Relationship to Dynamic Mode Decomposition and Resolvent Analysis.” *Journal of Fluid Mechanics*, Vol. 847, 2018, pp. 821–867. https://doi.org/10.1017/jfm.2018.283.

[33] Peters, N. J., Wissink, A., and Ekaterinaris, J. “A Mode Based Reduced Order Model for Rotorcraft Store Separation.” *AIAA SciTech Forum*, 2022. https://doi.org/10.2514/6.2022-0312.

[34] Schmid, P. J. “Dynamic Mode Decomposition of Numerical and Experimental Data.” *Journal of Fluid Mechanics*, Vol. 656, 2010, pp. 5–28. https://doi.org/10.1017/S0022112010001217.

[35] Cabell, R. H., Kegerise, M. A., Cox, D. E., and Gibbs, G. P. “Experimental Feedback Control of Flow-Induced Cavity Tones.” *AIAA Journal*, Vol. 44, No. 8, 2012, pp. 1807–1815. https://doi.org/10.2514/1.19608.

[36] Brunton, S. L., Rowley, C. W., and Williams, D. R. “Reduced-Order Unsteady Aerodynamic Models at Low Reynolds Numbers.” *Journal of Fluid Mechanics*, Vol. 724, 2013, pp. 203–233. https://doi.org/10.1017/JFM.2013.163.

[37] Rowley, C. W., and Dawson, S. T. M. “Model Reduction for Flow Analysis and Control.” *Annual Review of Fluid Mechanics*, Vol. 49, 2017, pp. 387–417. https://doi.org/10.1146/ANNUREV-FLUID-010816-060042.

[38] Valbuena, M., Sarabia, D., and de Prada, C. “A Reduced-Order Approach of Distributed Parameter Models Using Proper Orthogonal Decomposition.” *Computer Aided Chemical Engineering*, Vol. 29, 2011, pp. 26–30.

[39] Dehghan, M., and Abbaszadeh, M. “A Combination of Proper Orthogonal Decomposition–Discrete Empirical Interpolation Method (POD–DEIM) and Meshless Local RBF-DQ Approach for Prevention of Groundwater Contamination.” *Computers & Mathematics with Applications*, Vol. 75, No. 4, 2018, pp. 1390–1412.

[40] Fic, A., Białecki, R., Transfer, A. K.-N. H., B, P., and 2005, undefined. “Solving Transient Nonlinear Heat Conduction Problems by Proper Orthogonal Decomposition and the Finite-Element Method.” *Taylor & Francis*, Vol. 48, No. 2, 2005, pp. 103–124. https://doi.org/10.1080/10407790590935920.

[41] Wang, Z., Xiao, D., Fang, F., Govindan, R., Pain, C. C., and Guo, Y. “Model Identification of Reduced Order Fluid Dynamics Systems Using Deep Learning.” *Wiley Online Library*, Vol. 86, No. 4, 2017, pp. 255–268. https://doi.org/10.1002/fld.4416.

[42] Brentner, K. S., and Farassat, F. “Helicopter Noise Prediction: The Current Status and Future Direction.” *Journal of Sound and Vibration*, Vol. 170, No. 1, 1994, pp. 79–96. https://doi.org/10.1006/JSVI.1994.1047.

[43] Lu, Z., Debiasi, M., and Khoo, C. “Acoustic Characteristics of a Multi-Rotor MAV and Its Noise Reduction Technology.” *INTER-NOISE and NOISE-CON*, 2016, pp. 393–403.

[44] Bellocq, P., Garmendia, I., Sethi, V., Patin, A., Capodanno, S., and Rodriguez Lucas, F. “Multidisciplinary Assessment of the Control of the Propellers of a Pusher Geared Open Rotor-Part I: Zero-Dimensional Performance Model for Counter-Rotating Propellers.” *Journal of Engineering for Gas Turbines and Power*, Vol. 138, No. 7, 2016. https://doi.org/10.1115/1.4032008/374274.

[45] Tang, Z., Liu, P., Chen, Y., and Guo, H. “Experimental Study of Counter-Rotating Propellers for High-Altitude Airships.” *Journal Of Propulsion and Power*, Vol. 38, No. 6, 2015, pp. 1491–1496. https://doi.org/10.2514/1.B35746.

[46] Diaz, P. V., Rubio, R. C., and Yoon, S. “Simulations of Ducted and Coaxial Rotors for Air Taxi Operations.” *AIAA Aviation 2019 Forum*, 2019. https://doi.org/10.2514/6.2019-2825.

[47] Stoll, A. *Design of Quiet UAV Propellers*. Dissertation. Stanford University, 2012.

[48] Cambray, A., Pang, E., Showkat Ali, S. A., Rezgui, D., and Azarpeyvand, M. “Investigation towards a Better Understanding of Noise Generation from UAV Propellers.” *2018 AIAA/CEAS Aeroacoustics Conference*, 2018. https://doi.org/10.2514/6.2018-3450.

[49] Pascioni, K. A., Rizzi, S. A., and Schiller, N. H. “Noise Reduction Potential of Phase Control for Distributed Propulsion Vehicles.” *AIAA Scitech 2019 Forum*, 2019. https://doi.org/10.2514/6.2019-1069.

[50] Lueg, P. Process of Silencing Sound Oscillations, 2043416, 1936.

[51] Bies, D. A., and Hansen, C. H. “Engineering Noise Control.” 2017, pp. 578–579. https://doi.org/10.1201/9781315273464.

[52] Cunefare, K. “Active Noise Control.” *Special Lay-Language paper for the 75th Anniversary Meeting of the Acoustical Society of America*, 2004.

[53] Ikelheimert, B. J., and Nagel, R. T. “Active Noise Control of an Unducted Model Propeller.” *3rd AIAA/CEAS Aeroacoustics Conference*, 1997, pp. 441–447. https://doi.org/10.2514/6.1997-1639.

[54] Koopmann, G. H., Koopmann, W., and Chen, W. “Active Noise Control to Reduce the Blade Tone Noise of Centrifugal Fans.” *Journal of Vibration, Acoustics, Stress, and Reliability in Design*, Vol. 110, No. 3, 1988, pp. 377–383. https://doi.org/10.1115/1.3269529.

[55] Sargent, D. C. *Active Jet Acoustic Control of Low Frequency, In-Plane Helicopter Harmonic Noise*. PhD Dissertation. University of Maryland, College Park, 2012.

[56] Yu, Y. H., Gmelin, B., Splettstoesser, W., Philippe, J. J., Prieur, J., and Brooks, T. F. “Reduction of Helicopter Blade-Vortex Interaction Noise by Active Rotor Control Technology.” *Progress in Aerospace Sciences*, Vol. 33, Nos. 9–10, 1997, pp. 647–687. https://doi.org/10.1016/S0376-0421(97)00006-7.

[57] Hardin, J. C., and Lamkin, S. L. “Concepts for Reduction of Blade/Vortex Interaction Noise.” *AIAA Journal of Aircraft*, Vol. 24, No. 2, 2012, pp. 120–125. https://doi.org/10.2514/3.45428.

[58] Brooks, T. F., Booth, E. R., Jolly, J. J. R., William, J. R., Yeager, T., Matthew, J. R., and Wilbur, L. “Reduction of Blade-Vortex Interaction Noise through Higher Harmonic Pitch Control.” *Journal of American Helicopter Society*, Vol. 35, 1990.

[59] Splettstoesser, W. R., Lehmann, G., and van der Wall, B. “Higher Harmonic Control of a Helicopter Rotor to Reduce Blade-Vortex Interaction Noise.” *Zeitschrift fur Fluowissenschaften*, Vol. 14, 1966, pp. 109–116.

[60] Anobile, A., Bernardini, G., Gennaretti, M., and Testa, C. “Synthesis of Active Twist Controller for Rotor Blade–Vortex Interaction Noise Alleviation.” *Journal of Aircraft*, Vol. 53, No. 6, 2016, pp. 1865–1874. https://doi.org/10.2514/1.C033330.

[61] Sim, B. W., JanakiRam, R. D., and Lau, B. H. “Reduced In-Plane, Low-Frequency Noise of an Active Flap Rotor.” *Journal of the American Helicopter Society*, Vol. 59, No. 2, 2014. https://doi.org/10.4050/JAHS.59.022002.

[62] Sargent, D. C., and Schmitz, F. H. Fundamental Experimental Studies Supporting Active-Jet Acoustic Control of in-Plane Rotor Harmonic Noise. No. 51, 2014, pp. 434–446.

[63] Caleb Sargent, D., and Schmitz, F. H. “Fundamental Experimental Studies Supporting On-Blade Tip Air Blowing Control of in-Plane Rotor Harmonic Noise.” *18th AIAA/CEAS Aeroacoustics Conference (33rd AIAA Aeroacoustics Conference)*, 2012. https://doi.org/10.2514/6.2012-2140.

[64] Ffowcs Williams, J. E., and Hawkings, D. L. “Sound Generation by Turbulence and Surfaces in Arbitrary Motion.” *Philosophical Transactions of the Royal Society of London. Series A, Mathematical and Physical Sciences*, Vol. 264, No. 1151, 1969. https://doi.org/10.1098/rsta.1969.0031.

[65] Shi, Y., Li, T., He, X., Dong, L., and Xu, G. “Helicopter Rotor Thickness Noise Control Using Unsteady Force Excitation.” *Applied Sciences 2019, Vol. 9, Page 1351*, Vol. 9, No. 7, 2019, p. 1351. https://doi.org/10.3390/APP9071351.

[66] Yang, T., Brentner, K. S., Corle, E., and Schmitz, S. “Study of Active Rotor Control for In-Plane Rotor Noise Reduction.” *Journal of Aircraft*, Vol. 56, No. 1, 2019, pp. 179–190. https://doi.org/10.2514/1.C034873.

[67] Mankbadi, R. R. *Transition, Turbulence, and Noise*. Springer US, Boston, MA, 1994.

[68] SPALART, P., and ALLMARAS, S. A One-Equation Turbulence Model for Aerodynamic Flows. 1992.

[69] Afari, S., and Mankbadi, R. R. “Simulations of Noise Generated by Rotor-Rotor Interactions at Static Conditions.” *AIAA Scitech 2021 Forum*, 2021. https://doi.org/10.2514/6.2021-1986.

[70] Shur, M. L., Strelets, M. K., Travin, A. K., and Spalart, P. R. “Turbulence Modeling in Rotating and Curved Channels: Assessing the Spalart-Shur Correction.” *AIAA Journal*, Vol. 38, No. 5, 2000, pp. 784–792. https://doi.org/10.2514/2.1058.

[71] Spalart, P. R., Jou, W.-H., Strelets, M., and Allmaras, S. R. *Comments on the Feasibility of LES for Wings, and on a Hybrid RANS/LES Approach*. Greyden Press, 1997.

[72] Crank, J., and Nicolson, P. “A Practical Method for Numerical Evaluation of Solutions of Partial Differential Equations of the Heat-Conduction Type.” *Advances in Computational Mathematics*, Vol. 6, No. 1, 1996, pp. 207–226. https://doi.org/10.1007/BF02127704/METRICS.

[73] Poinsot, T. J., and Lelef, S. K. “Boundary Conditions for Direct Simulations of Compressible Viscous Flows.” *Journal of Computational Physics*, Vol. 101, No. 1, 1992, pp. 104–129. https://doi.org/10.1016/0021-9991(92)90046-2.

[74] Wagner, C. A., Hüttl, T., and Sagaut, P. *Large-Eddy Simulation for Acoustics*. Cambridge University Press, New York, 2007.

[75] Israeli, M., and Orszag, S. A. “Approximation of Radiation Boundary Conditions.” *Journal of Computational Physics*, Vol. 41, No. 1, 1981, pp. 115–135. https://doi.org/10.1016/0021-9991(81)90082-6.

[76] Farassat, F., and Myers, M. K. “Extension of Kirchhoff’s Formula to Radiation from Moving Surfaces.” *Journal of Sound and Vibration*, Vol. 123, No. 3, 1988, pp. 451–460. https://doi.org/10.1016/S0022-460X(88)80162-7.

[77] Lyrintzis, A. S. “Review: The Use of Kirchhoff’s Method in Computational Aeroacoustics.” *Journal of Fluids Engineering*, Vol. 116, No. 4, 1994, pp. 665–676. https://doi.org/10.1115/1.2911834.

[78] di Francescantonio, P. “A New Boundary Integral Formulation for The Prediction of Sound Radiation.” *Journal of Sound and Vibration*, Vol. 202, No. 4, 1997, pp. 491–509. https://doi.org/10.1006/JSVI.1996.0843.

[79] Pilon, A. R., and Lyrintzis, A. S. “Integral Methods for Computational Aeroacoustics.” *35th Aerospace Sciences Meeting and Exhibit*, 1997. https://doi.org/10.2514/6.1997-20.

[80] Brentner, K. S., and Farassat, F. “Analytical Comparison of the Acoustic Analogy and Kirchhoff Formulation for Moving Surfaces.” *AIAA Journal*, Vol. 36, No. 8, 1998. https://doi.org/10.2514/2.558.

[81] Epikhin, A., Evdokimov, I., Kraposhin, M., Kalugin, M., and Strijhak, S. "Development of a Dynamic Library for Computational Aeroacoustics Applications Using the OpenFOAM Open-Source Package." *Procedia Computer Science*, Vol. 66, 2015, pp. 150–157. https://doi.org/10.1016/j.procs.2015.11.018.

[82] DJI Phantom III. *https://www.dji.com/ phantom-3-standard*.

[83] Tiger P15x5 Propeller. *https://grabcad.com/library/tiger-motor-15x5-carbon-fiber-propeller-1*.

[84] Mankbadi, R. R., Hixon, R., and Povinelli, L. A. "Very Large Eddy Simulations of Jet Noise." *6th Aeroacoustics Conference and Exhibit*, 2000. https://doi.org/10.2514/6.2000-2008.

[85] Mankbadi, R., Lo, S. C., Lyrintzis, A., Golubev, V., Dewan, Y., and Kurbatskii, K. "Hybrid LES-RANS Simulations of a Jet Impinging on a Flat Plate." *International Journal of Aeroacoustics*, Vol. 15, Nos. 4–5, 2016, pp. 535–553. https://doi.org/10.1177/1475472X16642355.

[86] Russell, C. R., and Sekula, M. K. "Comprehensive Analysis Modeling of Small-Scale UAS Rotors." *AHS International 73rd Annual Forum*, Vol. 73, 2017.

[87] Zhou, W., Ning, Z., Li, H., and Hu, H. "An Experimental Investigation on Rotor-to-Rotor Interactions of Small UAV." *35th AIAA Applied Aerodynamics Conference*, 2017. https://doi.org/10.2514/6.2017-3744.

[88] Yoon, S., Lee, H. C., and Pulliam, T. H. "Computational Analysis of Multi-Rotor Flows." *54th AIAA Aerospace Sciences Meeting*, 2016. https://doi.org/10.2514/6.2016-0812.

[89] Majumdar, S. J., and Peake, N. “Noise Generation by the Interaction between Ingested Turbulence and a Rotating Fan.” *Journal of Fluid Mechanics*, Vol. 359, 1998, pp. 181–216. https://doi.org/10.1017/S0022112097008318.

[90] Robison, R. A. V., and Peake, N. “Noise Generation by Turbulence–Propeller Interaction in Asymmetric Flow.” *Journal of Fluid Mechanics*, Vol. 758, 2014, pp. 121–149. https://doi.org/10.1017/jfm.2014.487.

[91] Lopes, L. v, Boyd, D. D., Nark, D. M., and Wiedemann, K. E. “Identification of Spurious Signals from Permeable Ffowcs Williams and Hawkings Surfaces.”

[92] Sree, D. “A Novel Signal Processing Technique for Separating Tonal and Broadband Noise Components from Counter-Rotating Open-Rotor Acoustic Data.” *International Journal of Aeroacoustics*, Vol. 12, Nos. 1–2, 2013, pp. 169–188. https://doi.org/10.1260/1475-472X.12.1-2.169.

[93] Mani, R. “The Radiation of Sound from a Propeller at Angle of Attack.” *NASA Contractor Report*, Vol. 4264, 1990.

[94] Ghorbaniasl, G., Siozos-Rousoulis, L., and Lacor, C. “A Time-Domain Kirchhoff Formula for the Convective Acoustic Wave Equation.” *Proceedings of the Royal Society A: Mathematical, Physical and Engineering Sciences*, Vol. 472, No. 2187, 2016, p. 20150689. https://doi.org/10.1098/rspa.2015.0689.

[95] Mao, Y., and Hu, Z. “Convective Vector Wave Equation of Aeroacoustics.” *Procedia IUTAM*, Vol. 20, 2017, pp. 81–88. https://doi.org/10.1016/j.piutam.2017.03.011.

[96] Mccluer, M. S. “Helicopter Blade-Vortex Interaction Noise with Comparisons to CFD Calculations.” *NASA Technical Memorandum*, Vol. 110423, 1996.

[97] Brooks, T. F., Stuart, D., and Marcolini, M. A. “NASA Reference Publication 1218 Airfoil Self-Noise and Prediction.” 1989.

[98] Nguyen, L., Golubev, V., Mankbadi, R., Yakhina, G., and Roger, M. “Numerical Investigation of Tonal Trailing-Edge Noise Radiated by Low Reynolds Number Airfoils.” *Applied Sciences*, Vol. 11, No. 5, 2021, p. 2257. https://doi.org/10.3390/app11052257.

[99] Brunton, S. L. (Steven L., and Kutz, J. N. “Data-Driven Science and Engineering: Machine Learning, Dynamical Systems, and Control.” p. 472.

[100] Gavish, M., and Donoho, D. L. “The Optimal Hard Threshold for Singular Values Is 4/ √ 3.” *arXiv*, 2013. https://doi.org/10.48550/arXiv.1305.5870.

[101] VtkToolbox - File Exchange - MATLAB Central. https://www.mathworks.com/matlabcentral/fileexchange/94993-vtktoolbox. Accessed Aug. 3, 2022.

[102] Williams, M. O., Kevrekidis, I. G., and Rowley, C. W. “A Data–Driven Approximation of the Koopman Operator: Extending Dynamic Mode Decomposition.” *Journal of Nonlinear Science*, Vol. 25, No. 6, 2015, pp. 1307–1346. https://doi.org/10.1007/S00332-015-9258-5/FIGURES/14.

[103] Dawson, S. T. M., Hemati, M. S., Williams, M. O., and Rowley, C. W. “Characterizing and Correcting for the Effect of Sensor Noise in the Dynamic Mode Decomposition.” *Experiments in Fluids*, Vol. 57, No. 3, 2015. https://doi.org/10.1007/s00348-016-2127-7.

[104] Proctor, J. L., Brunton, S. L., and Kutz, J. N. “Dynamic Mode Decomposition with Control.” *SIAM Journal on Applied Dynamical Systems*, Vol. 15, No. 1, 2014, pp. 142–161. https://doi.org/10.48550/arxiv.1409.6358.

[105] Liu, X., Wang, H., Yu, X., and Wang, C. “A Krylov-Based Proper Orthogonal Decomposition Method for Elastodynamics Problems with Isogeometric Analysis.” *Engineering Analysis with Boundary Elements*, Vol. 133, 2021, pp. 71–83. https://doi.org/10.1016/J.ENGANABOUND.2021.08.025.

[106] Leslie, A., Wong, K. C., and Auld, D. “Broadband Noise Reduction on a Mini-UAV Propeller.” *14th AIAA/CEAS Aeroacoustics Conference (29th AIAA Aeroacoustics Conference)*, 2008. https://doi.org/10.2514/6.2008-3069.

[107] Gopalan, G., and Schmitz, F. “Far-Field Near-In-Plane Harmonic Main Rotor Helicopter Impulsive Noise Reduction Possibilities.” *American Helicopter Society Annual Forum*, Vol. 64, 2008.

[108] Brès, G. A., Brentner, K. S., Perez, G., and Jones, H. E. “Maneuvering Rotorcraft Noise Prediction.” *Journal of Sound and Vibration*, Vol. 275, Nos. 3–5, 2004, pp. 719–738. https://doi.org/10.1016/J.JSV.2003.07.005.

[109] Brentner, K. S. “Prediction of Helicopter Rotor Discrete Frequency Noise: A Computer Program Incorporating Realistic Blade Motions and Advanced Acoustic Formulation.” *NASA Technical Memorandum 87721*, 1986.

[110] Brentner, K. S., and Jones, H. E. “Noise Prediction for Maneuvering Rotorcraft.” *6th Aeroacoustics Conference and Exhibit*, 2000. https://doi.org/10.2514/6.2000-2031.

[111] Purcell, T. W. “CFD and Transonic Helicopter Sound.” *Proceedings of the Fourteenth European Rotorcraft Forum*, No. 2, 1988.

[112] Brentner, K. S. “Modeling Aerodynamically Generated Sound: Recent Advances in Rotor Noise Prediction.” *38th Aerospace Sciences Meeting and Exhibit*, 2000. https://doi.org/10.2514/6.2000-345.

[113] Lopes, L. v. “Compact Assumption Applied to Monopole Term of Farassat’s Formulations.” *https://doi.org/10.2514/1.C034048*, Vol. 54, No. 5, 2017, pp. 1649–1663. https://doi.org/10.2514/1.C034048.

[114] Kim, H. J., Koo, K., Lee, S. Q., Park, K. H., and Kim, J. “High Performance Piezoelectric Microspeakers and Thin Speaker Array System.” *ETRI Journal*, Vol. 31, No. 6, 2009, pp. 680–687. https://doi.org/10.4218/ETRIJ.09.1209.0010.

[115] Pierce, A. D. “Acoustics.” *Acoustics*, 2019. https://doi.org/10.1007/978-3-030-11214-1.

PUBLICATIONS

Journal Publications

1. Mankbadi, R. R., Afari, S., and Vladimir, V. G., "High-Fidelity Simulations of Noise Generation in A Propeller-Driven UAV," AIAA Journal, December 29, 2020. https://doi.org/10.2514/1.J059117
2. Afari, S., and Mankbadi, R. R., "Active Noise Control of Multi-Rotor Advanced Air Mobility Vehicles," Journal of American Helicopter Society, 2022. https://doi.org/10.4050/JAHS.68.032006
3. Afari, S., and Mankbadi, R. R., "Simulations of Multi-Rotor Interaction Noise at Hovering & Forward Flight Conditions," International Journal of Aeroacoustics, 2023. https://doi.org/10.1177/1475472X231152608
4. Afari, S., Golubev, V., Lyrintzis, A.S., Mankbadi, R., "Review of Control Technologies for Quiet Operations of Advanced Air-Mobility." *Appl. Sci.* **2023**, *13*, 2543. https://doi.org/10.3390/app13042543

Conferences, Proceedings & Other Publications

1. Prediction of noise associated with an isolated UAV propeller, Masters Thesis. https://commons.erau.edu/edt/463/
2. Mankbadi, R. R., Afari, S., and Vladimir, V. G., Towards High-fidelity Analysis of Noise Radiation and Control of Propeller-driven UAV," AIAA Aeroacoustics, May 2019. https://doi.org/10.2514/6.2019-2632
3. Mankbadi, R. R., Afari, S., and Vladimir, V. G., "Simulations of Broadband Noise of a Small UAV Propeller," AIAA SciTech, Jan 2020. https://doi.org/10.2514/6.2020-1493

4. Afari, S., and Mankbadi, R. R., “Simulations of Noise Generated by Rotor-Rotor Interactions at Static Conditions,” AIAA SciTech, Jan 2021. https://doi.org/10.2514/6.2021-1986
5. Afari, S., and Mankbadi, R. R., and Vladimir, V. G., “Review of Multi-Rotor Noise Prediction Techniques,” AIAA Aviation 2022. https://doi.org/10.2514/6.2022-3463
6. Afari, S., and Mankbadi, R. R., “Application of Data Reduction Methodologies to Prediction of Rotor Noise,” AIAA SciTech 2023. https://doi.org/10.2514/6.2023-0029

APPENDIX - A

The FWH formulations utilized in OpenFOAM were developed originally by UniCFDLab [81]. To validate this library, the pulsating sphere case is tested and presented here.

The pulsating sphere is modeled on the source boundary using the formulation documented by Pierce[115]. In this test case, the parameters of the pulsating sphere, and specifications of the acoustic radiation medium are:

- Radius of the sphere, $R = 0.1m$
- Amplitude of velocity, $U_o = 0.01\frac{m}{s}$
- Velocity Oscillations, $\tilde{v} = iU_o \sin(2\pi ft)$
- Speed of sound, $c = 100\frac{m}{s}$
- Density of gas, $\rho = 14.18\frac{kg}{m^3}$

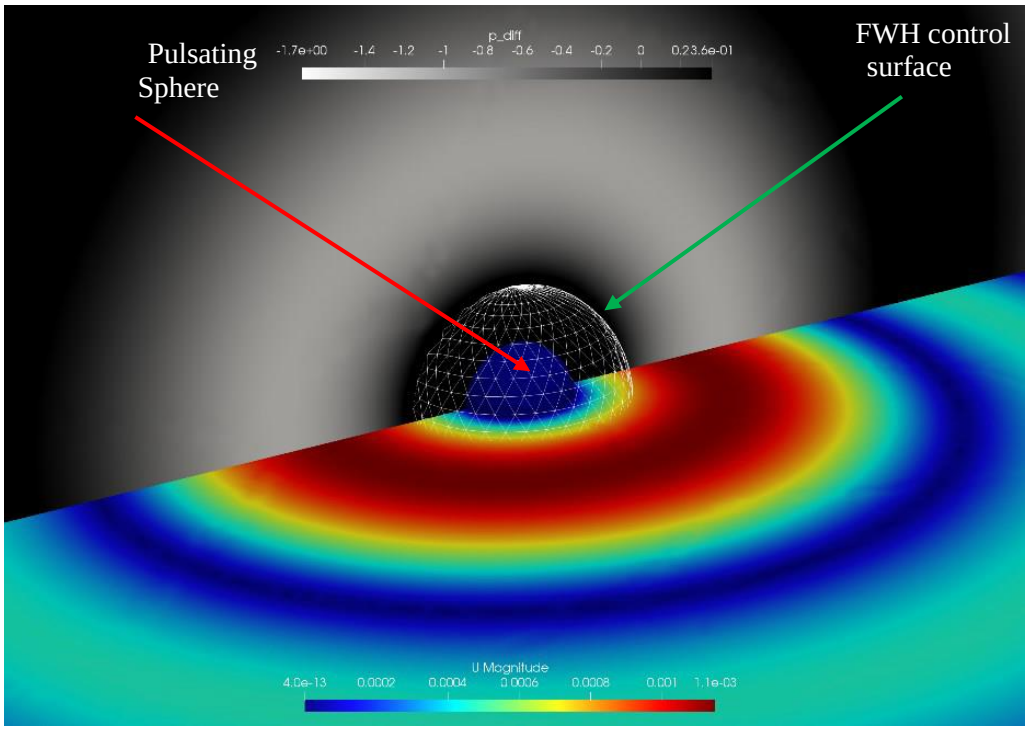

Figure A-5-1 Pulsating sphere and the FWH surface (mesh) in the computational domain

Figure A-5-1 illustrates the pulsating sphere in the computational domain. Two FWH surfaces are used for this study. The first one is right on the surface of the sphere, and the second one is at $2R$ shown as the white mesh in the figure. Data from the two FWH surfaces are collected and compared with the analytical solution at the far field location of r = 10R. The analytical solution for the pulsating sphere given as:

$$\hat{p} = Re\left(\frac{\rho c U_o k R^2}{r(1+ikR)}\right) U_o \sin(2\pi f t)\, e^{-ik(r-R)} \tag{A.1}$$

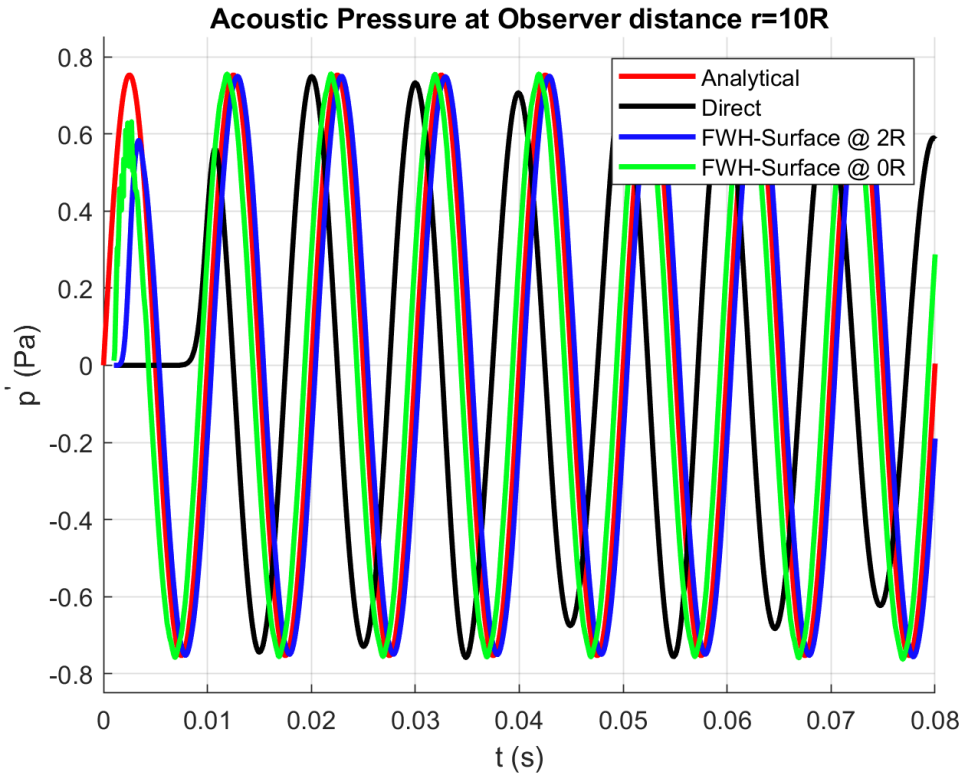

Figure A-5-2 Acoustic pressure time history at the observer location

Figure A-5-2 shows the acoustic pressure time history at the observer location. The far field noise obtained from FWH formulations are compared with the analytical data, as well as directly probed data in a relatively coarse grid region. The calculated acoustic time history from the FWH control surface at 2R shows excellent agreement with the analytical data.